Modelling the Future Impacts of Climate Change on Sediment Yield for a Semi-arid Catchment in South Africa using SHETRAN

by

Georg Frederik Barnardt

Thesis presented in fulfilment of the requirements for the degree of Master of Engineering in Civil Engineering in the Faculty of Engineering at Stellenbosch University

Supervisor: Prof. Gerrit Basson

March 2021

Declaration

By submitting this thesis electronically, I declare that the entirety of the work contained therein is my own, original work, that I am the sole author thereof (save to the extent explicitly otherwise stated), that reproduction and publication thereof by Stellenbosch University will not infringe any third party rights and that I have not previously in its entirety or in part submitted it for obtaining any qualification.

March 2021

Abstract

Sedimentation (caused by soil erosion and high sediment yields) has become a major problem in South Africa, especially in semi-arid regions like the Karoo, where water scarcity and reduction of reservoir storage capacity can cause social and environmental concerns. The uncertainties regarding the impact climate change may have on the hydrological cycle, and the effect on catchment response increase these concerns. This thesis's main objective was to evaluate the possible future impacts of climate change on sediment yield by incorporating predicted future climate data and a physically-based hydrological and sediment yield model, SHETRAN. From a literature study, background information regarding soil and vegetation properties, soil erosion, sediment yield, physically-based models (focussing on the SHETRAN model), climate change, and climate models were obtained.

The Nqweba Dam catchment (3651 km^2), located in the semi-arid region of the Eastern Cape of South Africa, was identified for the analysis. All the information and data required to execute a SHETRAN simulation were obtained, which include: Topography; soil distribution and -characteristics; land cover distribution and vegetation properties; streamflow data; and reservoir survey data. The reservoir survey data was used to determine the historical bed sediment densities and average sediment yield for numerous historical periods in the catchment.

The SHETRAN model was calibrated against observed streamflow and sediment data for current catchment and climate conditions. The calibration parameters were verified, and high sediment yield areas were identified. Future climate data projected by eleven climate models for two possible future emission scenarios were used to determine climate change signals for numerous future periods. The climate change signals were applied to the current climate data to represent possible future climate conditions. It was determined that climate change would cause an increase in average rainfall and evaporation in the study area.

The possibility of vegetation change was evaluated and the calibrated SHETRAN model was implemented for different future scenarios. It was found that climate change will increase sediment yield in relation to the baseline period for the Nqweba Dam catchment. However, the predicted sediment yield is still lower than some historical observations. During the early 1900s, sediment yields higher than 400 t/km^2/a have been recorded, while the future predictions range between 90 and 200 t/km^2/a. The current sediment yield for the Nqweba Dam is 57 t/km^2/a. The historical catchment characteristics were evaluated. It was determined that poor farm management and overgrazing during the early 1900s had a more significant influence on catchment response and the increase in sediment

yield than climate change. Improved farm practices and the construction of numerous farm dams that act as sediment traps significantly impacted the decline in historical sediment yields.

It was suggested that improved farm management must be maintained. In high sediment yield areas, farmers must be educated on the impact of overgrazing and poor farm management on erosion and the downstream effect. Recommendations for the methodology that can be adopted to model climate change and suggestions for future research were given.

Opsomming

Reservoir sedimentasie wat veroorsaak word deur gronderosie en sedimentlewering het 'n groot probleem in Suid-Afrika geword, veral in semi-woestyn streke soos die Karoo, waar waterskaarste en die vermindering van opgaarkapasiteit van damme, sosiale- en omgewingsrisiko's kan veroorsaak. Die onsekerhede rakende die impak wat klimaatsverandering het op die hidrologiese siklus en die invloed op die opvanggebied se reaksie, verhoog hierdie kommer. Die hoofdoel van hierdie tesis was om die moontlike toekomstige gevolge van klimaatsverandering op sedimentlewering te evalueer deur 'n fisies-gebaseerde hidrologiese en sedimentleweringmodel, SHETRAN te implementeer, en voorspelde toekomstige klimaatdata daarop toe te pas. Uit 'n literatuurstudie is agtergrondinligting rakende grond- en plantegroei-eienskappe, gronderosie, sedimentlewering, fisies-gebaseerde modelle (wat op die SHETRAN-model fokus), klimaatsverandering en klimaatmodelle verkry.

Die Nqweba-opvanggebied (3651 km^2) wat in die semi-woestyn streek van die Oos-Kaap van Suid-Afrika geleë is, is vir die ontleding gekies. Al die inligting en data wat benodig word om 'n SHETRAN-simulasie uit te voer, is verkry, insluitend: Topografie; grondverspreiding en -eienskappe; verspreiding van plantegroei en plantegroei-eienskappe; stroomvloei data; en reservoiropname data. Die reservoiropname data is gebruik om die historiese bodemsedimentdigtheid en gemiddelde sedimentlewering vir talle historiese periodes in die opvanggebied te bepaal.

Die SHETRAN-model is gekalibreer teen die waargenome stroomvloei- en sedimentdata vir huidige opvanggebied- en klimaatstoestande en hoë sedimentleweringstreke is geïdentifiseer. Toekomstige klimaatsdata wat deur elf klimaatmodelle geprojekteer word vir twee moontlike toekomstige emissiescenarios, is gebruik om klimaatsveranderingseine vir talle toekomstige tydperke te bepaal. Hierdie seine is op die huidige klimaatdata toegepas om moontlike toekomstige klimaatstoestande voor te stel. Daar is vasgestel dat klimaatsverandering 'n toename in gemiddelde reënval en verdamping sal veroorsaak in die studie area.

Die moontlikheid van plantegroeiverandering is geëvalueer en die gekalibreerde SHETRAN-model is geïmplementeer vir verskillende toekomstige scenario's. Daar is gevind dat klimaatsverandering 'n toename in die sedimentlewering sal veroorsaak in verhouding met die basislynperiode vir die Nqweba-opvanggebied, maar die voorspelde sedimentlewering is steeds laer as sommige historiese waarnemings. Gedurende die vroeë 1900's is sedimentlewerings van meer as 400 t/km^2/a waargeneem, terwyl die toekomstige voorspellings slegs tussen 90 en 200 t/km^2/a is. Die huidige sedimentlewering vir die Nqweba Dam is 57 t/km^2/a. Die historiese opvanggebiedseienskappe is

geëvalueer en daar is vasgestel dat swak boerderybestuur en oorbeweiding 'n groter invloed op die verhooging in sedimentlewering gehad het as klimaatsverandering. Die verbetering van boerderypraktyke en die konstruksie van talle plaas damme, wat sediment opvang, het ‘n beduidede invloed op die vermindering van sedimentlewering vir die Nqweba Dam opvangsgebied gehad.

Daar is voorgestel dat verbeterde boerderypraktyke gehandhaaf moet word en in gebiede met hoë sedimentlewerings moet boere ingelig word oor die impak van oorbeweiding en swak boerderybestuur op erosie en die stroomaf-effek. Aanbevelings vir die metodiek wat gebruik kan word om klimaatsverandering te modelleer, asook voorstelle vir toekomstige navorsing is gegee.

Acknowledgements

The author would like to thank the following individuals and organizations:

- Prof Gerrit Basson for his guidance, knowledge and overseeing the writing of this thesis;
- Dr Kuria Kiringu for assistance with the SHETRAN model application and calibration;
- Louis Swart for assistance with the site survey;
- Weather SA and the Department of Water for providing necessary climate – and reservoir data;
- Haw & Ingles Group for providing funding for my post-graduate studies; and
- Special thanks to my parents and fiancé for providing support throughout.

Table of Contents

List of Figures

List of Tables

1 INTRODUCTION

Reservoirs serve several purposes, including water storage and supply, flood protection, ecological services, and the production of energy in the form of hydropower. When the storage capacity of reservoirs decreases, the purpose of the dam may become jeopardised. The reduction of storage capacity is caused by siltation, which is directly related to erosion and sediment yield. This thesis deals with the future impacts of climate change on sediment yield, and Section 1 gives background, a problem statement, objectives, and research methodology.

1.1 Background

Hydraulic structures and water-related infrastructures like reservoirs, storm-water drains, irrigation projects, and inter-basin transfers are usually designed for a design life of approximately 50 to 100 years. However, according to De Villiers & Basson (2007), sedimentation has reduced the average life-span for reservoirs in South Africa to only 35 years, leading to economic and environmental concerns.

The significance of reservoir sedimentation in South Africa was first realized in 1901 when it was observed that the newly constructed Camperdown Dam was quickly filling with sediment. The observation has lead to a large amount of research and accumulation of fairly reliable long-term sedimentation data for major reservoirs (Rooseboom *et al.*, 1992). However, it is still challenging to relate the sediment yield data obtained from reservoir surveys to catchment erosion. The difficulty is due to high variability in soil type, vegetation cover, slope, and system connectivity within catchments (Boardman *et al.*, 2017).

1.1.1 Soil erosion and land degradation in South Africa

Due to the landscape and soil conditions, large parts of South Africa are prone to soil erosion by water, making it one of the country's leading environmental problems (Le Roux *et al.*, 2008). Soil erosion is a natural process, but human activity may increase the problem. Human activities include poor land management and overgrazing, road construction and urban development, mining activities, deforestation, and human activity that causes climate change. One of the main drivers of soil erosion and land degradation is a decline in vegetation cover, and according to Boardman *et al.* (2017), the decline in vegetation cover is primarily caused by overgrazing.

During the 1950s, the South African government’s focus was on point source discharges, believing this was the leading cause of sediment yield. However, during the 1980s, water resource managers realized that certain land-use practices caused problems on catchment scale. A positive development

during the 1990s was the implementation of a new National Water Act (Act 36 of 1998), which incorporated an Integrated Catchment Management approach and enabled water resources managers to use a legal framework to manage land-use practices. However, implementing policies is still a challenge due to limited human and financial resources (Slaughter, 2011).

To identify the soil erosion on a spatial scale and mitigate the problem, the Department of Agriculture (DOA) and the Water Research Commission (WRC) have initiated numerous regional projects. Rooseboom *et al.* (1992) developed a Sediment Delivery Potential Map (SDM), Pretorius (1995) developed an Erosion Susceptibility Map (ESM) as well as a Predicted Water Erosion Map (PWEM) (Pretorius, 1998). The South African National Biodiversity Institute (SANBI) created a series of maps that illustrate the severity and type of soil degradation for different land-use types (Le Roux *et al.*, 2008). Msadala *et al.* (2010) also reviewed the SDM to improve sediment yield estimates on a regional scale.

1.1.2 Hydrological modelling of erosion and sediment yield

Numerous erosion and sediment yield models are available that can be implemented to estimate erosion rates and sediment yield. Some can only be applied to single slope segments, while others can be used on a catchment scale. For this thesis, the Nqweba Catchment close to Graaff-Reinet in the Eastern Cape of South Africa is used for the case study area. Although a few models are briefly covered in the literature review, all hydrological and sediment yield modelling is done with the SHETRAN model. SHETRAN is a physically-based, spatially distributed erosion and sediment yield model (Ewen *et al.*, 2011). The SHETRAN model was chosen for the analysis because, of the physically-based, basin-scale models, only SHETRAN provides a framework within which components have been developed for raindrop impact, overland flow erosion, landslide erosion, channel bank erosion (although at a simple level), and within which a preliminary design has been developed for a gully erosion component (Bathurst, 2011). The SHETRAN model can also be modified to represent changes within a catchment or climate data and has been used in numerous climate change studies, which will be discussed in the literature review.

The SHETRAN Model can simulate contaminate transport and water quality, but this research focuses on the impact of climate change on sediment yield. Therefore, only the water flow and sediment delivery components are simulated with the SHETRAN model.

1.2 Problem Statement

The Earth's average temperature is rising, causing changes in rainfall patterns and variation in the arrival of seasons and increasing the occurrence of extreme weather events like droughts and floods (IPCC, 2007).

Reservoir sedimentation caused by catchment soil erosion by water and sediment yield is already an economic and ecological concern for water resources managers. Possible future impacts of climate change on sediment yield need to be assessed to provide more clarity for future planning, catchment- and land management, as well as hydraulic design criteria.

1.3 Objectives and research methodology

The main objective of this thesis is to obtain more clarity on the future impacts of climate change on sediment yield for a semi-arid catchment by incorporating climate models with a physically-based hydrological sediment yield model. To achieve this, the following needs to be done:

1. Conduct a literature review to obtain the necessary knowledge and gather information regarding:
    - relevant soil and vegetation parameters;
    - soil erosion and sediment yield;
    - physically-based sediment yield models;
    - SHETRAN model and sediment yield calculations; and
    - climate change and climate models.
2. Define the case study catchment area and obtain required catchment characteristics, which include:
    - Digital Elevation Model (DEM);
    - vegetation, soil, and geological properties; and
    - meteorological data, which includes rainfall, evaporation, and streamflow data.
3. Calibrate the SHETRAN model for current climate and catchment conditions and verify the calibration parameters:
    - Calibrate simulated water flow by using measured gauge plate readings and corresponding inflow data;

- Calibrate the simulated sediment yield by using reservoir survey- and sediment accumulation data; and
- Verify the calibration parameters by applying the SHETRAN model to independent (another period) data.

4. Determine climate change signals:
    - Use average projected data from numerous climate models.
5. Apply climate change signals on current climate data and implement on the calibrated SHETRAN model.
6. Investigate the possible impact of climate change on vegetation and how this influence sediment yield by reapplying the SHETRAN model.
7. Analyse and discuss results.
8. Conclude and make recommendations.

2 LITERATURE REVIEW

Section 2 presents a literature review of the key concepts and terminology used in the research. Included are the basics concerning soil and sediment properties, vegetation cover indices, erosion, and sediment transport. Physically-based models are discussed, with the focus on the SHETRAN model. The water flow-, sediment transport-, and channel erosion calculations will be discussed. An overview of climate change and the factors influencing climate change is given, as well as a description of different climate models.

2.1 Physical properties of soil

The difference between soil and sediment lies in the way they are deposited. Sediments are created by wind and water erosion from a parent rock material or stone. Sediments are characterised by size (nominal- or sieve diameter), density, specific weight, and angularity/smoothness. Soils comprise inorganic (rock and sediments) and organic (decomposed animal or plant material) matter (Yang, 2003).

2.1.1 Porosity

Porosity is a measurement of the fraction of empty spaces (voids) in a soil or rock sample. Porosity is calculated by taking the difference between the density of the particles within a rock or soil sample and a dry sample, divided by the density of the particles. Values of soil porosity can range from 0 in dense rock to 0.5 in fractured limestone, and for soil, 0.3 for sand to 0.6 in clay soils (Freeze & Cherry, 1979).

2.1.2 Soil Moisture Characteristic function

The soil moisture characteristic function is also known as the soil retention curve and relates the soil-water potential (Ψ) with the soil-water content (θ). Factors that influence this relationship includes the textural - and structural soil configuration and the presence of organic material in the soil. If the fraction clay and sand in a sample are known, the soil water potential can be determined for different soil moistures (Saxton *et al.*, 1986). The Ψ- θ relationship is not limited to one curve but can consist of a family of relationships, depending on the wetting and drying history of a specific soil (Salter & Williams, 1965).

2.1.3 Soil Texture size distribution

Soils can be classified by feel, texture, or by measuring the size distribution and are classified according to the percentage of sand, clay, and silt it contains per volume. Sieve analysis is used to determine the size of a sediment particle. According to the British Standards Institution (UNM, 2008), sand particles range between 0.05 mm and 2.0 mm, silt range from 0.002 mm to 0.05 mm, and clay is defined to be less than 0.002 mm. These ranges correspond relatively close to the sediment size ranges defined by Lane (1947). Table A-1 in **Appendix A** illustrates the sediment size ranges defined by Lane (1947).

2.1.4 Saturated Conductivity

For soils, saturated conductivity is defined as the discharge rate per unit area through the soil if it is saturated. In rocks, the saturated conductivity could be lower than 10^{-6}m/day, but it could be up to 10 m/day for karst limestone. For soils, it can range from less than 0.01 m/day for clay to more than 100 m/day when gravel alluvium is considered (Rawls et al., 1982). Table A-2 in **Appendix A** illustrates the saturated conductivity values for different soil types.

2.1.5 Conductivity function (K, θ) relationship

If the soil is saturated, all the pore spaces are filled with water, and the hydraulic conductivity (K) is at a maximum. When the soil becomes drier, the larger pores spaces lose water, and flow through the soil becomes more difficult, causing the hydraulic conductivity to decrease (Rawls et al., 1982).

2.2 Vegetation cover properties

According to Birkinshaw (2016), the following standard vegetation types can be specified for a catchment:

- Arable;
- bare ground;
- grass;
- deciduous forest;
- evergreen forest;
- shrubs; and
- urban.

It is essential to know how and to what extent the vegetation covers the surface of a catchment. The plant area index (PLAI) is defined as the proportion of the ground that is always bare, divided by the ground covered with vegetation for the time when the vegetation is in leaf. The canopy leaf area index (CLAI) is defined as the ratio of the total area covered with leaves to the ground area covered with vegetation. For some vegetation types, the CLAI can vary during the year for different seasons (Birkinshaw, 2013).

The PLAI can range from 0 for bare ground to 1 for the scenario where the vegetation covers the entire surface area. For forests, the CLAI can vary between 0.1 and 6, depending on the season. The PLAI and CLAI values for the standard vegetation types can be seen in Table B-1 in **Appendix B**.

2.2.1 Canopy Storage

Vegetation can prevent water from reaching the ground surface. The maximum quantity of water (mm) that can be held back is known as the canopy storage capacity (CSTCAP). The value of CSTCAP is dependent on the size of the leaves, their arrangement, orientation, and roughness, as well as gravity and the forces created by wind (Birkinshaw, 2013). Values for the CSTCAP for the standard vegetation types can be seen in Table B-1 in **Appendix B**.

2.2.2 Drainage parameters

Two parameters, developed by Rutter *et al.* (1972), are used to define how water, held by the vegetation canopy, drain to the ground surface. The Rutter Ck parameter represents the drainage rate when the CSTCAP is reached. When the canopy becomes drier, the drainage rate decreases. The decreased drainage rate is determined with the Rutter Cb parameter, incorporated in an exponential function (Birkinshaw, 2013). The drainage parameters for the standard vegetation types are illustrated in Table B-1 in **Appendix B**.

2.2.3 Root Density functions

The root density function (RDF) is dependent on the depth of the roots below the ground surface and the proportion of the roots for different depths. The RDF is required to determine the water loss due to transpiration from the different depths. With a higher RDF, the transpiration rate increases. The most accurate method to determine the RDF for the vegetation in a catchment is by digging soil pits. Literature values can also be used to estimate the RDF, but variations are likely due to different soil conditions (Birkinshaw, 2013). Table B-2 in **Appendix B** gives the values for the RDF for the standard vegetation types.

2.2.4 Evapotranspiration Parameters

Intercepted water can evaporate from the canopy or the bare soil, and most of the water absorbed by the vegetation's roots is lost through transpiration. Potential evaporation E_p is defined as the evaporation of water under ideal conditions from open water.

Important parameters to consider when evapotranspiration is calculated are the aerodynamic and canopy resistance, r_a and r_c. The r_a is defined as the force exerted by the air, restraining evapotranspiration, and is dependent on the friction created by the air moving over the vegetation. The r_c is defined as the resistance exerted by the plant's stomata and considers the moisture of the soil.

2.2.5 Relationship between vegetation and rainfall

According to Levy (2019), vegetation is expressed as an index of greenness, which is a factor of:

- the density and type of plant;
- how leafy they are; and
- the plant health.

The most common index that is used to express vegetation greenness is the Normalised Difference Vegetation Index (NDVI). The NDVI is based on data obtained from satellite sensors that measure the spectral reflections in the red and near-infrared wavelength areas, that is sensitive to the presence, health, and density of vegetation. (Herrmann, Anyamba & Tucker, 2005).

According to a study conducted by Herrmann *et al.* (2005), a linear regression between rainfall and the NDVI exist for their study area (West African Sahel), as illustrated in Figure 2.1.

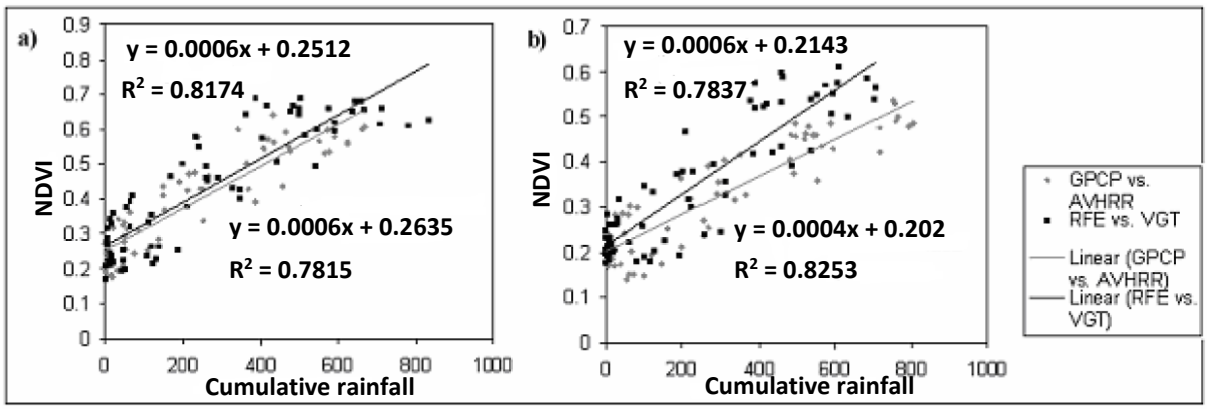

Figure 2.1: Linear regression between rainfall and NDVI (West African Sahel) (Herrmann *et al.*, 2005)

2.3 Soil Erosion

Land resource is one of the most important geological resources in the world and is used for agriculture, reforestation, urban development, water resource management, and tourism. Human land-use and resource utilisation is an indication of the extent to which human civilization has developed, but it also causes negative impacts on the environment. One of the negative impacts is soil erosion.

Soil erosion is the removal and transport of soil or sediment particles by water or wind abrasion. Although soil erosion is a natural geomorphic process, human activity has accelerated the erosion rate drastically. According to the Food and Agriculture Organization (FAO), (a branch of the United Nations), the global loss of usable land due to erosion is estimated to be between 5 and 7 million hectares per year. Annually, approximately 23 billion tons of topsoil of the world farmland is lost due to erosion (FAO, 2019).

For South Africa, the average predicted soil loss rate due to erosion is approximately 12.6 tons/ha/year. However, it is not only the loss of fertile topsoil that is a problem. Transported sediment causes severe off-site problems when delivered to rivers or dams, causing siltation (Le Roux 2014).

2.3.1 Soil erosion prediction in South Africa

South Africa was included in studies conducted by the Global Assessment of Human-induced Soil Degradation (GLASOD). A soil erosion risk map was created by dividing soil erosion areas into units, depicting the vital erosion processes (Laker, 2004).

In 1991, Rooseboom *et al.* (1992) were instructed by the Water Research Commission (WRC) to develop a sediment yield map for southern Africa. The sediment yield map was developed by taking soil erodibility, rainfall, land use, and slope into consideration. The soil erodibility, rainfall, land use, and slope factors were obtained from land type data produced by the Agricultural Research Council – Institute for Soil, Climate, and Water (ARC-ISCW).

In 1993 an Erosion Susceptibility Map was developed by the ARC-ISCW, with remote sensing and GIS. A green vegetation cover map obtained from satellite data was integrated with the sediment yield map. With continued research in 1998, the Predicted Water Erosion Map (PWEM) was developed with the help of the Universal Soil Loss Equation (USLE) within a GIS framework.

Further studies during the 2000s resulted in the mapping and monitoring of natural resources for different provinces in South Africa. Soil erosion was assessed by applying the Revised USLE (RUSLE)

and incorporating an erosion susceptibility map, the soil erodibility index, and the erosion hazard classes. Important factors that were considered include topography, soil, and climate. Topography factors were obtained with the help of Digital Elevation Models (DEM), and soil maps were used to determine the soil erodibility ratings (Wessels *et al.*, 2001).

In 2010 Msadala *et al.* did a study to determine the predicted sediment yield for South Africa by evaluating three approaches. First, they considered a probabilistic method and used available regional data for observed sediment yields in a statistical analysis. Second, they developed an empirical method from regression analysis by evaluating parameters that influence sediment yield. These parameters include floods, river slope and density, catchment area, and soil erosion hazard classes. Third, they evaluated the use of two physically-based models (SHETRAN and ACRU) to estimate the sediment yield for different regions.

2.3.2 Types of soil erosion

The three main erosion types are water -, wind _ and tillage erosion. Wind erosion occurs when the forces created by wind causes soil particles to detach from the ground surface and transported within the wind stream. The distance the particles are transported is dependent on the size of the detached grains. Tillage erosion is not well known, and its importance was only recognised in the 1990s. While it is occurring, tillage erosion is not easy to observe but is caused by tillage implements during land preparation for crops. Soil is moved downslope and causes the upper slope areas to lose soil while over-thickening lower slope areas (FAO, 2019). For this study, sediment yield is important, and therefore the focus will be on water erosion. Water erosion is also the most widely researched of all the erosion types.

2.3.3 Water erosion

For water erosion, soil particles' detachment from the ground surface is caused by rainfall and inadequate drainage. The impact of raindrops on the ground surface splashes the particles into the air and can remove seeds from the ground. The detachment of soil is measured in kg/m^2 and is a product of the following:

- the kinetic energy of raindrop impact (kJ/m^2);
- the energy required to initiate detachment of particles; and
- soil detachability (kg/kJ) – decrease if particle size increase.

Detached particles can block the soil's surface pores, causing the runoff to increase. The ground surface also becomes smoother, causing runoff velocity to increase (FAO, 2019).

When runoff is generated by rainfall and the forces created by water flowing over the ground surface exceed the soil's hydraulic resistance, it causes particles to be detached and transported downslope, which is known as sheet erosion. The soil's hydraulic resistance depends on the ground surface factors, which include surface roughness, rock fragment content, particle size, and vegetation (FAO, 2019).

When the flow converges into small channels, it causes rill erosion. Rill erosion is the most common form of water erosion. If deeper incisions are created, it leads to gully erosion. Sheet - and rill erosion can be filled by tillage, while gullies are defined as deep cuts in the soil that cannot be fixed with normal tillage operations. Castillo and Gómez (2016) defined a threshold depth of 0.3 m between rills and gullies. The difference between sheet-, rill-, and gully erosion are illustrated in Figure 2.2.

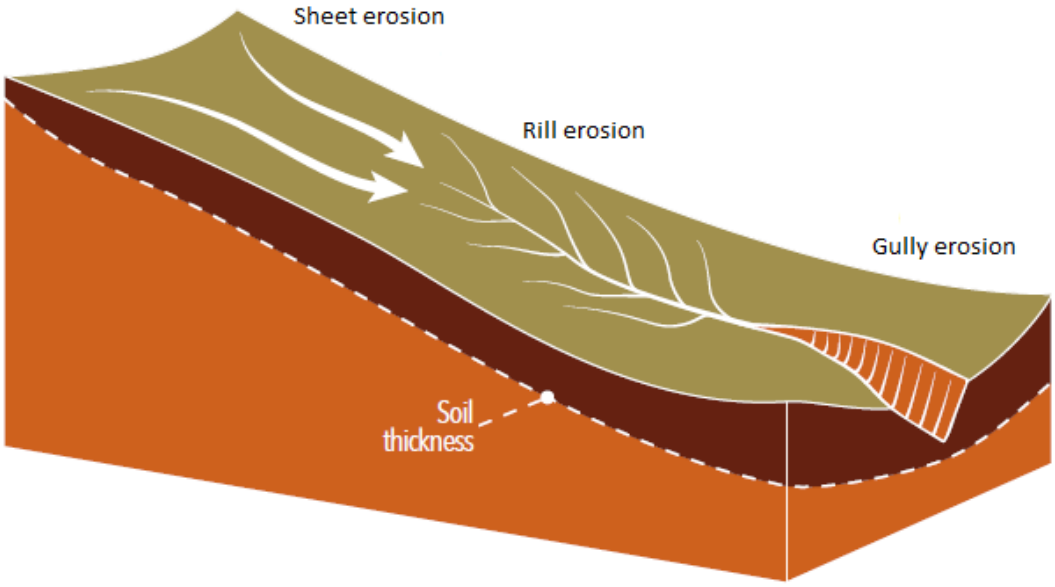

Figure 2.2: Schematic representation of sheet-, rill-, and gully erosion (FAO, 2019)

For sheet -, rill -, or gully erosion, if the flowing water's velocity or depth decreases sufficiently, sediment particles can settle out, and the eroded soil is deposited. However, if deposition does not occur, the sediment is transported with a stream system to reservoirs or the sea (FAO, 2019).

2.3.4 Factors influencing and causing soil erosion

Soil erosion is a physical process, and the erosion rate is dependent on site-specific conditions. The leading causes can be divided between natural- or human-induced factors, although sometimes human-activity (causing climate change) can also influence natural factors.

According to Anthoni (2000), natural factors that influence soil erosion include the following:

- Heavy downpour on weak soil cause soil particles to detach from the ground surface and be transported downslope;

- Reduced vegetation growth due to drought causes more raindrops to fall on the bare ground than vegetation cover. Droughts can also cause water to dry up, making soil vulnerable to wind erosion;
- Steep slopes increase the soil erosion rate because the water flows faster, causing the soil to move downhill; and
- Sudden climate change like unexpected rainstorms, -droughts, or changing winds, increase soil erosion.

According to Anthoni (2000) and FAO (2019), human-induced factors that influence soil erosion includes the following:

- Changes to the land, which include deforestation, urban development, land levelling, and soil excavation cause the loss of soil biota;
- Intensive farming (overgrazing, tillage, crop harvesting, and excessive irrigation) may permanently damage the land; and
- Road construction causes drainage problems, and if roadsides are not adequately maintained, soil erosion is imminent.

2.3.4.1 Climate

From all the factors influencing soil erosion, rainfall is the most significant. Two attributes are important to consider. The first is rainfall amount, and the second is rainfall intensity. According to Anthoni (2000), water is approximately 800 times heavier than air, and the characteristics of raindrops are expressed as kinetic energy. Therefore, if the size of the raindrops increases, the destructive power increases drastically. The susceptibility of erosion due to rainfall is known as Erosivity (R) and is measured by multiplying the total kinetic energy of a rainstorm by the maximum 30-minute rainfall intensity (Wischmeier, 1959).

2.3.4.2 Soil

Soil properties have a significant effect on soil erosion. Water falling on the ground surface can either infiltrate the soil or, if a slope is present, continue along the ground surface as runoff. Factors influencing infiltration include rainfall intensity and drop size, the slope of the ground surface, and the infiltration rate of the soil. The infiltration rate is influenced by the pores' size and continuity, the pre-existing soil moisture condition, organic matter content of the soil, cultivation history, and vegetation. The most important soil characteristic influencing soil erodibility is particle size. In clay-dominated soils, high cohesion between particles will resist the detachment of particles. Medium to coarse sand

consists of larger particles, making it more difficult to be transported. Silt – and loamy soils are more vulnerable, and particles are easier detached and transported (FAO, 2019).

Another essential soil parameter influencing soil erosion is surface roughness. If the surface roughness increases, the resistance (friction) against flowing water increases, causing the erosive potential to decrease. Factors that increase surface roughness include large aggregates, clods from tillage, vegetation, and rock fragments on the ground surface (Torri & Borselli, 2012).

Soil erosivity is predicted with the soil-erodibility factor, K of the Revised Universal Soil Loss Equation (RUSLE). The soil-erodiblity factor takes the soil texture - and structure class, organic matter content, and soil permeability class into consideration (FAO, 2019).

2.3.4.3 Topography

Although gravity is responsible for keeping soil in its position, it also “pulls” soil and water down-slope. Flat surfaces are very stable, but when the slope increases, the water flows faster, and the erosion rate increases linearly. Slopes between 2 and 5% are vulnerable to soil losses, and a slope of 10 to 15% have an erosion potential of 8 to 16 times higher than flat land. Slopes greater than 20% are less affected because they are usually higher uphill, receive less runoff, and the duration that water flows over the ground surface is less (Anthoni, 2000).

When across-slope curvatures are present on a hillslope, water will flow from convex areas to concave areas. The flow will concentrate in the concave areas, creating streamlets and increase erosion.

2.3.4.4 Vegetation

Vegetation is the best defence against soil erosion by water, and the influence it has on the erosion processes is summarized by FAO (2019) as follows:

- Vegetation intercepts and prevents a portion of rainfall to reach the ground surface, delaying the time it takes to wet the soil;
- The soil is protected by vegetation against raindrop impact, decreasing the detachment of soil particles;
- Plant roots increase the infiltration rate by increasing macro-porosity, reducing runoff, and consequently decreasing soil erosion;
- Plant roots decrease erosion by resisting flow detachment of soil particles;
- Vegetation plays a vital role in decreasing the erosion energy by providing resistance against the overland flow. The overland flow resistance increases from cropland to grassland to forest; and

- Vegetation and organic matter produced by plants create water-stable aggregates, increasing infiltration and resistance against erosion.

Gyssels *et al.* (2005) researched the relationship between the relative erosion loss for a given vegetation cover and the soil loss from bare soil. Table 2.1 summarizes the reduction of sheet and rill erosion for an increase in vegetation cover, compared to bare ground.

Table 2.1: Relationship between relative soil loss and vegetation cover(Gyssels *et al.*, 2005)

Vegetation Cover (%)	Reduction of sheet and rill erosion (compared to bare ground) (%)
20	50
30-35	75
60	90

2.3.5 Assessment of soil erosion

Soil erosion can be physically determined by measuring the evidence of its presence in a catchment. The physical method includes measuring the depth and extent of rills and gullies, exposure of vegetation roots, parts of structures, or fence posts, which were supposed to be below ground, as well as the amount of sediment intercepted by drains. According to Evans (2013), these physical methods give a good representation of the actual erosion rate in a catchment, but consist of only a small part of the estimates provided by models.

Soil erosion is also evaluated by remote sensing, using close-range photogrammetry with drones and ground-based light detection and range (LIDAR). According to Bennett and Wells (2019), remote sensing and close-range photogrammetry might replace model-based approximations because they use actual measurements, and technology is continuously developing.

2.3.5.1 Sediment yield from river basins and catchments

Sediment yield is defined as the mass of sediment measured at a point of interest over a specific period (ton/year). If the area of the catchment is also considered, sediment yield is expressed in units of ton/km^2/year.

Measuring suspended sediment concentration, and water flow from river basins and catchments, have been commonly used to evaluate water erosion. The measurements are done at gauging stations along a river channel or stream. The water discharge is monitored, and devices are used to obtain samples of the sediment load at prescribed time intervals. According to Poesen (2018), the literature on more than 1200 catchments in Europe is available, and more than 500 studies have been done on

sediment accumulation in reservoirs. In South Africa, extensive sediment sampling in rivers was conducted between 1920 and 1970. After the 1970s, river samples are still being taken, but not very often. Because most of the dams in South Africa were constructed during the 1960s and 1970s, the DWA decided to focus on reservoir surveys instead of river suspended sediment sampling to determine sediment yields and river sedimentation (Msadala *et al.*, 2010).

Reservoir surveys are usually conducted every 10 to 15 years at most DWA dams in South Africa but are also necessary after a 1:20 year flood or larger. The datum for surveys should always be the Non-Overspill Crest (NOC) and never the water level. It is also crucial that fixed cross-sections are used and that the control beacons are monitored during each survey. In South Africa, the required vertical accuracy for measurements is 20 mm (Msadala *et al.*, 2010).

According to the FAO (2019), estimating soil erosion from sediment yield on a catchment-scale have limitations. Included are the following:

- A considerable amount of eroded sediment is deposited and stored within the catchment. Therefore the sediment at the measuring point only consists of a fraction of the actual eroded soil;
- Temporal deposition of sediment on hillslopes and in streams and rivers results in a time lag between actual erosion and the sediment yield measurements;
- Some of the sediment transported in rivers are not there due to the soil erosion but could be mobilized sediment from floodplains. The mobilization of deposited sediments usually occurs during a flood event; and
- It is challenging to duplicate a catchment, and therefore any statistical analysis or model-based approach, which incorporates physical parameters, may lead to inaccuracies in predicting sediment yield.

2.3.5.2 Models

Models are widely used to predict soil erosion and sediment yield under different climate and land use conditions. When scenario planning is considered, the most commonly used model for the evaluation of water erosion is the RUSLE, which is a revision of the original USLE.

Soil loss can be estimated using experimental designs like rainfall simulators and erosion-runoff plots. Raindrop size and rainfall intensity can be manipulated, and simulations executed on different ground surface conditions. The USLE was developed with the help of these rainfall simulators. The USLE (Eq. 2.1) calculates the predicted amount of soil loss by erosion and takes the climate, soil type,

topography, and land use into account (FAO, 2019). The RUSLE is based on the same structure as the USLE but incorporates new research on these factors.

$$A = RKLSCP \quad (2.1)$$

Where:

- A = Average soil loss per year (ton/ha/a)
- R = Rainfall erosivity factor (MJ mm/ha/h/a)
- K = Soil erodibility factor (Mg ha h /ha/MJ/mm)
- L = Slope length factor
- S = Slope steepness factor
- C = Cover management factor
- P = Supporting practice factor.

The slope length factor represents the length of the slope segment under consideration in the down-slope direction. The cover management factor is dependent on the comparison between the crop growth rate and the variation in erosion for different climate conditions. The supporting practice factor takes terracing, strip cropping, and the use of contours into account (Wischmeier, 1959).

The problem is that the USLE was developed to evaluate a single slope segment with a constant slope, making it difficult to use on a catchment scale. The USLE also calculates soil loss and not sediment yield. Regarding the Rainfall erosivity, there is a lack of clear considerations in runoff when the R factor is considered, causing uncertainty when soil loss is calculated (Kinnell, 2016). The USLE was refined, and the Modified USLE (MUSLE) was developed. The MUSLE uses peak flow data and runoff to determine soil loss for a specific event (Sadeghi *et al.*, 2014). Many of these approaches have been used in physically-based models to determine sediment yield. Due to the extent to which physically-based models, and SHETRAN in particular, are going to be used in this research, physically-based models are dealt with in more detail in the following sections.

2.4 Physically-based models

Physically-based models can simulate erosion and sediment yield and are based on the interrelationships between these controlling processes while taking time and space into consideration. Detailed results of the sediment transport, erosion, and sediment yield can be generated with physically-based models. Many physically-based models are available to study soil

erosion and sediment yield. Pandey *et al.* (2016) reviewed 50 physically-based models regarding input requirements, practical applicability and capability, complexity, representation of processes, and types of output they provide. A few examples of physically-based models include:

- SHETRAN (Ewen *et al.*, 2011);
- SWAT (Soil Water Assessment Tool) (Arnold *et al.*, 1998);
- WEPP (Water Erosion Prediction Project) (Savabi *et al.*, 2007);
- ANSWERS (Areal Non-point Source Watershed Environmental Response Simulation) (Beasley *et al.*, 2013);
- HSPF (Hydrological Simulation Programme – FORTRAN) (Bicknell *et al.*, 1996);
- CREAMS (Chemicals, Runoff, and Erosion from Agricultural Management Systems) (Kinsel, 1980);
- KINEROS (Kinematic runoff and Erosion Model) (Borah & Bera, 2003); and
- EUROSEM (European Soil Erosion Model) (Morgan *et al.*, 1998).

2.5 The SHETRAN Model

SHETRAN, which is physically-based and spatially distributed, is a hydrological and sediment yield modelling system (Ewen et al., 2011). In order to execute the erosion and sediment yield simulations, SHETRAN uses equations and functions coded into the model. SHETRAN is also known to model subsurface flow and transport. The modelling of subsurface flow and transport are possible because SHETRAN uses a grid network of three-dimensional columns that take the different soil layers into account. The soil thickness is represented by these layers, and the surface of the top layer represents the overland surface. For SHETRAN to execute a basic simulation, four compulsory modules are required. The basic modules consist of the Frame-, Evapotranspiration-, Overland and channel-, and the Variably saturated surface module (Ewen et al., 2011).

The Frame module represents the body of the model where the simulation control parameters are entered, as well as the catchment geometry. Included in the Frame module are information about the simulation time step, general data concerning element numbers and sizes, and details regarding the results output (Ewen et al., 2011).

SHETRAN calculates the potential evaporation and transpiration in the Evapotranspiration module, taking the vegetation, soil characteristics, and water surfaces into account. The model also calculates

the amount of water absorbed by plants in the root zone, canopy storage, total precipitation under the canopy, as well as the drainage from the canopy (Ewen et al., 2011).

The Overland - and Channel module compute the flow over the surface of the catchment, as well as in the channels, by determining the water depth. The Variably saturated subsurface module calculates water movement in the subsurface, taking seepage into account (Ewen et al., 2011).

Four optional modules are also available to amplify the SHETRAN simulations. Included are a Bank-, Snowmelt-, Sediment erosion and transport-, and Contaminant transport module (Ewen et al., 2011). In order to calculate the sediment yield and erosion processes for a catchment, the sediment erosion and transport module need to be included in the simulation.

2.5.1 SHETRAN flow calculations

In order to execute a SHETRAN simulation, different meteorological inputs are required. Meteorological data include precipitation (rain or snow) and potential evaporation (measured or calculated). The total water that reaches the ground surface is calculated by considering the interception, evaporation, and drainage characteristics of the vegetation canopy (Parkin, 1995). The Rutter model is used to calculate interception. The actual evapotranspiration rates are calculated with the Penman-Monteith equation and by taking the dynamic soil moisture conditions into account. The soil moisture content and recharge to the saturated zone are determined by taking infiltration into account. Surface water in the form of sheet overland flow is generated, due to infiltration – and saturation excess, and routed into the channels. For each catchment, the channels are represented in a network of channels with different cross-sections feeding to a single outflow (Parkin, 1995).

2.5.1.1 Evapo-transpiration (ET) calculations

According to Parkin (1995), the calculation procedure in SHETRAN for evapotranspiration are as follows:

1. The model calls the snowmelt module if it is present. If the temperature is more than zero degrees, the canopy calculations are executed. No ET calculations are performed if the temperature is below zero degrees.
2. Potential evaporation is calculated with Eq. (2.2) (Penman, 1948).

$$E_p = \frac{R_n\Delta + \left(\frac{\rho_A C_p \delta_e}{r_a}\right)}{\lambda(\Delta + \gamma)} \qquad (2.2)$$

Where:

- E_p = potential evaporation
- R_n = net radiation
- Δ = increase rate of the saturation vapour pressure of water at air temperature
- ρ_A = air density
- C_p = specific heat of the air
- δ_e = vapour pressure shortage of air
- r_a = aerodynamic resistance to movement of water vapour from the canopy to a plane two meters above it
- λ = latent heat of vaporization of water
- γ = psychrometric constant.

3. The evaporation is calculated by taking interception, canopy storage, and drainage from the canopy into consideration.
4. The net precipitation is calculated as the sum of the water that falls on bare soil and the drainage from the canopy, taking the area covered by vegetation into account.
5. The soil moisture loss, due to transpiration from the cells in the root zone, is calculated.
6. Evaporation from the ground surface is calculated.

2.5.1.2 Overland and Channel (OC) flow calculations

The OC module uses the basic continuity equation to calculate the water depth of the water on the surface of the soil and in the channels. The OC module also calculates the flow over the ground surface, in the channel networks, and overbank flooding. Eq. (2.3) represents the continuity equation for a grid square -, bank element or channel link (Parkin, 1995).

$$\frac{\partial h}{\partial t} = \frac{1}{A}\left[\sum_{i=1}^{4} Q_i + Q_R\right] \tag{2.3}$$

Where:

- h = depth of water above the ground in the element
- t = time
- A = surface area of the element

- Q_i = lateral inflow into the element (assumed positive)
- Q_R = sum of net precipitation and excess flow to the surface due to saturation.

When overbank flooding is considered, it is assumed that the bank is 'drowned' or flooded if:

$$z_d > \frac{2z_u + z_b}{3} \tag{2.4}$$

Where:

- z_b = the elevation of the bank
- z_u = upstream water elevation
- z_d = downstream water elevation.

If the bank is flooded, the flow between the bank element and the channel link is calculated with Eq.(2.5), the broad-crested weir equation (Henderson, 1966), eg.

$$Q = \sqrt{2g} \cdot w(z_u - z_d)^{0.5}(z_d - z_b) \tag{2.5}$$

Where:

- w = the length of the channel link ('weir' width)
- g = gravitational acceleration.

If the channel is not flooded, the flow is calculated with Eq. (2.6) (Henderson, 1966).

$$Q = 0.386\sqrt{2g} \cdot w(z_u - z_b)^{3/2} \tag{2.6}$$

2.5.1.3 Variably Saturated Subsurface Calculations

Three-dimensional flow is simulated for saturated or unsaturated conditions, taking porosity and permeability into account. Even if multiple permeable layers (with different characteristics) are present, the simulation can be executed. The simulation can also deal with different aquifers and perched groundwater. Seepage faces are defined at the ground surface and where layers overlap with a stream channel. When a spring is present, it is represented by a point discharge, at the point where the groundwater flows directly into a stream channel (Parkin, 1995).

2.5.2 Sediment Transport (ST) component

The ST module uses a lot of the parameters defined in the flow components and simulates erosion, transport, and deposition of sediment on the hillslope and along the channel network. The hillslope includes the ground surface of the catchment as well as the surface of the bank elements. The hillslope

subcomponent allows the soil to be redistributed across the catchment and serves as an input of sediment to the channel network. In the channel, the sediment transport is simulated, taking in-channel erosion and deposition into account (Lukey *et al.*, 1995).

2.5.2.1 Hillslope erosion and sediment transport

This subcomponent deals with soil erosion due to raindrop- and leaf drip impact, as well as soil erosion due to overland flow. First, the amount of soil erosion is determined by considering the rainfall data. In the hillslope erosion process, erosion only refers to the detachment of the sediment particles from the main soil body and not sediment transport. The eroded sediment is further simulated across the model grid network with the overland flow calculations. The erosion rate due to raindrop- and leaf impact is calculated with Eq. (2.7) (Wicks & Bathurst, 1996)

$$D_r = k_r F_w (1-C_g-C_r)\left(\sqrt{M_r + M_d}\right) \tag{2.7}$$

Where:

- D_r = rate of the detachment of sediment in (kg $m^{-2}s^{-1}$)
- k_r = soil erodibility coefficient due to raindrop impact (J^{-1})
- C_g = proportion of surface protected by near ground cover
- C_r = proportion of surface protected by the ground-level cover
- M_r = momentum of raindrops reaching the ground per unit area $(kg^2\ s^{-3})$
- M_d = momentum of leaf drip reaching the ground per unit area $(kg^2\ s^{-3})$

- F_w represents the protective effect that a layer of water on the ground surface would have on the erosion rate, where:

$$F_w = \begin{cases} 1 & \text{if } h \le d_m \\ \exp\left(1-\frac{h}{d_m}\right) & \text{if } h > d_m \end{cases} \tag{2.8}$$

Where:

- h = the water depth on the surface (m)
- d_m = the effective drop and drip diameter (m).

According to Laws and Parsons (1943), the effective drip/drop diameter is determined by Eq. (2.9).

$$d_m = \max\left[d_{min}, d_1\left(\frac{R_D}{P_N}\right), 0.01935 \cdot P_N^{0.182}\right] \tag{2.9}$$

Where:

- $d_{min} = 10^{-4}$ (minimum allowed for d_m)
- $d_1 =$ leaf drip diameter (m)
- $R_D =$ drainage rate of water from the canopy (m s^{-1})
- $P_N =$ net precipitation rate (including canopy drainage) (m s^{-1}).

The raindrop momentum is calculated with Eq. (2.10).

$$M_r = A_1(1\text{-}C_c)a_1 I^{b_1} \tag{2.10}$$

Where:

- $A_1 =$ area over which M_r is determined (m^2)
- $C_c =$ proportion of surface shielded by dominant vegetation cover
- $I =$ the average rainfall intensity over A_1 (mm h^{-1})
- a_1 and b_1 are read from Table 2.2 for different ranges of rainfall intensity.

Table 2.2: Constants a_1 and a_2 for different rainfall intensities (Marshall & Palmer, 1950)

Rainfall intensity (mm/h)	a_1	b_1
0 - 10	2.6893 (10^{-8})	1.689
10 - 50	3.7514 (10^{-8})	1.5545
50 - 100	6.1192 (10^{-8})	1.4242
≥ 100	11.737(10^{-8})	1.2821

To determine the leaf drip momentum, Eq. (2.11) is used (Wicks, 1996).

$$M_d = \frac{\pi}{6} V_d^2 \rho^2 d_1^3 L_d R_D \tag{2.11}$$

Where:

- d_1 and R_D is as defined earlier
- $L_d =$ proportion of drainage defined as leaf drip
- $V_d =$ leaf drip falling velocity, defined by Eq. (2.12).

$$V_d = \sqrt{\frac{M}{\beta} g \left(1\text{-}e^{\frac{2X\beta}{M}}\right)} \tag{2.12}$$

Where:

- $X =$ average distance drops fall from leaves to the ground
- M= average mass of falling drops

- β= friction constant

and,

$$\frac{M}{\beta} = a_2 + b_2 d_1 \tag{2.13}$$

Where:

- a_2 and b_2 are constants and found in Table 2.3.

Table 2.3: Constants a_2 and b_2 for different drop diameters and average fall distance to the ground (Lukey et al., 1995)

d_1 (m)	X (m)	a_2	b_2
< 0.0033	all X	0	2200
≥ 0.0033	< 7.5	1.93	1640
≥ 0.0033	≥ 7.5	5.14	660

2.5.2.2 Overland Erosion Calculations

The erosion rate due to overland flow is calculated with Eq. (2.14). This equation is applicable when the shear stress caused by overland flow is greater than the critical shear stress for incipient motion (Kamphuis & Hall, 2008).

$$D_q = k_f(1-C_r)\left[\frac{\tau}{\tau_c} - 1\right] \tag{2.14}$$

Where:

- D_q = erosion rate due to overland flow per unit area
- k_f = soil erodibility coefficient for overland flow
- τ = shear stress caused by overland flow
- τ_c = critical shear stress for incipient motion.

The shear stress is calculated with Eq. (2.15)

$$\tau = \rho g h S \tag{2.15}$$

Where:

- ρ= water density
- h= water depth
- S= slope of the water surface in the flow direction.

There are two methods provided by SHETRAN to calculate the critical shear stress. The first option is to use the Shields (1936) curve and the second is with Eq. (2.16). This expression was obtained by Smerdon and Beasley's experiments in 1961 (Clark & Wynn, 2013).

$$\tau_c = 0.493 \times 10^{1.83F_c} \quad (2.16)$$

Where:

- F_c = fraction of clay present in sediment by weight.

2.5.2.3 Protection against overland soil erosion

There are three types of protection or cover defined in the sediment module. Firstly, there are ground cover (C_g), which is defined as low-lying vegetation or vegetation litter. The near-ground cover only protects the soil against erosion due to raindrop and leaf drip impact. Secondly, there are rock cover (C_r), which may include mulch, stones (or rocks), and concrete surfaces. Rock cover protects soil against drip and drop – and overland flow erosion. Lastly, canopy cover is defined. Canopy cover is the part of the surface covered by the dominant vegetation type. Protection against the direct impact of raindrops is provided, but erosion due to leaf drip is still considered. Canopy cover is calculated with Eq. (2.17) (Parkin, 1995).

$$C_c = PLAI * \min[CLAI, 1] \quad (2.17)$$

Where:

- PLAI = plant leaf area index
- CLAI = canopy leaf area index.

2.5.2.4 Overland Transport calculations

SHETRAN provides two options to calculate the overland sediment transport. The first is the Yalin equation (Eq. (2.18)) (Yalin, 1963). The second option is the Engelund-Hansen equation (Eq. (2.19)) (Engelund & Hansen, 1967).

$$G_{tot} = 0.635 \sqrt{\frac{\tau}{\rho}} \cdot LD_{50}\delta \left[1 - \frac{1}{a\delta} \ln(1+a\delta)\right] \quad (2.18)$$

$$G_{tot} = \begin{cases} \dfrac{0.05Q^2S^{\frac{3}{2}}}{\sqrt{gh}\left(\frac{\rho_s}{\rho}-1\right)^2 D_{50}L}, & if\ h > 0 \\ 0, & otherwise \end{cases} \tag{2.19}$$

Where:

- G_{tot} = total capacity for the overland transport rate
- Q = water flow rate
- L = width of the flow
- D_{50} = the sediment particle diameter that is larger than 50% of the particles
- δ and a are defined in Eqs. (2.20) and (2.21).

$$\delta = \max\left[0, \frac{\tau}{\tau_c}-1\right] \tag{2.21}$$

$$a = 2.45\sqrt{\frac{\tau_c}{(\rho_s-\rho)gD_{50}}}\cdot\left(\frac{\rho_s}{\rho}\right)^{-0.4} \tag{2.22}$$

The Yalin- and Engelund-Hansen equations were initially developed to deal with sediment transport in channels. To make sure unrealistic results for overland transport are not generated, Eq. (2.23) is used to calculate the particulate sediment transport capacity. Eq. (2.24), which represents mass conservation, is also applied to all the sediment size fractions (Lukey et al., 1995).

$$G = \min[G_{tot}, Q*FPCRIT] \tag{2.23}$$

Where:

- FPCRIT = maximum sustainable sediment concentration

$$\frac{\partial(c_i h)}{\partial t}+(1-\lambda)\frac{\partial z_i}{\partial t}+\frac{\partial g_{xi}}{\partial x}+\frac{\partial g_{yi}}{\partial y} = 0 \tag{2.24}$$

Where:

- h = the water depth
- c = sediment concentration
- λ = loose sediment porosity factor
- z = loose soil depth
- g_x = sediment transport rate per unit width in the x-direction

- g_y = sediment transport rate per unit width in the y-direction
- t = time
- i = sediment size fraction.

2.5.3 Channel Erosion

According to Lukey et al. (1995), SHETRAN is capable of simulating different sediment transport processes in a channel. Included are:

- Erosion of the channel bank, caused by the flow;
- Deposition and mobilisation of sediment on the channel bed;
- Sediment convection, distributed by particle size fraction in channel;
- Sediment infiltration of fine particles into the channel bed; and
- The effect caused by channel bed armouring.

2.5.4 SHETRAN data requirements

In order to execute a SHETRAN simulation, a large amount of data for the water flow- and sediment transport component are required. The required data are listed in Table 2.4 (Ewen et al., 2011).

Table 2.4: SHETRAN water flow and sediment reqirements

Component	Data
Water flow	• Rainfall and meteorological data for all stations • Station numbers for all the columns and river links • Size and location of the columns and river links • Soil and rock types • Land-use and vegetation cover • Controlled diversions and discharge in channels • Borehole pumping rates and artificial recharge • Hydraulic potentials for subsurface (initial) • Overland and channel flow depths (initial) • Thickness and temperature of the snowpack (initial) • Hydraulic potential boundaries • Stream inflow rate boundaries • Drainage parameters and storage capacity of vegetation canopy • Ground cover distribution • Canopy- and aerodynamic resistances • The root density distribution of vegetation over depth • Storage and porosity of rocks and soil • Matric potential functions for rocks and soil • Hydraulic conductivity (unsaturated) functions for rocks and soil • Hydraulic conductivity (saturated) of rocks and soil
Sediment transport	• Raindrop size distribution • Average fall distance and drop sizes for canopy drainage • The fraction of canopy drainage that falls as leaf drip • The thickness of sediments and channel bed (initial) • Stream inflow sediment concentrations • Porosity and particle size distribution of sediment • Erodibility coefficients

The data in Table 2.4 can be collected from the following sources:

- Records from weather stations, evaporation pans, river- and rain gauges;
- Contour- or digital maps, representing the surface elevation;
- Geology and land-use maps;
- Satellite images or surface surveys (vegetation cover and land-use);
- Channel surveys (bed- and bank conditions);
- Logs (borehole drilling and soil pit digging);
- Test records (soil permeability and borehole pumping);
- Laboratory test records (particle size and hydraulic tests);
- Water supply extraction licences;
- Flood records;
- Results from experiments (hillslope erosion and tracer tests);
- Data obtained from neighbouring or similar catchments; and
- Experienced individuals.

2.6 Climate Change

The Earth's climate is a complex, interactive system consisting of the atmosphere, oceans and water bodies, snow and ice, and the interaction of living organisms with the system (IPCC, 2007). Climate is often characterised by the atmospheric component and defines it in terms of the average and variability of temperature, rainfall, and wind over a given period. Climate change is caused by its internal dynamics and external factors, which include natural phenomena (solar variation and volcanic eruptions), as well as human activity leading to changes in the atmospheric composition (IPCC, 2007).

Important parameters to consider in hydrological and soil erosion processes are rainfall, evapotranspiration, soil, and vegetation properties. Rising temperatures and changes in spatial and temporal rainfall patterns are regularly predicted by global and regional climate models. Section 2.6 gives background about climate change and the impact on significant parameters involved in the hydrological and soil erosion processes.

2.6.1 Factors influencing Earth's Climate

The climate system is driven by and responds directly to solar radiation. According to the IPCC (2007), the radiation balance of the Earth is influenced by three fundamental ways:

1. Variation in solar radiation entering the atmosphere. The variation is caused by changes in the Earth's orbit or the Sun itself.

2. Changing the quantity of solar radiation that is reflected, which is called albedo, and is influenced by changes in atmospheric particles (aerosols), cloud cover, or vegetation. Approximately 20% of the sunlight that reaches the atmosphere is reflected by clouds and aerosols, while approximately 10% is reflected by light-coloured areas of Earth's surface (deserts, snow, and ice). Major volcanic eruptions are the most significant influencer of aerosol-produced reflectivity. Rain can remove aerosols out of the atmosphere within two weeks. However, if particles were projected far above the highest clouds, aerosols can influence the climate for up to two years before falling into the troposphere and cleared by precipitation. Human-made aerosols like the burning of fossil fuels also reflects sunlight.
3. Changing the longwave radiation from Earth to outer space. The change is caused by a variation in the greenhouse gas concentration. Everything on Earth continuously releases longwave radiation. Greenhouse gases create a partial blanket, causing the natural greenhouse effect. The most significant greenhouse gases are carbon dioxide and water vapour. Human activities have increased the amount of carbon dioxide in the atmosphere by approximately 35% during the industrial era. The primary causes for the increased carbon dioxide concentrations are due to the burning of fossil fuels and the removal of forests.

For water to evaporate from the land surface or water bodies, energy is required. The energy is known as latent heat and is released when water vapour condenses in clouds. Latent heat is the primary driver for atmospheric circulation, and atmospheric circulation through the wind on the water surface is responsible for much of the ocean circulation. Ocean circulation is also influenced by changes in the ocean's surface temperature and salinity, which relates to precipitation and evaporation (Kiehl & Trenberth, 1997).

When changes in some of the characteristics of the climate system, like the temperature of the ocean and atmosphere, the size of ice sheets, or the distribution and type of vegetation, it will affect large-scale circulation features of the ocean and atmosphere. Some changes create a feedback loop. For example, when global warming resulting from an increase in greenhouse gases occur, ice and snow begin to melt, revealing darker land and water surfaces. The darker areas absorb more of the heat from the Sun, resulting in more warming and, consequently, more melting, amplifying the problem (IPCC, 2007).

2.6.2 Factors influencing Climate Change

According to the IPCC (2007), it has been observed that the influence human-activity has on climate change for the past 50 years supersedes that of natural factors. The leading causes are the changes in the amount of greenhouse gasses and aerosols in the atmosphere and changes in land use. The four

primary greenhouse gasses are carbon dioxide, methane, nitrous oxide, and the halocarbons, which include fluorine, chlorine, and bromine. During the industrial era (from about 1760), the concentration of these gases has increased significantly. According to the IPCC (2007), these increases in concentration is caused by the following:

- The burning of fossil fuel for transportation, manufacturing processes, and the heating or cooling of buildings causes an increase in carbon dioxide. Deforestation also releases carbon dioxide in the atmosphere and reduces its uptake by vegetation. Natural processes like the decay of plant material also release carbon dioxide.
- The increase in methane concentration was mainly caused by agricultural practices, natural gas distribution, and landfills but is relatively constant during the last two decades.
- Nitrous oxide is released when fertilizers are used, as well as during natural processes in soils and the ocean.
- Halocarbons have caused the hole in the ozone layer above Antarctica. The increase of the halocarbon gases was mainly caused by refrigeration agents and some industrial processes, but after their discovery in the atmosphere, international regulations were implemented to decrease emissions.
- In the atmosphere, ozone is continuously produced and destroyed by chemical reactions. The release of carbon monoxide, nitrogen oxide, and hydrocarbons by human activities have caused an increase in ozone, while halocarbons destroy ozone.
- The most important greenhouse gas is water vapour. Human activities have a minimal direct influence on the amount of water vapour in the atmosphere. Indirectly, by causing global warming, human activities have contributed significantly to the changes in the amount of water vapour in the atmosphere. A warmer climate results in an increase in the amount of water vapour.
- Aerosols in the atmosphere are either directly emitted or formed from emitted compounds. The burning of fossil fuel or biomass has caused the concentration of sulphur- and organic compounds, as well as black carbon, known as soot, to increase in the atmosphere. Some industrial processes and surface mining have also increased the amount of dust in the atmosphere. Natural contributors include sulphate and dust produced by volcanic eruptions, mineral dust from biogenic emissions from the ocean and land, and sea salt aerosols.

2.6.3 Climate Change in the South African context

The mean annual precipitation for different regions in South Africa is extremely variable, ranging from less than 50 mm to more than 3000 mm. Rainfall intensities also vary from low intensity (sometimes as snow) to high intensity (usually convection storms). Furthermore, precipitation falls on an incredibly diverse landscape, ranging from steep mountains to undulating hills to plains. The diverse landscape characteristics make it challenging to convert rainfall into overland-, base-, and storm flows. Climate change will influence the spatial patterns of hydro-climatic systems (Lynch, 2004).

South Africa has a diverse land cover distribution, which results in different hydrological responses for different regions. Different intensities of land management practices for identical land cover also plays a significant role. For example, sediment yield can be changed by a factor of four or more when overgrazed grassland is compared to well-managed conditions, or the amount of runoff can be significantly decreased by implementing conservation tillage practices and contour banks on crop fields (Schulze, 2011).

In comparison to other African countries and the rest of the world, South Africa's per capita emissions are higher. According to previous studies, the mean annual temperatures in South Africa have increased by more than 1.5 times the global average of 0.65°C over the last 50 years, and the frequency of extreme rainfall events has also increased (Ziervogel *et al.,* 2014).

The South African Long Term Adaption Scenarios (LTAS) and the Fifth Assessment Report of the IPCC have also concluded that a rise of 3°C to 6°C by 2081 to 2100 is possible in South Africa. However, the changes in precipitation in terms of magnitude and direction is still uncertain. Due to the large impact that South Africa has on climate change, a lot of research and climate modelling is conducted to contribute to mitigation procedures. One of these projects is the LTAS project that develops national and sub-national adaption scenarios to handle possible future climate conditions (Ziervogel *et al.*, 2014).

2.6.4 General Circulation Models (GCMs)

From Section 2.6.1 and 2.6.2, it is evident that the interaction between the different processes that influence Earth's climate makes it difficult to predict future climate conditions by simple, intuitive reasoning. This difficulty led to the development of GCMs, which are computer models that are mathematical representations of Earth's climate system. The physical and biogeochemical processes are numerically defined and are used to run simulations. GCMs are based on assumptions that depict the changes in the factors that influence climate change by taking natural and anthropogenic emissions into account. These assumptions are estimated by developing possible "storylines" or

emission scenarios, which describe plausible future conditions regarding population growth, economic growth, technological development, energy consumption and production, and land use (Jacob & Van den Hurk, 2009). According to the Special Report on Emissions Scenarios (SRES) and IPCC-TGICA (2007), four future conditions may be considered:

1. "A world of rapid economic growth and rapid introductions of new and more efficient technologies."
2. "A very heterogeneous world with an emphasis on family values and local traditions."
3. "A world of dematerialization and introduction of clean technologies."
4. "A world of emphasis on local solutions to economic and environmental sustainability."

In order to quantify the storylines and ensure coherency when evaluating climate change, climate modellers have developed Representative Concentration Pathways (RCPs) named after the degree of radiative forcing (watts per square meter) caused by each scenario. Included are RCP 2.6, RCP 4.5, RCP 6, and RCP 8.5, and each emission scenario can be summarized as follows:

a) RCP 2.6

The RCP 2.6 scenario is the best case for decreasing climate change that is caused by human activities. Emissions decline and reach almost zero by 2080. However, because CO_2 accumulates and can stay in the atmosphere for decades, the concentration continues to increase and reach a peak in the middle of the century. The global population also reaches a peak by the middle of the century. The use of oil decreases, but the use of other fossil- and biofuel increases. The use of renewable energy increases but remains relatively low, and global economic growth is high. For this scenario to become a reality, climate policies for all countries around the world need to be adapted, improved and implemented.

b) RCP 4.5

For the RCP 4.5 scenario, emissions reach a peak by the middle of the century (50 % higher than the early 2000s), then declines quickly during the next 30 years, after which it stabilises (50 % lower than the early 2000s). However, the CO_2 concentration continues to increase but at a lower rate. Economic and population growth are moderate and a little less than for RCP 2.6, but the energy consumption is slightly higher. Oil use is quite constant throughout the century, with an increase in nuclear power and renewable energy.

c) RCP 6

For the RCP 6 scenario, emissions reach a peak by 2060 (100 % higher than the early 2000s), after which it declines significantly but remain much higher than the early 2000s. The CO_2 concentration continues to increase through the century, with a decline in the rate after the 2060s. Population growth is reasonably high, but the lowest economic growth (between the four scenarios) is assumed for the RCP 6 scenario. Energy consumption also reaches a peak in 2060, after which it declines and remains constant at levels similar to RCP 2.6 at the end of the century. Oil use remains high, but the impact of nuclear power and biofuel is less than for the other emission scenarios.

d) RCP 8.5

The RCP 8.5 is the worst-case scenario where emissions increase at a high rate through the early and mid-century. The CO_2 concentration increases significantly by the end of the century and continues to increase throughout the next century. Energy consumption is very high (more than three times higher than present levels), with the burning of fossil fuel as the primary energy source. Oil use also increases rapidly until 2070 and then decreases significantly.

On a large scale, GCMs can effectively simulate the most significant global climate features but sometimes struggle to characterise the impacts on a local scale. Therefore, outputs from GCMs are downscaled by linking them to regional climate characteristics to obtain a finer spatial resolution (Bergant *et al.,* 2006).

2.6.4.1 Regional Climate downscaling

Dynamic- and Empirical Downscaling are two downscaling approaches that are often used to link large- and local-scale climate scenarios. Dynamic downscaling make use of high-resolution Regional Climate Models (RCMs) but still relies on the GCM to provide the boundary conditions. The RCM provides additional detail, which includes topographical features and land cover distribution. The Dynamic downscaling approach is computationally demanding (Jacob & Van den Hurk, 2009).

Empirical- or statistical downscaling uses empirical formulation from observed data to numerically present the climate system's physics. In order Year nine the regional climate change signals, it is necessary to develop a relationship between local- and large-scale atmospheric variables and applying it to the GCM output. Empirical downscaling allows for the determination of rainfall for a specific site, which can be used as input for a hydrological model (Jacob & Van den Hurk, 2009).

The University of Cape Town and the Climate Systems Analysis Group (CSAG) developed local climate values from climate change scenarios by using the empirical downscaling method on eleven GCMs and

two emission scenarios in accordance with the fifth phase of the Coupled Model Inter-comparison Project (CMIP5). Monthly rainfall and – maximum and minimum temperatures were produced in point format for the present climate, as well as the intermediate future and more distant future (Schulze *et al.*, 2014). A short overview of the different climate models are given below:

1. Model for Interdisciplinary Research on Climate - Earth System Model (MIROC-ESM)(Watanabe *et al*., 2011)

The MIROC GCM was cooperatively developed by the University of Tokyo, the National Institute for Environmental Studies (NIES), and the Japan Agency for Marine-Earth Science and Technology (JAMESTEC) and includes an aerosol-, ocean, and sea-ice component, as well as a land surface model with a river routing scheme. The MIROC-ESM adds the following:

- Atmospheric chemistry(CHASER 4.1) component;
- Nutrient-phytoplankton-zooplankton-detritus (NPZD) ocean ecosystem component; and
- Terrestrial ecosystem (SEIB-DGVM) component, which deals with vegetation change.

Watanabe *et al.* (2011) give a detailed description of each component within the model, the interaction of all the model components, and a list of all the variables exchanged between the components.

2. MIROC-ESM-CHEM (Watanabe *et al.*, 2011)

The MIROC-ESM-CHEM model is a chemistry coupled version of the MIROC-ESM model mentioned above. The MIROC-ESM-CHEM model has been successfully used to reproduce historical (1850-2005) short term variations in air temperatures and present-day climatology. Based on the Representative Concentration Pathways' (RCP) historical emissions, the model also reasonably simulates the change in column ozone and – concentration aerosols in the troposphere.

3. MIROC5 (Watanabe *et al.*, 2010)

This MIROC model was based on the MIROC3.2 model, with improvements regarding radiation, cumulus convection, cloud microphysics, aerosols, and sea ice modelling. The MIROC model incorporates an atmosphere model (CCSR-NIES-FRCGC), the CCSR Ocean Component Model (COCO4.5), and an updated terrestrial model- Minimal Advanced Treatments of Surface Interaction and Runoff (MATSIRO), that is coupled with a river model.

4. CNRM-CM5 (Centre National de Recherches Meteorologiques- Climate Model 5)(Voldoire *et al*., 2013)

The CNRM-CM5 model is an improvement of the original CNRM-CM GCM and was developed by the CNRM and the Centre Europe´en de Recherche et de Formation Avance´e (Cerfacs). The CNRM-CM5 includes an atmospheric model (ARPEGE-Climat), an ocean model (NEMO), a land surface system (ISBA), and a sea-ice model (GELATO).

5. Second generation Canadian Earth System Model (CanESM2) (CCCMA, 2017)

The CanESM2 model was developed by the Canadian Centre for Climate Modelling and Analysis and includes a physical atmosphere-ocean model (CanCM4), combined with a terrestrial carbon model (CTEM), which includes land-use change, and an ocean carbon model (CMOC). The CanESM2 model focuses on the change of the carbon dioxide burden in the atmosphere.

6. Flexible Global Ocean-Atmosphere – Land System Model (FGOALS-s2)(Zhou *et al*., 2018)

Data from the FGOALS GCM has supported numerous publications around the world and has been used as a useful tool to simulate the evolution of climate conditions on Earth. The FGOALS-s2 model consists of an atmospheric model (GAMIL2), an oceanic model (LICOM2), a terrestrial model (CLM3), and a sea-ice model (CICe4-LASG). FGOALS-s2 incorporates a Flux coupler (CCSM Coupler) to transfer data between the model components.

7. Beijing Normal University – Earth System Models (BNU-ESM) (Ji *et al.*, 2014)

The BNU-ESM model was developed at the Beijing Normal University and has successfully evaluated ocean-atmosphere interactions, carbon-climate feedback for different periods, and natural climate variability. The BNU-ESM model consists of an atmospheric model (CAM3.5), an ocean component based on the GFDL MOM4p1 Model, a terrestrial component that consists of the Common Land Model (CoLM), and it incorporates the CCSM3.5 coupling framework developed by the National Centre for Atmospheric Research.

8. Geophysical Fluid Dynamic Laboratory – Earth System Models (GFDL-ESM) (Dunne, 2013)

Two ESMs (GFDL-ESM2M and GFDL-ESM2G) have been jointly developed by the GFDL, the Department of Interior, and Princeton University, to evaluate climate and ecosystem variations by looking at natural and human-induced impacts. The models consist of the following coupling components:

- Atmospheric (aerosols, cloud physics, and precipitation);

- Terrestrial (precipitation, evaporation, runoff, rivers, streams, and lakes);
- Terrestrial ecology; and
- Ocean (wave processes, currents, and water flow, sea-ice dynamics and freshwater iceberg transport, marine ecology and biochemistry).

9. Meteorological Research Institute – Coupled Global Climate Model (MRI-CGCM3) (Yukimoto *et al.*, 2012)

The CGCM model series was developed and improved by the MRI, and the MRI-CGCM3 model consists of the following components:

- Atmosphere-land model (MRI-AGCM3) that incorporates the aerosol model (MASINGAR Mk-2), a mass-flux cumulus convection scheme, Japan Meteorological Agency's radiation scheme, a cloud scheme (MRI-TMBC), and a land surface model (HAL);
- Ocean and sea ice model (MRI.COM3); and
- Scup coupler.

Yukimoto *et al.* (2012) give a detailed description of each component, the interaction between them, as well as experimental results for different areas around the world.

10. Beijing Climate Centre Climate System Model (BCC-CSM1.1) (Tongwen *et al.*, 2014)

The BCC-CSM1.1 model has been successfully used to simulate terrestrial and oceanic carbon cycles, as well as the change of atmospheric CO_2. Simulations with the BCC-CSM1.1 model also contributed to the CMIP5 and supported the IPCC's Fifth Assessment Report (AR5). The model consist of the following coupling components:

- Atmospheric General Circulation Model (BCC-AGCM2.0);
- Land-Surface model (AVIM2) that includes plant photosynthesis and transpiration, radiation, moisture-, and heat transfer between the vegetation, soil, and air; and
- Sea ice model (SIS) that was developed by the GFDL.

2.6.5 Modelling Climate and land-use change (SHETRAN)

In order to model the impact of climate change on hydrological processes, an approach that can deal with uncertainties in the drivers (precipitation, temperature, carbon dioxide) of these processes is required. Variability within these drivers will lead to changes in evaporative demand and changes in base- and storm flow, which will influence sediment yield. The landscape component is also an important variable that is directly impacted by changes in the climatic drivers. In the hydrological system, wetlands, estuaries, and riparian zones are often wedged between the landscape and channel

component and are usually in equilibrium with the natural environment. When the upstream landscape or channel characteristics are manipulated or influenced by climate change, these ecosystems become fragile and need to be assessed (Schulze, 2011).

To simulate the hydrological consequences of climate change, a model that can represent a catchment in its possible future state is required. Current conceptual models cannot be easily used because they rely on regression relationships and require the availability of previous hydrological records to calibrate them. Their parameters also lack physical meaning and cannot be specified for future conditions (Bathurst & Purnama, 1991).

According to Schulze (2011), the following model requirements must be met to evaluate climate change and model the future hydrological and sediment yield impacts:

- The model must be able to evaluate hillslope processes and different processes that might dominate in different climate conditions;
- The model must be able to execute with a daily time step;
- The model must be physically-based and of the functional deterministic category with regards to its process evaluation, and therefore includes initial- and boundary conditions; and
- The model must be able to be modified with regards to soil properties, land cover, land use, and the topographic features of the landscape.

Therefore, a physically-based modelling system like SHETRAN is required. According to Ewen *et al*. (1996), studies to determine the impact of climate- or land-use change have been effectively done using SHETRAN. Before-and-after simulations were executed for the Rimbaud basin in France after a fire in August 1990. The study concluded that SHETRAN is a suitable modelling system to evaluate climate change, land-use change, and environmental impacts of soil erosion and pollution. The fitness for climate change modelling was also confirmed by Birkinshaw (2008). SHETRAN was also used in the Mediterranean Desertification and Land Use (MED ALUS) project. The objective of the MED ALUS project was to generate strategies to mitigate desertification trends. Climate change and the interaction between land-use changes, soil degradation, and water resources were investigated (Bathurst *et al.*, 2002).

SHETRAN has specific advantages when changes in a catchment need to be considered, or when limited historical records are available. Input parameters can be measured in the field and have a physical meaning. Therefore, the parameters can easily be changed to represent the future characteristics of a catchment. Another approach is to validate the flow components of the system by using the information from existing catchments from other climatic regions to serve as analogues for possible future conditions in the catchment under consideration (Parkin *et al.*, 1996).

3 Study area

In Section 3, an overview of the study area that was used to evaluate the future impacts of climate change on sediment yield will be defined. The physical characteristics of the catchment are obtained and evaluated. These properties will be used to calibrate the SHETRAN model for present-day conditions. The Nqweba Dam, close to Graaff-Reinet, and its catchment in the Eastern Cape, of South Africa, was selected for the study. The Nqweba Catchment lies within South Africa's semi-arid region. Approximately 30% of the country's land surface consist of semi-arid landscape.

3.1 Background

During the 1800s, no human-made dams existed in the eastern Karoo, and settlements lasted as long as the water sources or natural pools lasted. In 1843 the first dam in the Graaff-Reinet area of the Karoo was built on a farm known as Cranmere. Initially, the Cranmere dam consisted of a 1.5 m high earthen wall, catching water from the surrounding area. The construction led to new initiatives and farm development due to more permanent water supply in the arid eastern Karoo region (Palmer, 2012).

Although located close to the Sundays River, Graaff-Reinet has experienced quite a lot of problems regarding water supply. During the early 1900s, the town was supplied by two temporary dams, but they were frequently washed away, or irrigation furrows were blocked by sediment (Minnaar, 1987). The problems initiated the construction of the Van Reynevelds Pass Dam (now called Nqweba Dam) in 1921. Figure 3.1 shows a picture and the location of the Nqweba Dam. Although construction was finished in 1925, it did not provide an interminable supply of water due to irregular droughts and heavy rain. For example, although the dam spilled for the first time in 1932, it was followed by a severe drought in 1932/1933, causing the water to become brackish. The problem continued, and the reservoir became empty for the first time during the drought in the late 1950s. Besides the inconsistent water supply, extreme siltation resulted in the reduction of the storage capacity, causing the dam to overflow more often (Minnaar, 1987).

Figure 3.1: Picture and location of Nqweba Dam at Graaff-Reinet

Excessive siltation of reservoirs and reduced storage capacity is one of the major problems of dams in the Karoo. Excessive siltation is due to the high erodibility of the soil and limited vegetation cover in the semi-arid regions. According to the Department of Water and Sanitation (DWS, 2011), by April 2011, the Nqweba Reservoir has lost approximately 43% of its storage capacity due to sedimentation. This drastic sedimentation and loss of reservoir storage capacity are illustrated in Figure 3.2 and Figure 3.3. Figure 3.2 illustrates a long section through the deepest channel in the Nqweba Reservoir for 1925 and 2011. Figure 3.3 illustrates a cross-section at the dam.

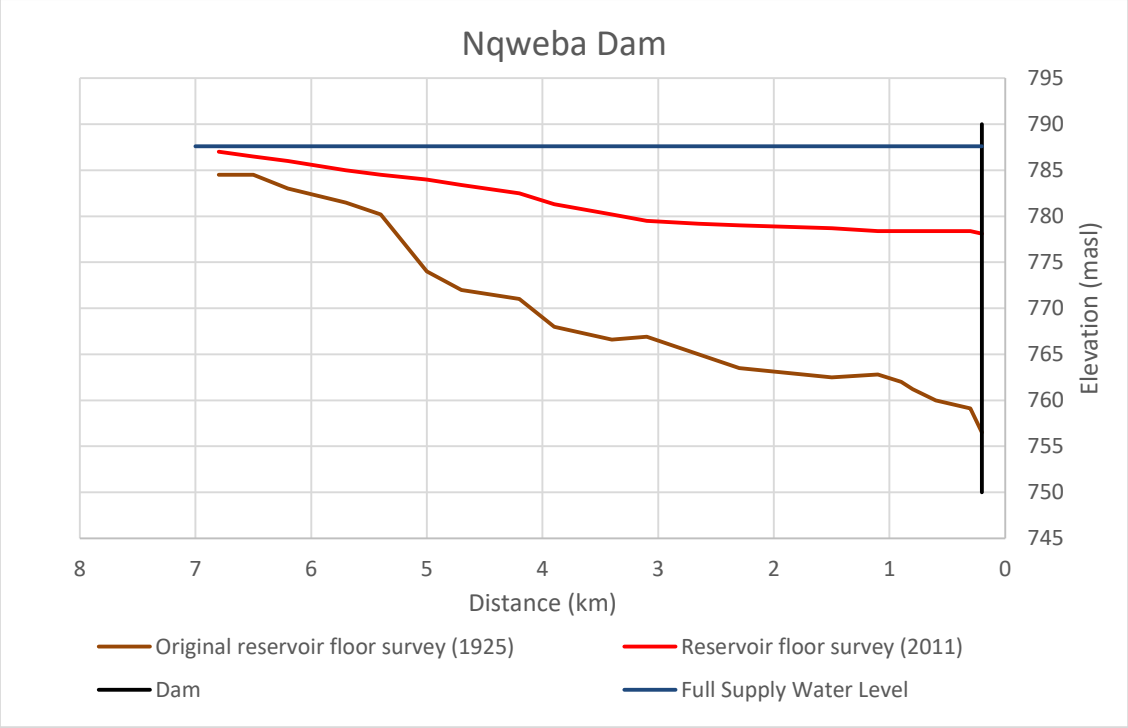

Figure 3.2: Long section of Nqweba Reservoir through the deepest channel (DWS, 2011)

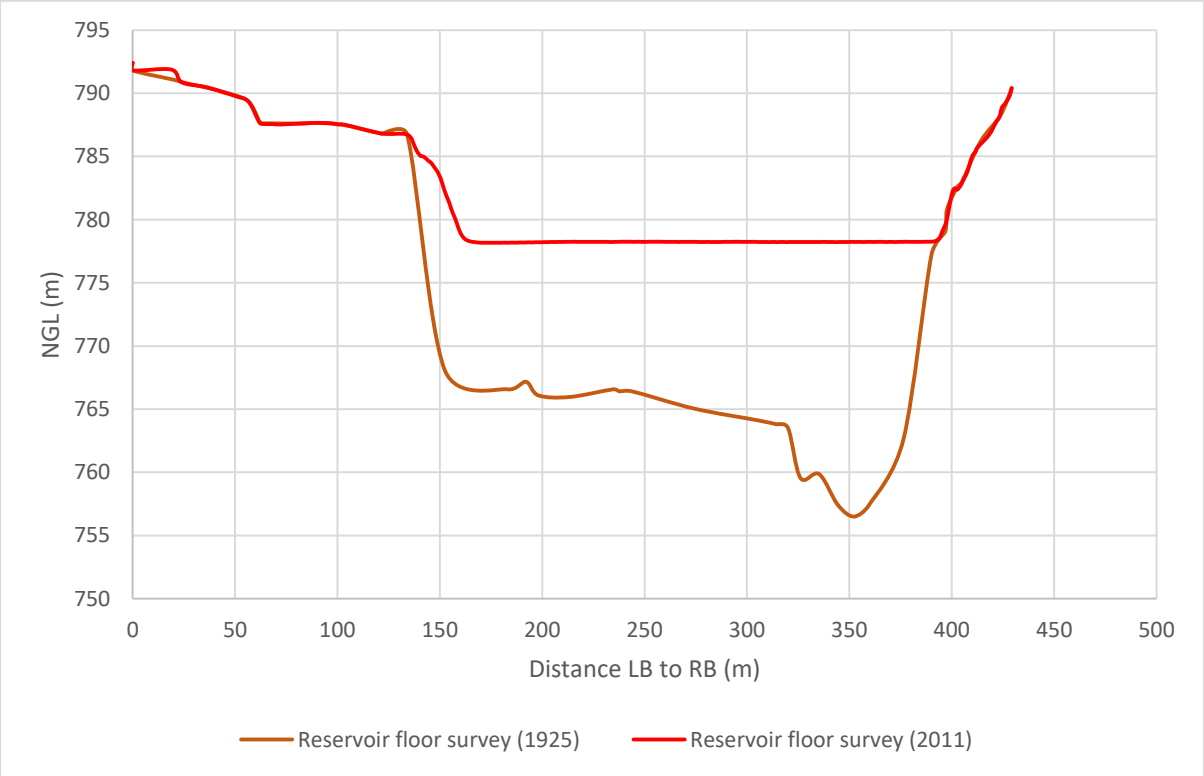

Figure 3.3: Cross-Section at Ngweba Dam (DWS, 2011)

3.2 Catchment Characteristics

3.2.1 Catchment Delineation

The catchment area for the Nqweba Dam is part of the Sundays River Catchment, which lies within the Fish to Tsitsikama Water Management Area. According to DWS (2011), the effective catchment area is approximately 3681 km^2. The location of the Nqweba Catchment is illustrated in Figure 3.4. A Digital Elevation Model (DEM) (Figure 3.5) illustrates that the elevation varies from 755 masl to 2467 masl. The watershed, primary, and secondary river networks and the location of the Nqweba Reservoir within the network are also illustrated in Figure 3.5.

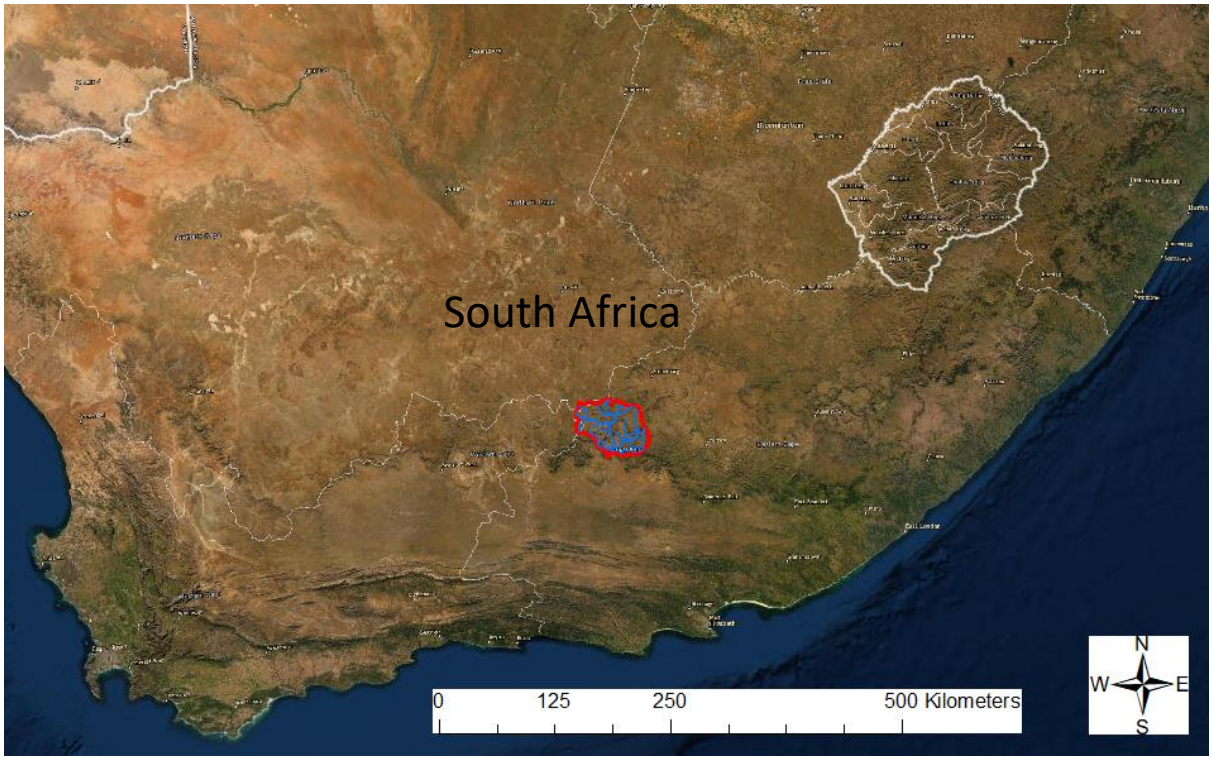

Figure 3.4: Location of Nqweba catchment

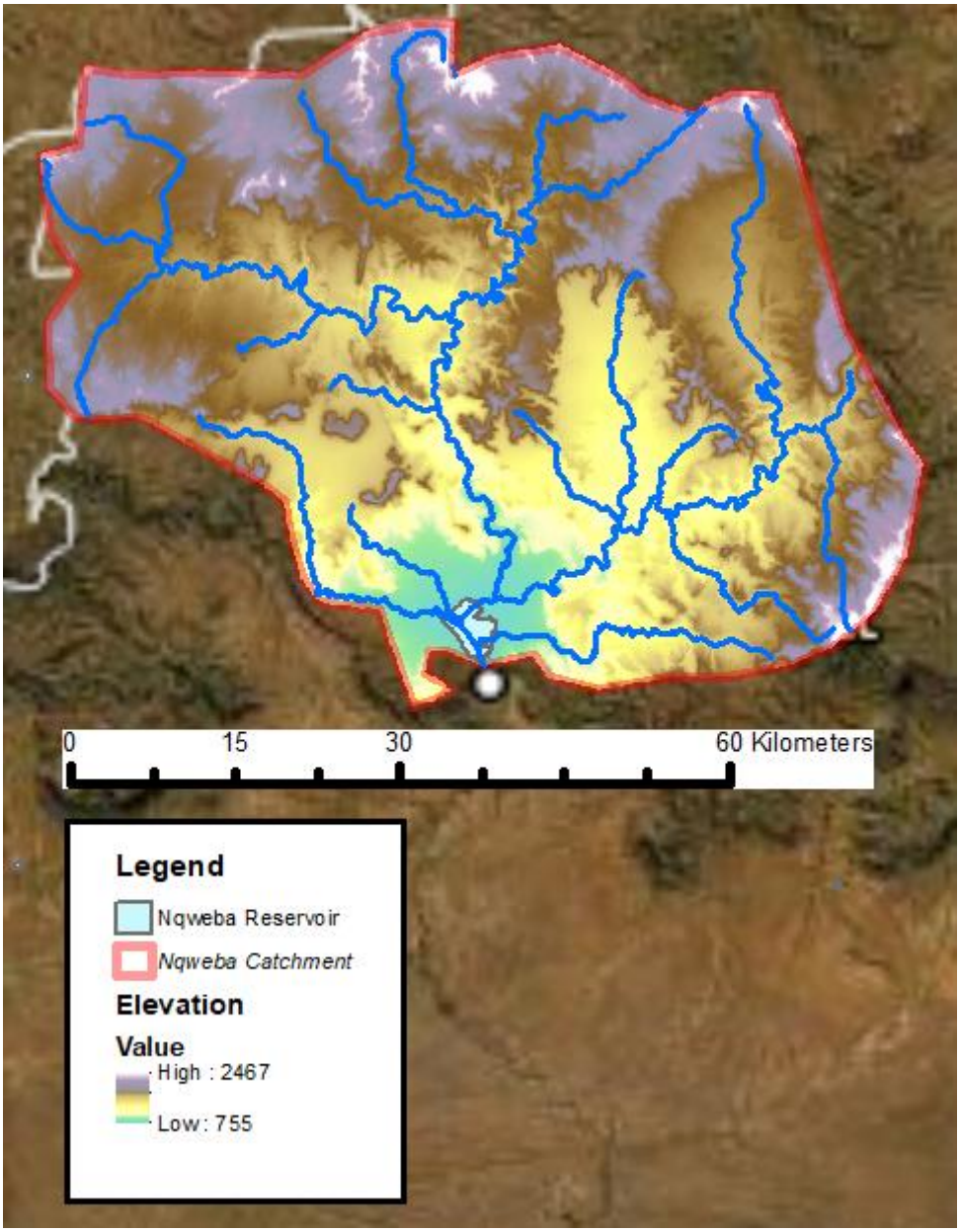

Figure 3.5: DEM for Nqweba Dam catchment (USGS, 2020)

3.2.2 Land Cover Distribution

According to the South African National Biodiversity Institute (SANBI, 2012), three land covers dominate the Nqweba Dam catchment. Included are Camdeboo Escarpment Thicket, Upper Karoo Hardeveld, and Karoo Grassland. Table 3.1 summarize the landscape, vegetation, geology, and soil characteristics of the land cover in the Nqweba Dam catchment. Detail regarding the soil properties will be discussed in Section 3.2.3. Pictures of the different land covers can be seen in **Appendix C**. The spatial distribution of the land cover is illustrated in Figure 3.6.

Table 3. 1: Land Cover in the Nqweba Dam catchment (SANBI, 2012)

Land Cover	Landscape	Vegetation	Geology and soil
Camdeboo Escarpment Thicket	Rugged, broken ridges and mountain slopes	2-3 m Succulent thicket (Spekboom); Small trees and Shrubs	Sand-and mudstone of the Permian Adelaide Subgroup; Dykes of Jurassic Karoo dolerites; Skeletal soils of Mispah form
Upper Karoo Hardeveld	Steep slopes of butts, mesas, and small hills; Large boulders and stones	Sparse dwarf Karoo shrubs, Succulent shrubs, and drought-tolerant grasses	Primitive, skeletal soils; mudstone and arenites; Jurassic dolerite dykes and sills; dolerite boulder slopes
Karoo Grassland	Mountain summits; low mountains and hills	Thin, tussock grasslands; Graminoids (herbaceous plants with grass-like features); low shrubs	Shallow soils; mudstone and sandstone of the Beaufort Group; Dolerite intrusions on some ridges

A land cover distribution obtained from the European Space Agency (ESA) was also obtained for 2016 and is illustrated in Figure 3.7. This distribution illustrates the basic vegetation types for the Nqweba Dam catchment.

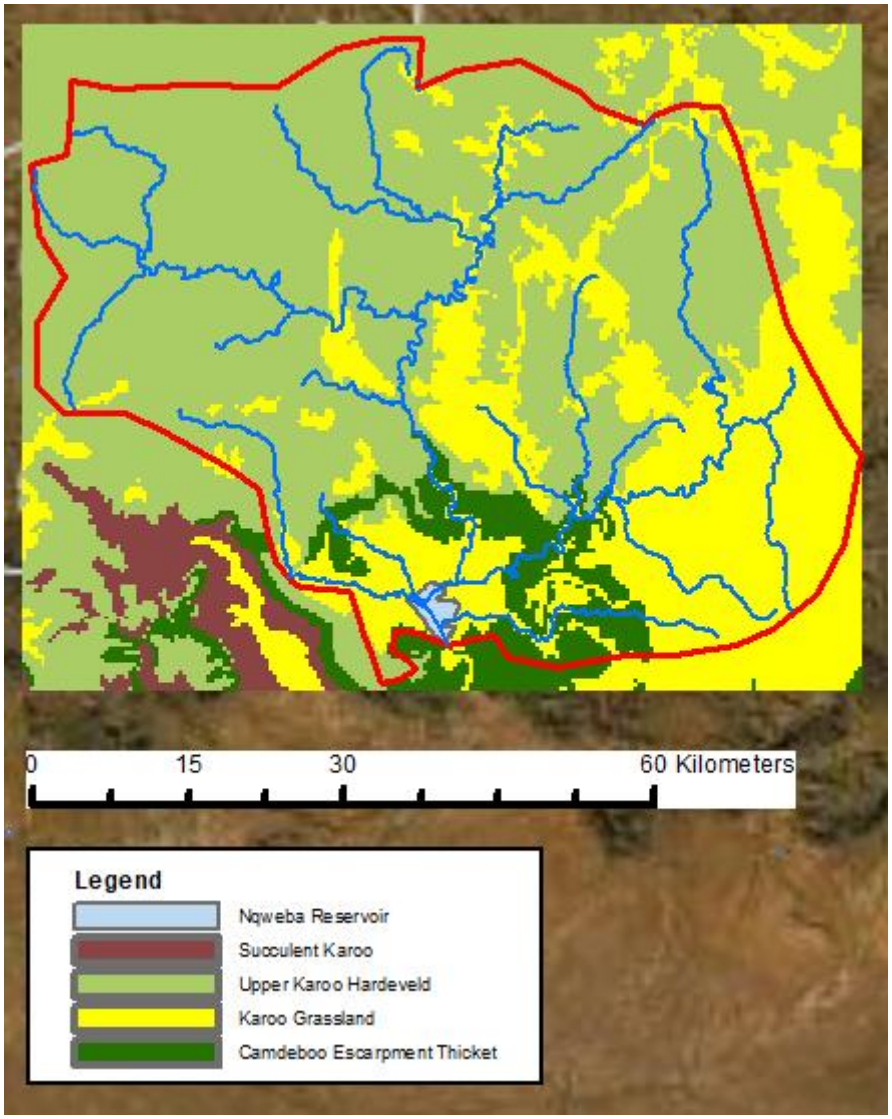

Figure 3.6: Land Cover distribution for Nqweba Dam catchment(SANBI, 2012)

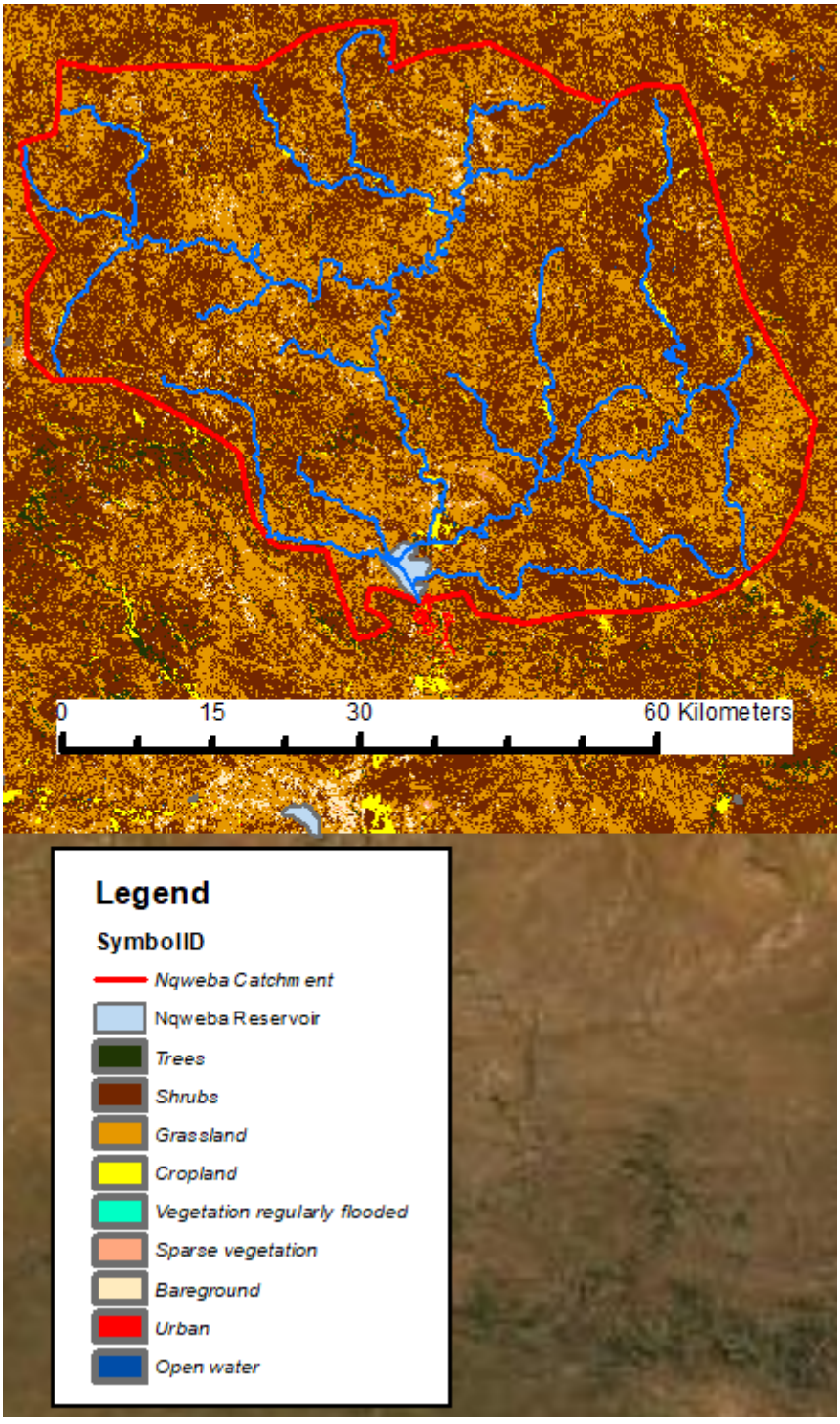

Figure 3.7: ESA year 2016 Land Cover (ESA, 2016)

3.2.3 Soil Properties

In a vegetation study conducted by Palmer (1989) in the Karoo Nature Reserve, which lies within the Nqweba Dam catchment, characteristics regarding the soil depth were obtained. Palmer (1989) determined that the soil depth varies between shallow Mispah-Rock complex (0.03 m to 1.2 m) to moderate depth (1.2 m to 2.3 m) and deep (2.3 m to 5 m) calcareous duplex soils of the Shigalo-

Limpopo Association. The Mispah-Rock complex is often related to the dolerite sills and dykes in the Beaufort Group that intrudes the sedimentary layers. In general, the A-horizon of the soil within the catchment displays an orthic topsoil consisting mainly of the Lithic soil group and traces of the Duplex, Oxidic, and Cumulic soil groups (Fey, 2010).

Dolerite boulders that often overlay the pediment soils improve soil quality by enhancing the water-holding capacity and reducing the soil's alkalinity. The pediment soils are weakly structured, apedal, freely drained soils that have been deposited as alluvium on impermeable sandstone. The pediment soils are susceptible to sheet and gully erosion, which is intensified if the vegetation cover is reduced (Ellis & Lambrechts, 1986).

3.2.3.1 Physical survey

Twelve points were identified within the catchment, and soil samples were obtained for each point. The location of the samples can be seen in Figure D-1 in **Appendix D**. The grading according to particle size were obtained for each sample, and the percentage clay, silt, sand, and gravel were determined according to the particle size classification described in Section 2.1.3 and Table A-1 in **Appendix A**. The topsoil in the Nqweba Dam catchment varies from Clay-Loam to Sandy-Loam to Loamy-Sand. Table 3.2 summarize the grading, d_{50} particle size and soil texture for each sample and Figure 3.8 illustrates the spatial distribution of the different soil types within the Nqweba catchment. The detailed grading for Point P1, P4, P5, and P7 is given in **Appendix D**.

Table 3.2: Soil sample grading and texture

Sample	Clay (%)	Silt (%)	Sand (%)	Gravel (%)	d50 (mm)	Soil Texture
P1	13	24	62	1	0.0790	Sandy Loam
P2	7	30	56	7	0.1050	Sandy Loam
P3	18	22	51	9	0.0840	Sandy Loam
P4	31	31	37	1	0.0440	Clay Loam
P5	6	10	84	0	0.1900	Loamy Sand
P6	5	15	63	17	0.3000	Sandy Loam
P7	16	10	21	53	2.8000	Clay loam
P8	13	30	54	3	0.0690	Sandy Loam
P9	8	10	62	20	0.6900	Sandy Loam
P10	11	9	37	43	1.2000	Clay Loam
P11	10	19	60	11	0.15	Sandy Loam
P12	11	14	60	15	0.23	Sandy Loam

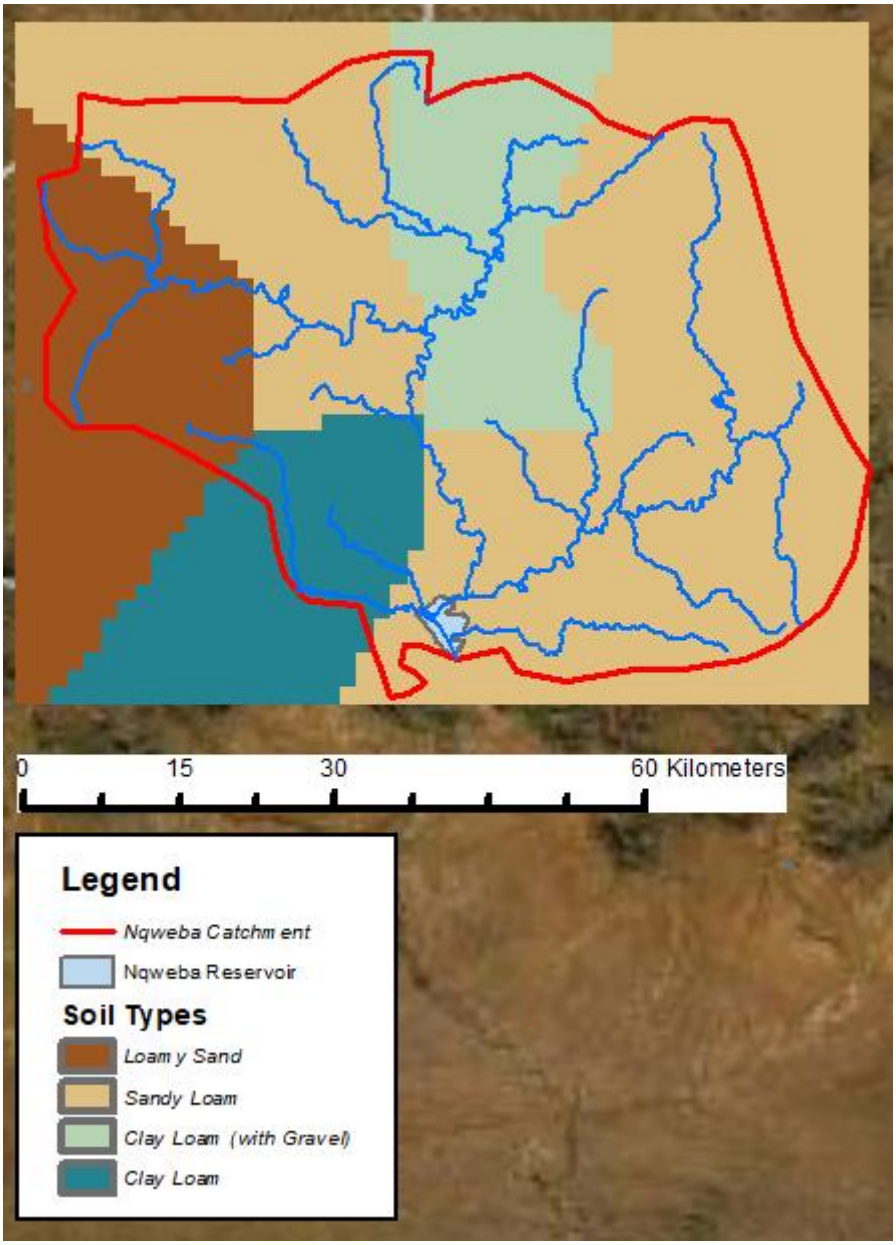

Figure 3.8: Spatial distribution of different soil types in the Nqweba Dam catchment

3.2.4 Climate

According to Palmer (1989), the climate is described as semi-arid, with a third of the Mean Annual Precipitation (MAP) falling during February, March, and April (the hottest months of the year). Regular fog also occurs during these months over the high-lying areas, providing moisture availability. During the summer months, the maximum air temperature may exceed 43^{O}C. During winter (May-August), temperatures may fall below -3^{O}C, with regular frost and snow occurring on the high-lying plateau.

3.2.4.1 Rainfall data

The annual precipitation is highly variable in the area, and low total annual precipitation with high evaporation losses causes low total annual runoff. Runoff is also characterised by sudden flash floods caused by thunderstorms. According to Grenfell *et al.* (2014), extreme rainfall events are responsible for a significant amount of the MAP. For example, extreme rainfall events in 1909, 1931, 1961, and 1974 contributed to more than 30 % of the annual precipitation.

Observed daily rainfall data for two stations within the borders of the drainage basin were available, as well as rainfall data from two stations just outside the catchment. The MAP for each station's available data was calculated and compared with neighbouring stations. It was concluded that the rainfall data is fairly reliable because the neighbouring rainfall records correspond well. A summary of the stations is given in Table 3.3. A Thiessen polygon was developed from the point data, and the spatial contribution for each station is illustrated in Figure 3.9.

Table 3.3: Rainfall station details

Rainfall station	Latitude	Longitude	Available data	MAP (mm)
GRAAFF-REINET	32°11'35.88"S	24°32'35.16"E	1925-2020	333
BLOEMHOF	32° 2'36.96"S	24°40'26.04"E	1900-2020	330
COETZEESKRAAL	32° 0'0.00"S	24° 7'22.08"E	1932-2020	326
VANDERWALTSHOEK	32° 7'58.80"S	24°15'0.00"E	1928-2020	332

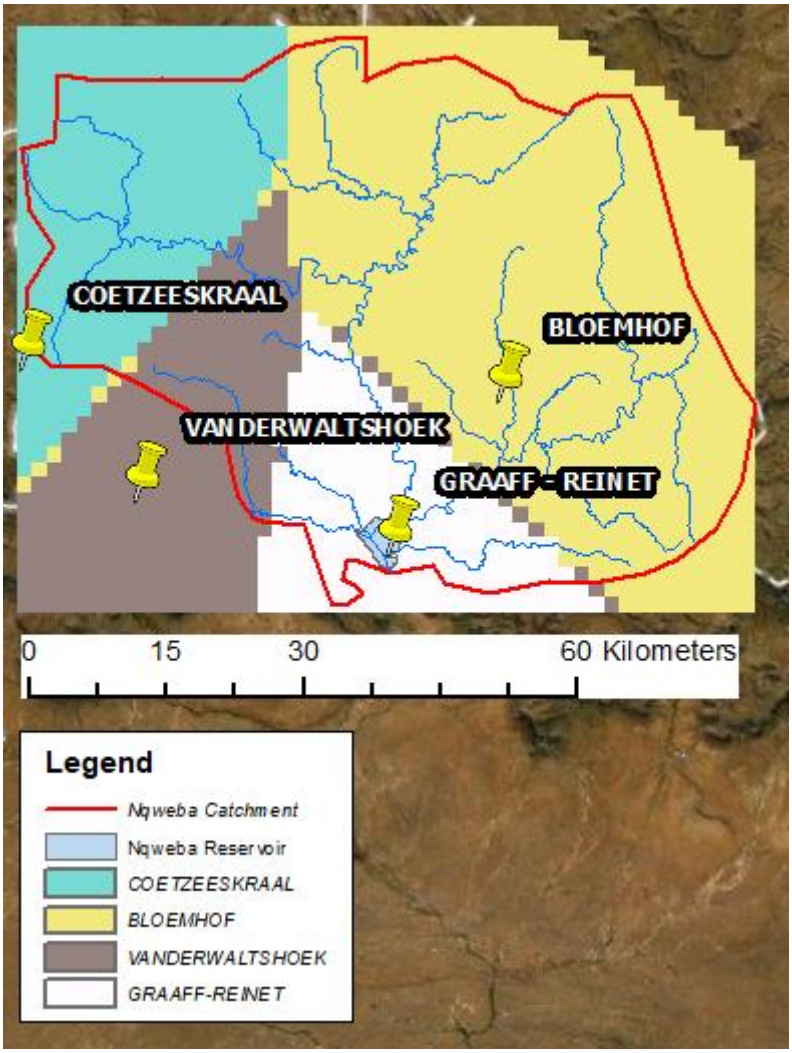

Figure 3.9: Spatial Rainfall distribution of contributing stations

3.2.4.2 Evaporation data

For the Nqweba Dam catchment, S-Pan daily evaporation data at the dam was obtained from the Department of Water and Sanitation (DWS). However, SHETRAN requires potential evaporation as input values. Potential evaporation was calculated by applying the S-Pan Factors given in Table 3.4 for different months. The average daily evaporation for each month is given in Figure 3.10. The potential evaporation in the Nqweba Dam catchment varies from 7 mm/day in December and January to 2.3 mm/day in June. The S-Pan evaporation and the potential evaporation from 1932 to 2019, used in the SHETRAN model, are given in Figure 3.11.

Table 3.4: Monthly S-Pan Factors

Month	S-Pan Factor
October	0.81
November	0.82
December	0.83
January	0.84
February	0.88
March	0.88
April	0.88
May	0.87
June	0.85
July	0.83
August	0.81
September	0.81

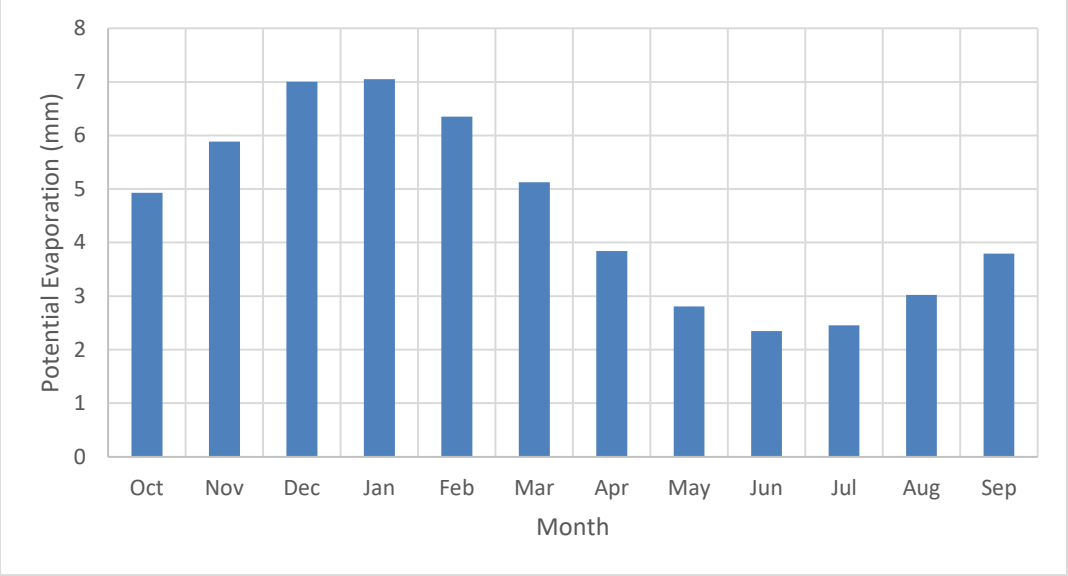

Figure 3.10: Average daily Potential Evaporation (1932-2019) for each month

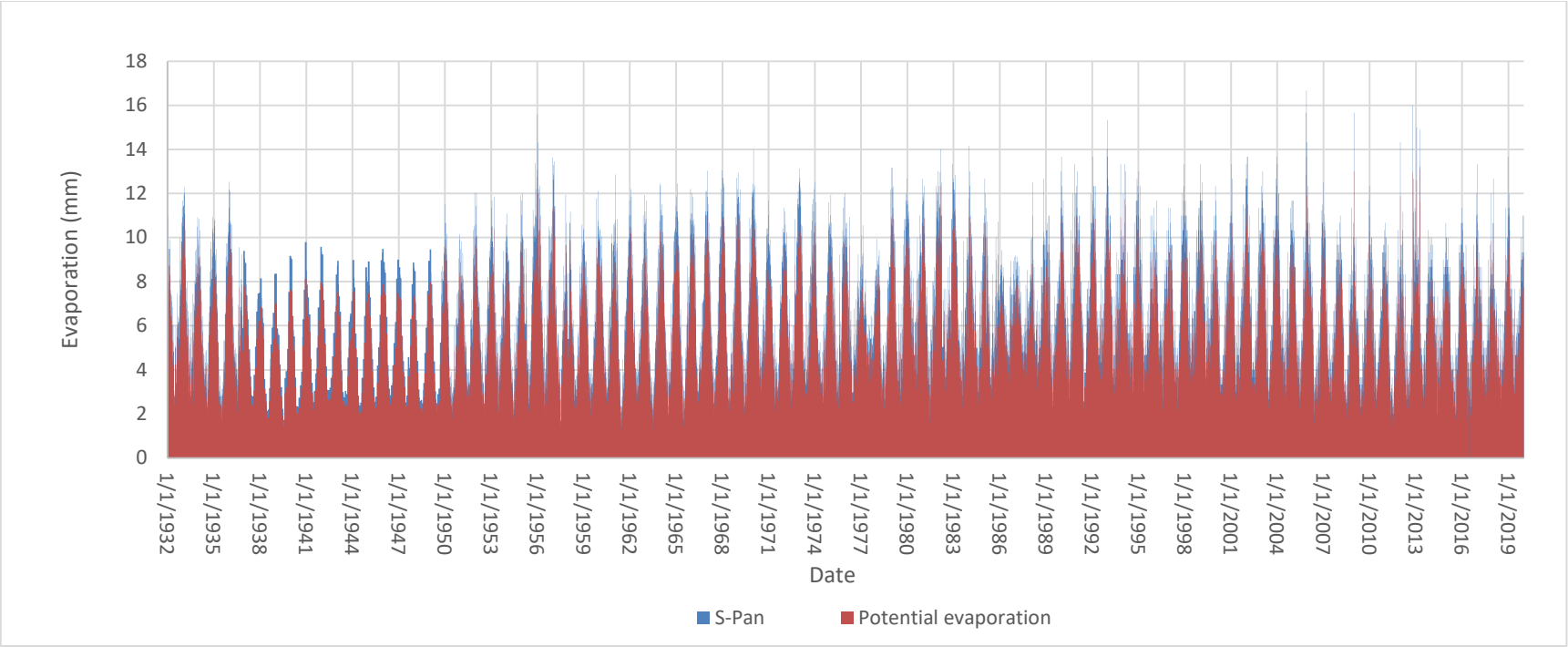

Figure 3.11: S-Pan and Potential evaporation in Nqweba Catchment

3.2.5 Streamflow data

Observed daily gauge plate readings for the Nqweba Dam was obtained from the DWA and illustrated in Figure 3.12. The only missing data was from June 1976 to April 1978 and June 1978 to August 1978. In order to minimize errors caused by missing data, streamflow data from 1980 to 2020 was used during calibration.

The inflow required for calibration purposes was calculated from observed dam mass balance data by taking the change in volume, rainfall on-, and evaporation from the reservoir surface and water withdrawal into account. Figure 3.13 illustrates the calculated daily streamflow into the Nqweba Reservoir. The high variability in rainfall causes high variability in runoff and streamflow. Table 3.5 summarizes the frequency of calculated flood peaks greater than 50 m^3/s for three 25-year periods. From Table 3.5, it can be seen that the frequency of streamflow events greater than 50 m^3/s for the past 25 years (1995 to 2020), are considerably lower than for the 1925 to 1950 and 1951 to 1976 periods.

Table 3.5: Frequency of flood peaks greater than 50 m^3/s

Period	Frequency (flood peaks greater than 50 m^3/s)
1925-1950	31
1951-1976	28
1995-2020	14

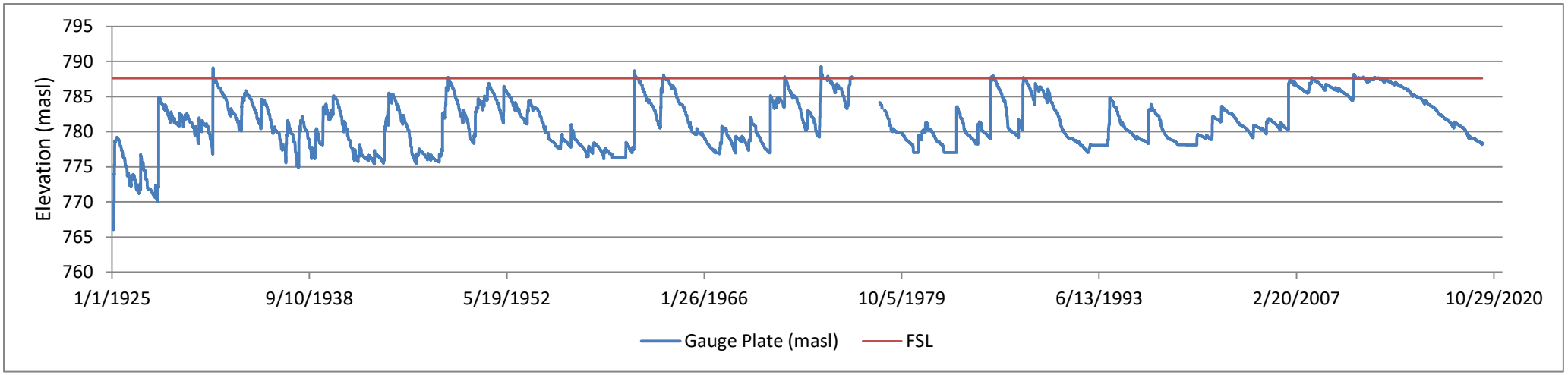

Figure 3.12: Observed water levels for the Nqweba Reservoir

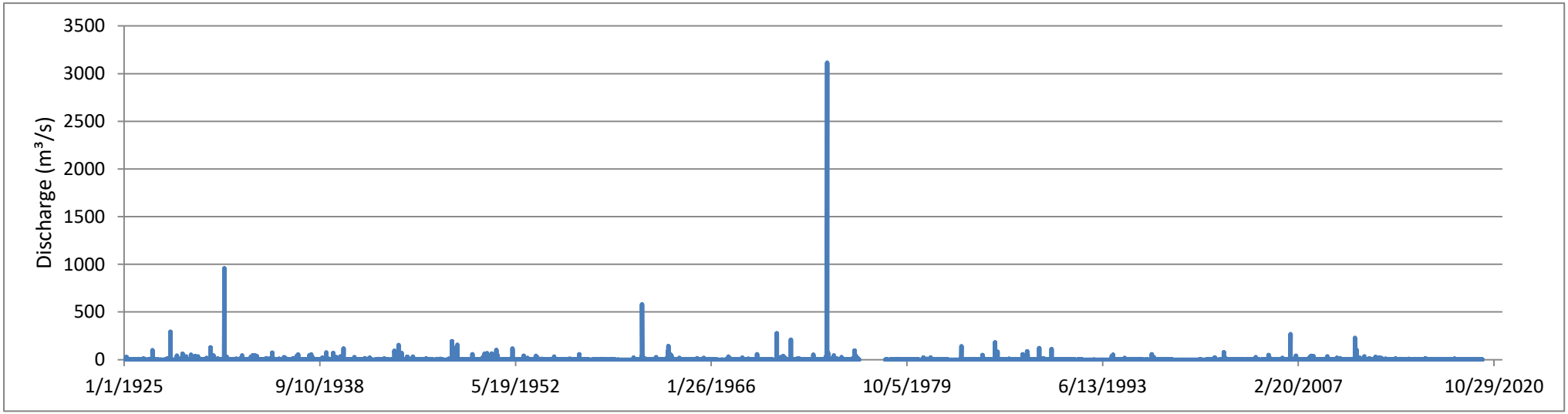

Figure 3.13: Calculated inflow at Nqweba Reservoir

Because the streamflow is not actual measurements but is calculated from a dam mass balance, it is assumed that errors in the daily flood peaks might occur. However, it is assumed that the monthly mass balance is correct. Floods are important for sediment transport simulations and in order to give the streamflow data more credibility, the catchment's response to rainfall is evaluated by comparing the rainfall-runoff events of the three largest flood peaks to three smaller events. From Figure 3.13, the three largest flood peaks are the following:

a) For 2 January 1932, a flow of 3116 m^3/s was calculated.
b) For 28 March 1961, a flow of 972 m^3/s was calculated.
c) For 5 March 1974, a flow of 1060 m^3/s was calculated.

In order to evaluate the catchment response, floods a), b) and c) are compared to the following smaller floods:

d) For 29 March 1928, a flow of 290 m^3/s was calculated.
e) For 28 August 1970, a flow of 275 m^3/s was calculated.
f) For 4 August 2006, a flow of 269 m^3/s was calculated.

The analysis is done by looking at the accumulated rainfall in the catchment five days before the streamflow event and the accumulated rainfall in the catchment three months and one year before the flood event. The accumulated rainfall is calculated as the average for all four rainfall stations discussed in Section 3.2.4.1. The results are summarized in Table 3.6

Table 3.6: Comparison of rainfall-runoff events

Flood	Date	Calculated streamflow(m^3/s)	Accumulated rainfall five days before flood (mm)	Accumulated rainfall 3 months before flood (mm)*	MAP for the year leading up to flood (mm)*
(a)	Jan 1932	956	102	58	355
(b)	Mar 1961	580	87	134	292
(c)	Mar 1974	3116	101	256	503
(d)	Mar 1928	290	101	66	161
(e)	Aug 1970	275	103	22	185
(f)	Aug 2006	269	92	63	342

* The accumulated rainfall three months and a year before the flood event excludes the rainfall recorded for the five days before the flood event.

3.2.5.1 Comparison of flood (a) and flood (d)

It is evident that flood (a) is almost six times larger than flood (d). Both floods are caused by approximately the same rainfall event (five days before the flood). The total average rainfall for the three months leading up to the floods also correlates well. However, the MAP for the year leading up to flood (a) is significantly higher than that of flood (d). Consequently, the following remarks can be made:

- The period between the floods are relatively small (four years), and therefore the impact of significant climate change can be excluded.
- The year leading up to flood (d) was significantly drier than the year leading up to flood (a).
- Although a dry year might cause a decrease in vegetation cover, the soil's characteristics and dryness result in less runoff due to infiltration and a lower water table.
- Flood (a) is recorded at the beginning of the rain-season (January), while flood (d) is recorded closer to the end of the rain-season (March). One of the dominant vegetation types of the Nqweba Dam catchment is grass, which grows during the rain- season. This means that it is possible that there was significantly less vegetation cover during flood (a), increasing runoff.
- It is also possible that a dry year can cause farm dams to be relatively empty. When a flood event occurs, farmers would probably intercept a significant portion of runoff, decreasing the amount of water ending up in the reservoir. The opposite can be valid for a wet year – farm dams are already relatively full when the flood event occurs, and most of the runoff ends up in the Nqweba Reservoir.

3.2.5.2 Comparison of flood (b) and flood (f)

From Table 3.6, it can be seen that flood (b) is almost four times larger than flood (f). The rainfall event five days before the measurement for both floods is similar. However, it can be noted that the MAP for the year leading up to flood (b) is lower than that of flood (f), but the average rainfall in the catchment for the three months before flood (b) is significantly higher (more than double) than that off flood (f). Consequently, the following remarks can be made:

- The period between the floods is relatively large (45 years), and therefore it is possible that climate change affected the catchment response. It is possible that higher evapotranspiration during later years (the 2000s) resulted in lower soil moisture conditions and an increase in water table depth, which influences infiltration and decreasing runoff.

- Although a larger MAP is recorded for the year before flood (f), the fact that the rainfall three months before the measurement is much less than that recorded before flood (b) concludes that the latter has a more significant influence than the former.
- Due to the high rainfall three months before flood (b), it is possible that farm dams were already relatively full by the time the flood event occurs and the opposite could be true for flood (f). During the 45 years between the floods, it is also highly probable that the number of farm dams has significantly increased, resulting in less water ending up in the Nqweba Reservoir.

3.2.5.3 Comparison of flood (c) and (e)

From Table 3.6, it can be seen that flood (c) is much larger than flood (e). Both floods were caused by approximately the same rainfall event. However, it is immediately evident that significantly lower rainfall was recorded during the three months - as well as one year before the flood (e) than flood (c). The following remarks can be made:

- The period between the floods is relatively small (four years), and therefore it is assumed that the impact of climate change can be excluded.
- The MAP preceding flood (c) (503 mm) is significantly higher than the average MAP (330 mm) of the Nqweba catchment, and the MAP preceding flood (e) (185 mm) is significantly lower than the average MAP for the catchment.
- The same arguments in Sections 3.2.5.1 and 3.2.5.2 with regards to farm dams are probable for this comparison.

3.2.5.4 Summary

The analysis was done to evaluate the catchment response to rainfall for significant rainfall and streamflow events by comparing it with smaller floods. It is concluded that similar rainfall events can have extremely variable catchment responses, depending on conditions preceding the actual event. Low MAP preceding an extreme rainfall event will result in lower gauge plate readings in the Nqweba Reservoir. Although low MAP would reduce vegetation growth and – cover, increasing runoff and streamflow, the presence of numerous empty farm dams can intercept a large portion of rainfall from extreme events. It was also concluded that low MAP could reduce the soil moisture and lower the water table, causing more water to infiltrate and less to end up in the Nqweba Reservoir.

Although there are numerous explanations for the variability in inflow (caused by approximately the same rainfall event) into the Nqweba Reservoir, it is still important to take the following points into account before using the inflow data for the SHETRAN calibration:

- The inflow data is not actual streamflow measurements but was calculated using mass balance and gauge plate readings (water level in the reservoir). The accuracy of these calculations is susceptible to errors, because there was no spillage for the greater part of the dam's history, and the calculations had to rely on the change in volume; and
- Rainfall data from limited stations within the catchment are available. Therefore, some rainfall events, especially in the Northern parts of the catchment (Ref. Figure 3.9), may be absent or inaccurate.

3.3 Estimated sediment yield for Nqweba Catchment

According to Di Silvo & Basson (2008), reservoirs trap approximately 97% of the catchment sediment yield, causing sediment accumulation and loss in reservoir storage. Therefore, it is possible to calculate sediment yield by comparing the changes in water storage capacity between two or more reservoir surveys. Table 3.7 summarizes the change in storage capacity for the Nqweba Reservoir from 1925 to 2011 and the accumulated sediment volume.

Table 3.7: Nqweba Reservoir survey data (DWS, 2011)

Date	Years	Storage capacity at FSL (Mm^3)	Sediment Volume (Mm^3)
1925	1	78.824	0.000
1931	6	75.700	3.124
1935	10	69.400	9.424
1941	16	64.900	13.924
1946	21	62.800	16.024
1953	28	58.200	20.624
1957	32	57.074	21.750
1966	41	53.060	25.764
1973	48	51.827	26.997
1978	53	47.426	31.397
1998	73	46.369	32.454
2011	86	44.718	34.106

In order to account for the consolidation of the deposited sediment, the available data is plotted on a log scale (Figure 3.14) because it is assumed that there is a logarithmic relationship between sediment

deposit volume and time (Rooseboom *et al.*, 1992). Using the equation for the trend line (Eq. (3.1)) the sediment volume in the reservoir after T years can be calculated:

$$\mathbf{V_T = 11.985ln(T) - 18.905} \quad (3.1)$$

Where:

- V_T = Sediment volume in the reservoir after T years.

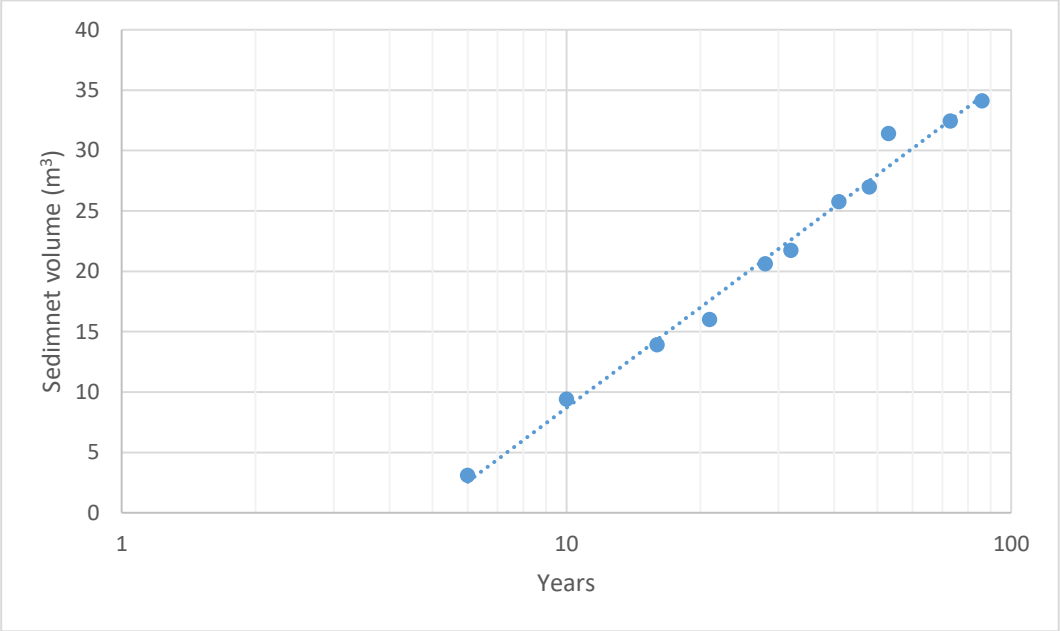

Figure 3.14: Cumulative sediment volume in Nqweba Reservoir

The average sediment yield for a period n is calculated with Eq. (3.2).

$$\mathbf{S_y = \frac{\rho_T V_T - \rho_{T-n} V_{T-n}}{n A_e}} \quad (3.2)$$

Where:

- S_y = Sediment yield (t/km^2/a)
- V_T = Sediment volume in the reservoir after T years
- A_e = Effective catchment area
- ρ = sediment density.

Observed sediment densities in reservoirs can vary significantly, and to calculate the sediment yield, predicting the correct sediment densities for different periods are essential. According to Basson & Rooseboom (1997), the sediment density in a reservoir is a function of the following:

- The overburden weight;
- Sediment particle size and distribution;
- Degree of exposure to drying (when the reservoir is empty);
- Permeability; and
- Age of deposits and consolidation rate.

Reservoirs in South Africa are classified according to reservoir operation, and the different types are given in Table 3.8. For these reservoir types, the initial densities of deposited sediment are summarized in Table 3.9, and the consolidation coefficients are given in Table 3.10 (Basson & Rooseboom, 1997).

Table 3.8: Reservoir operation classification (Basson & Rooseboom, 1997)

Reservoir type	Reservoir operation
1	Sediment is always- or nearly submerged
2	Usually moderate to significant reservoir drawdown
3	The reservoir is usually empty

Table 3.9: Initial densities of deposited sediment (Basson & Rooseboom, 1997)

Reservoir type	ρ clay (kg/m³)	ρ silt (kg/m³)	ρ sand (kg/m³)
1	416	1120	1550
2	561	1140	1550
3	641	1150	1550

Table 3.10: Sediment consolidation coefficients (Basson & Rooseboom, 1997)

Reservoir type	K clay	K silt	K sand
1	256	91	0
2	135	29	0
3	0	0	0

By taking continuous sedimentation and compaction into account, the average density of deposited sediment after T years can be calculated with Eq. (3.3) (Miller, 1953).

$$\rho_T = \rho_0 + 0.4343 K_0 \left[\frac{T}{T-1}(\ln T) - 1\right] \quad (3.3)$$

Where:

- ρ_T = sediment density after T years of compaction
- ρ_0 = initial sediment density

- $K_0 = K_{clay} * \text{clay fraction} + K_{silt} * \text{silt fraction} + K_{sand} * \text{sand fraction}.$

The Nqweba Reservoir is classified as a type 2 reservoir. According to a DWS survey conducted by Braune (1984), where 42 samples were taken, the observed bed sediment particle distribution was 60 % clay, 35 % silt, and 5 % sand, and the average sediment density for 1960 and 1980 was 1120 kg/m^3 and 1147 kg/m^3 respectively. Using the survey data in Table 3.7 for the same years, and Eq (3.3), the sediment densities are calculated and summarized in column four of Table 3.11. It was determined that a scale factor of 1.385 needs to be applied to the consolidation coefficients in Table 3.10 to obtain the calibrated sediment density given in column six of Table 3.11.

Table 3.11: Sediment density due to consolidation

Year	Dam age (years)	Type 1	Type 2: Calc Sediment density (kg/m3)	DWS obs>0.9m (1.8-3km from dam) (kg/m)	Type: calibrated (kg/m3)	Difference
1960	35	933	918	1120	1110	-0.91%
1980	55	967	935	1147	1157	0.89%

Therefore, using the survey data from 1925 to 2011 in Table 3.7, Figure 3.14 for 2020, and Eqs. (3.2) and (3.3), the calibrated sediment densities and estimated sediment yield for the Nqweba Dam catchment are calculated and summarized in Table 3.12. The change in sediment yield over time is also illustrated in Figure 3.15. Looking at the results, it is evident that the sediment yield for the Nqweba Dam catchment has generally declined over the years, except for the 1973-1978 period (extreme flood event occurred in 1974 – Ref. Figure 3.13).

Although a decline in sediment yield is uncommon, similar trends have been observed in the Orange River, as illustrated in Figure 3.16. Possible theories for the decline in sediment yield for the Nqweba Dam catchment include the following:

- Alternative land-use practices (changing from livestock- to game farming) resulted in improved vegetation cover and decreased erosion;
- The construction of numerous farm dams within the catchment prevents sediment from reaching the reservoir by acting as sediment traps; and
- Climate change caused changes in catchment response and resulted in less runoff and sediment yield.

These theories will be evaluated by applying the SHETRAN Model. It can also be noted that the current sediment yield observed for the Nqweba Dam catchment (56 t/km^2/a) is relatively low

compared to some other locations in South Africa. Examples of higher sediment yield regions are given in Table 3.13.

Table 3.12: Calculated bed sediment density in Nqweba Reservoir and estimated sediment yield for catchment

Year	Calibrated Sediment density (kg/m^3)	Sediment yield (t/km^2/a)[1]
1925	813	0
1931	941	161
1935	987	435
1941	1031	231
1946	1058	142
1953	1087	214
1957	1101	104
1966	1126	154
1973	1143	72
1978	1153	293
1998	1187	32
2011	1204	54
2020	1215	56

[1]The sediment yield is calculated as an average for the period between reservoir surveys (years in the first column).

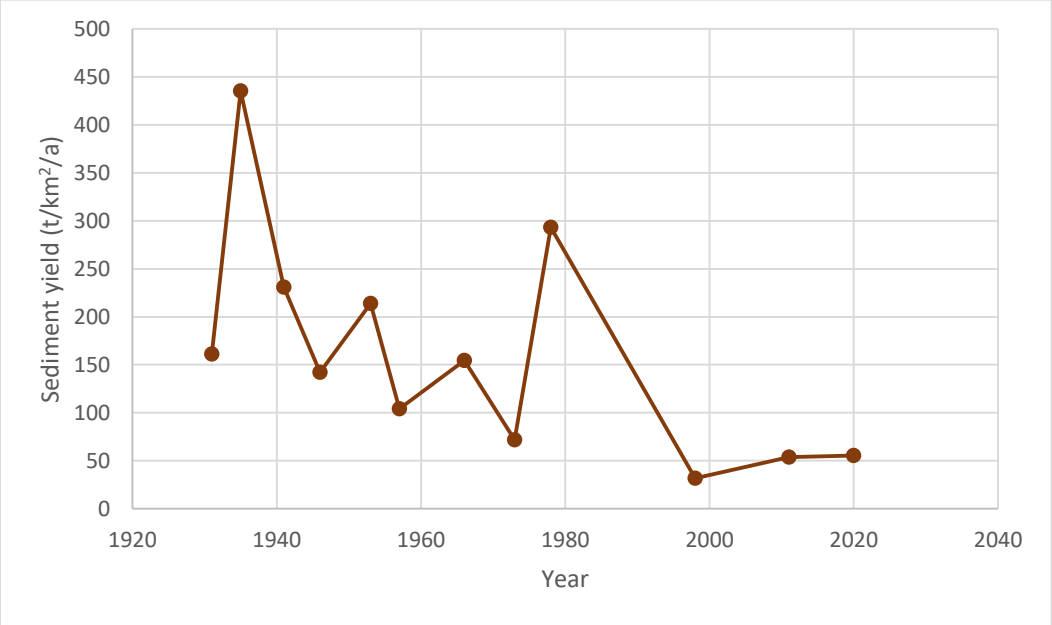

Figure 3.15: Estimated historical sediment yield for Nqweba catchment

Figure 3.16: Decline in sediment load observed in Orange River (Basson & Rooseboom, 1997)

Table 3.13: Sediment yields for different locations in South Africa (Msadala *et al.*, 2010)

Name	Station No	Sediment yield (t/km^2/a)
Nqweba Dam	N1R001	56
Kromellenboog Dam	A3R003	120
Klipkoppie Dam	X2R002	219
Middle Letaba	B8R007	520
Witklip Dam	X2R003	402
Goedertrouw Dam	W1R001	524
Oranjerivierbrug		630
Caledon rivier (Slabbertswag)	D2H016	832
Bridle Drift Dam	R2R003	1509
Gubu Dam	S6R001	840

4 SHETRAN Model Application

In order to execute a SHETRAN simulation, the following data is essential:

- Relevant DEM for the study area;
- Land cover distribution;
- Soil properties,grading and spatial distribution;
- Historical rainfall and potential evaporation records; and
- Streamflow and sediment yield data for calibration.

All of the above are described in Section 3.2 and 3.3. The DEM, Land cover – and soil distribution maps were converted to ASCII files, consisting of 1911 grid squares of 1.65 km by 1.65 km each. The time step was set to 24 hours to correspond with the available daily rainfall and – evaporation input data. The initial water table depth below ground was set to 3 m, but to increase the accuracy of the simulations, the results of the phreatic surface level for preceding simulations (after equilibrium was reached) were used to represent the initial conditions for the Variably Saturated Subsurface (VSS) module, as described in Section 2.5.1.3.

4.1 SHETRAN Model calibration

In theory, the parameters used in a physically-based, spatially-distributed model, like SHETRAN, should not have to be calibrated. The parameters are supposed to be based on physical measurements and give an accurate representation of the characteristics of the part of the catchment for which they are evaluated. However, it is impossible or impractical to measure all the model parameters in all the grid squares for the whole catchment. This means that multiple parameter values have to be estimated by using data from a courser resolution. For example, only twelve soil samples were taken to represent the soil characteristics across the entire catchment. In other cases, parameter values have to be obtained from literature. Therefore, a degree of calibration or parameter adjustment will always be required to correlate the observed and simulated data. However, this calibration should be restricted and controlled by physical plausibility (Ewen & Parkin, 1996).

4.1.1 Water-flow calibration and parameter verification

The period from 2010 to 2020 was used with a 24 hour time step, to calibrate the simulated streamflow against the observed inflow into the Nqweba Reservoir. The 2010 to 2020 period was

chosen because it best represents current catchment conditions, and the most reliable data with regards to catchment characteristics (land cover and soil properties) were available for this period.

Typical model parameters or functions to which SHETRAN water-flow simulations are most sensitive include the following:

- Saturated hydraulic conductivity, K_s
- Overland flow resistance coefficient (Stickler or $^{1}/_{\text{Manning n}}$)
- Soil hydraulic property curves (Van Genuchhten α and n parameters)
- Relationship between actual- and potential evaporation ($^{E_a}/_{E_p}$).

Standard parameter values for typical soil types and vegetation cover are given in Table A-2, and Table A-3 in **Appendix A** and Table B-1 and Table B-2 in **Appendix B**. The standard parameters were used as starting values for calibration. The different soil characteristics for the Nqweba Dam catchment were described in Section 3.2.3.1 and can be divided into four soil types. The suggested and adopted values for the soil properties used in the model are given in Table 4.1. The land cover distribution for the Nqweba catchment was described in Section 3.2.2 and comprise of three main vegetation types. Table 4.2 illustrates the adopted standard vegetation types used in the SHETRAN simulations and the suggested and adopted sensitive vegetation properties adjusted for calibration. The other vegetation properties were used as described in the SHETRAN manual and illustrated in Table 4.3.

Table 4.1: Suggested and adopted sensitive soil properties used in SHETRAN water flow calibration

Soil Type	Ks (m/day)		VanG α (cm^{-1})		VanG n	
	Suggested	Adopted	Suggested	Adopted	Suggested	Adopted
Loamy Sand	5.04	5.2	0.01986	0.0195	1.793	1.35
Sandy Loam	0.62	3.8	0.01441	0.0125	1.736	1.25
Clay loam	0.055	1.6	0.00923	0.0078	1.657	1.125
Clay Loam (with gravel)	0.055	2.2	0.00923	0.0078	1.657	1.125

Table 4.2: Suggested and adopted sensitive vegetation properties used in SHETRAN calibration

Vegetation type	Adopted SHETRUN vegetation type	Ea/Ep		1/Manning n	
		Suggested	Adopted	Suggested	Adopted
Camdeboo Escarpment Thicket	Evergreen Forest	1	1	0.5	7
Upper Karoo Hardeveld	Shrub	0.4	0.4	1	30
Karoo Grassland	Grass	0.6	0.6	1	25

Table 4.3: Standard vegetation properties according to SHETRAN manual(Ewen *et al.*, 2011)

Vegetation Type	Canopy storage capacity (mm)	Leaf Area Index	Maximum Rooting depth (m)
Evergreen Forest	5	1	2
Shrub	1.5	1	1
Gras	1.5	1	1

To relate specific rainfall events with flood peaks, the results are given for a daily time step and are illustrated in Figure E-1 to Figure E-4 in **Appendix E**. For illustration and discussion, the results for the simulated monthly discharge (accumulated 24-hour discharge) against the observed monthly inflow into the Nqweba Reservoir for the period of 2010 to 2020 is given in Figure 4.1. In order to verify the calibration parameters, simulations were also performed for preceding decades and are illustrated in Figure 4.2, Figure 4.3, and Figure 4.4.

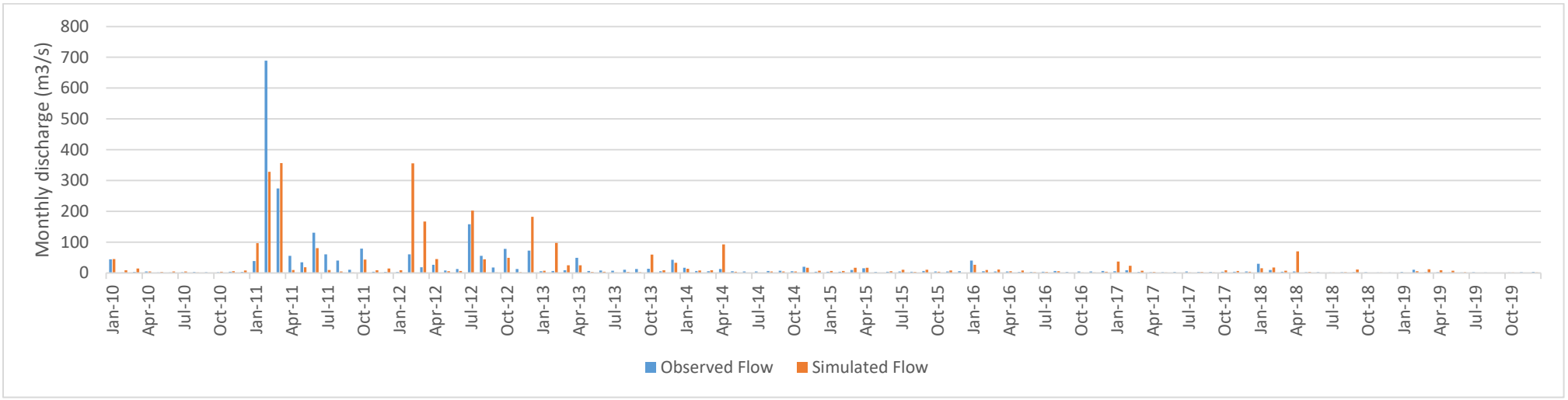

Figure 4.1: Simulated monthly flow against observed flow into Nqweba Reservoir for 2010-2020 period

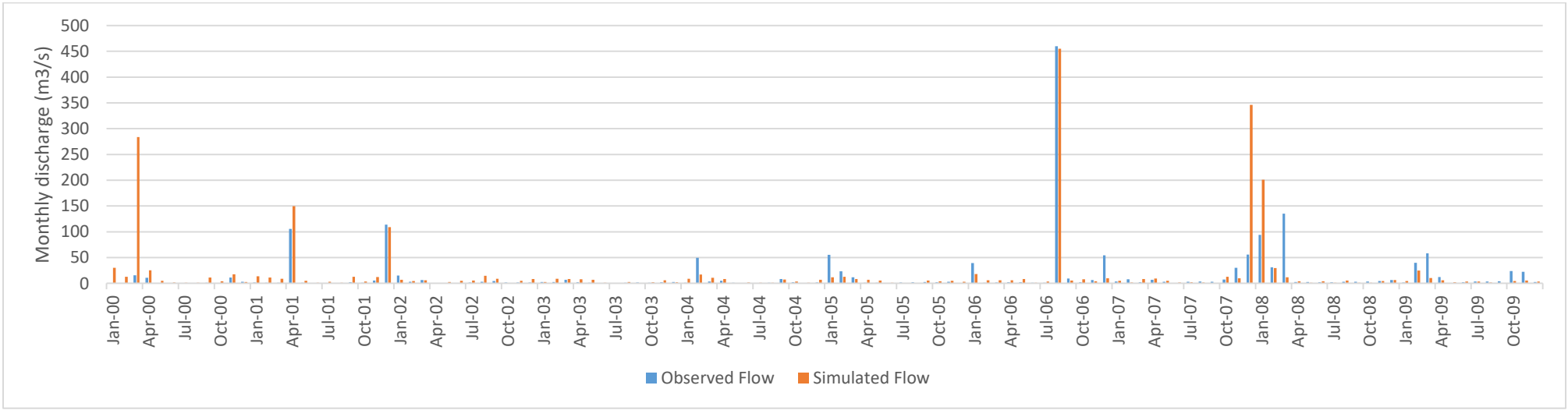

Figure 4.2: Simulated monthly flow against observed flow into Nqweba Reservoir for 2000-2010 period

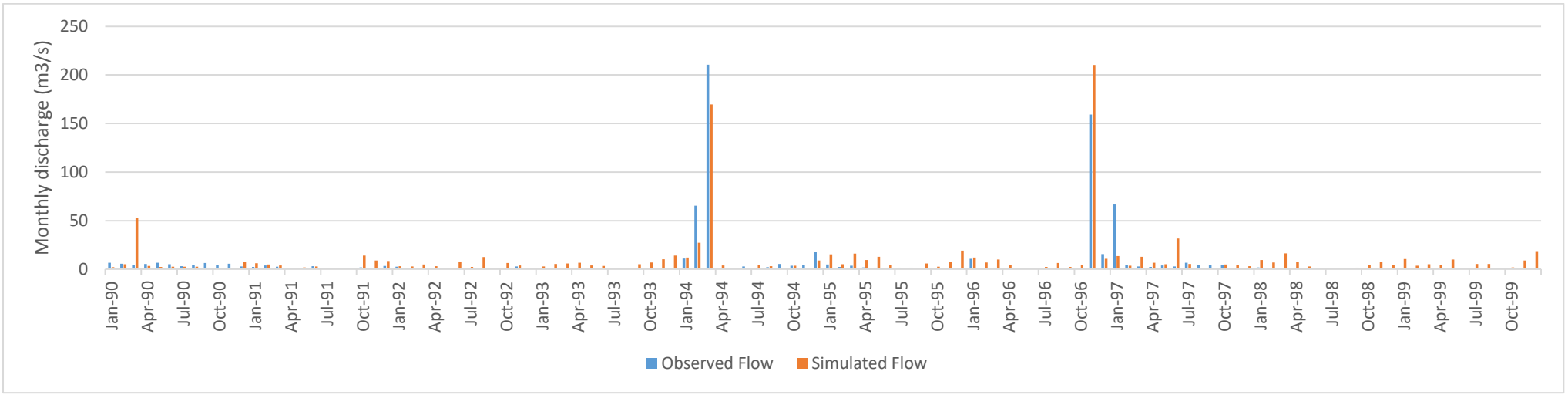

Figure 4.3: Simulated monthly flow against observed flow into Nqweba Reservoir for 1990-2000 period

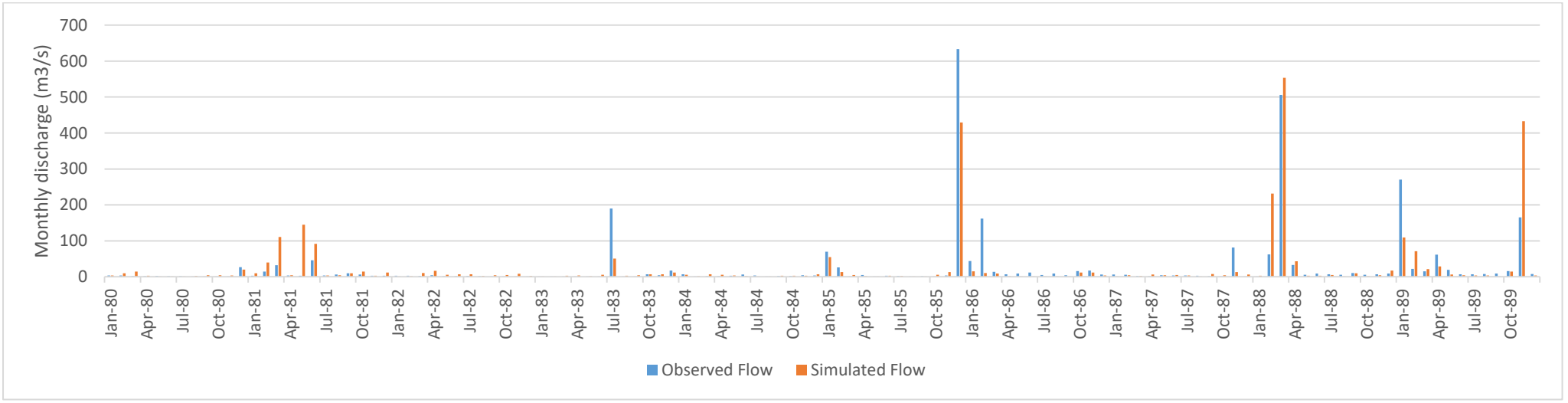

Figure 4.4: Simulated monthly flow against observed flow into Nqweba Reservoir for 1980-1990 period

4.1.1.1 Discussion of water flow calibration and parameter verification results

While analysing the calibration and verification results, it is essential to note that it is highly probable that the catchment characteristics and catchment response for different decades (or even years) might fluctuate significantly. For example, intermittent droughts can cause a degradation of vegetation cover for some periods, resulting in different runoff events for approximately the same rainfall event. However, to verify the SHETRUN model, the same vegetation cover was used for the calibration and verification periods. Table 4.4 summarize the average rainfall for the Nqweba Dam catchment and illustrates the difference between the observed cumulative discharge and the cumulative simulated discharge for the calibration period (2010-2020) and verification periods (1980-2010).

Table 4.4: Average rainfall, observed- and simulated discharge for Nqweba Dam Catchment

Period	Average rainfall (mm)	Approx MAP(mm)	Observed Cumulative discharge (m^3/s)	Simulated Cumulative Discharge (m^3/s)	% error
2010-2020	3565	356	2595	3023	16
2000-2010	3615	362	1747	2262	30
1990-2000	2952	295	769	1098	43
1980-1990	3396	340	2899	2962	2

From Table 4.4, it can be seen that an error of 16 % exists between the observed and simulated flow for the calibration period. Because of uncertainty in available rainfall- and observed streamflow data, as well as complex catchment dynamics, the error of 16 % was accepted. The 1980-1990 period only gives a 2 % difference between observed and simulated flow and therefore verifies the calibration parameters.

For the 1990-2000 period, the error between observed and simulated flow is 43 %, which is quite large. Therefore, the error between the calibrated model and the 1990-2000 verification period is approximately 27 %. Table 4.4 illustrates that the rainfall for the 1990-2000 period is much less than the other periods. In Section 3.2.5, the catchment response with regards to flood events and rainfall was discussed. One of the conclusions was that a significant rainfall event after a dry period would result in significantly less runoff because empty farm dams might intercept a portion of the runoff. The presence of farm dams is not included in the model and can explain why the simulated flow exceeds the observed flow.

For the 2000-2010 period, the error between the observed and simulated flow is 30 %, resulting in a 14 % difference between the calibration and verification results. However, from Table 4.4 is evident that the observed flow (1747 m^3/s) for the 2000-2010 period is much lower than the observed flow (2595 m^3/s) for the calibration period, but the average rainfall is slightly higher. Therefore, if the rainfall data used in the simulation are considered, the simulated results are more realistic than the calculated flow. Due to the limited rainfall stations within the catchment, it is highly probable that some rainfall events are overestimated, while others might be underestimated.

4.1.1.2 Water flow calibration and verification summary

By analysing the calibration and verification results in conjunction with the rainfall data that was used, as well as considering the interception of runoff by farm dams and possible vegetation cover change, it can be concluded that the SHETRAN water flow component was calibrated reasonably accurate for the 2010-2020 period. Errors in the verification results can be attributed to variation in catchment dynamics and the impossibility to obtain the accurate spatial distribution of historical rainfall and catchment characteristic data for the whole catchment area.

4.1.2 Sediment yield calibration and parameter verification

The SHETRAN sediment transport component was described in Section 2.5.2. The standard SHETRAN sediment yield module was modified to represent the soil characteristics of the Nqweba Dam catchment. Based on the SHETRAN manual, seven grain size classes were used for calibration, and the values for the soil composition fractions were obtained from the soil grading described in Section 3.2.3.1. An iterative process was used to calibrate the cumulative sediment discharge for the 2010-2020 period against the calculated sediment load that entered the reservoir during the calibration period.

From the graph in Figure 3.14, the cumulative sediment volume that entered the Nqweba Reservoir by 2010 and 2020 was determined. Using the sediment density for the different periods, the cumulative sediment load that entered the reservoir and deposited was calculated and illustrated in Table 4.5. A total of 2.03 Mt sediment entered the Nqweba Reservoir during the 2010 to 2020 period. This is equal to an average sediment yield of 55.6 $t/km^2/a$ for the Nqweba catchment (3651 km^2).

Table 4.5: Cumulative Sediment load entering and deposited in Nqweba Reservoir (2010-2020)

Reservoir age (years)	Year	Density calibrated (kg/m3)	Cum Sed volume entering Nqweba Reservoir (Mm3)*	Cum Sediment load entering the reservoir and deposited (Mt)
85	2010	1204	34.3	41.3
95	2020	1215	35.7	43.3

An iterative process was used to calibrate the cumulative simulated sediment discharge against the cumulative calculated sediment load. The model parameters that were adjusted, as well as the adopted values, are given in Table 4.6. The default values proposed in the SHETRAN manual were used for the other parameters in the sediment yield module.

Table 4.6: Adjusted model parameters for sediment yield calibration

Model Parameter	Value	Unit
Raindrop and –drip soil erodibility coefficient	3	(J^{-1})
Overland flow soil erodibility coefficient	0.00008	($kg/m^2/s$)
Channel bank erodibility coefficient	0.00003	($kg/m^2/s$)

Figure 4.5 illustrates the simulated monthly sediment load entering the Nqweba Reservoir for the 2010-2020 calibration period. Table 4.7 illustrates the difference between the cumulative calculated and -simulated sediment load entering the reservoir.

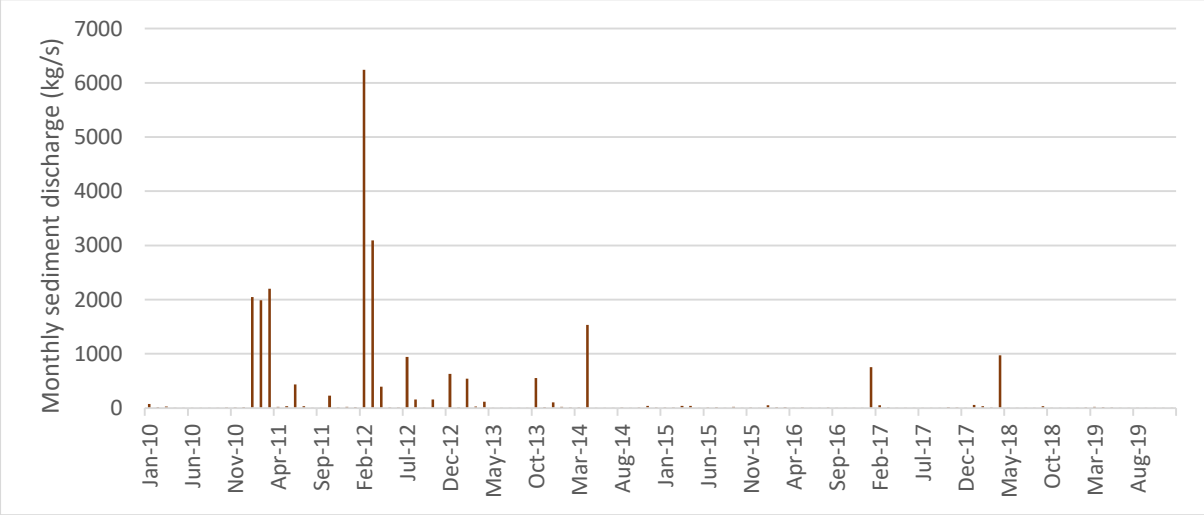

Figure 4.5: Simulated monthly sediment load entering the Nqweba Reservoir for the 2010-2020 period

Table 4.7: Difference between calculated and simulated sediment load entering Nqweba Reservoir for 2010-2020 calibration period

Period	Calculated sediment load entering the reservoir and deposited (Mt)	Simulated sediment load entering reservoir (Mt)	% error
2010-2020	2.03	2.10	3.4

The calibration parameters were verified using the 1978-1998 period. From the reservoir survey data given in Table 3.6, the sediment volume accumulated by 1978 and 1998 were obtained. Using the sediment densities, the cumulative sediment load that entered the reservoir and deposited by 1978 and 1998 were calculated and summarized in Table 4.8. A total of 2.32 Mt sediment entered the Nqweba Reservoir during the 1978 to 1998 period. This is equal to an average sediment yield of 31.8 t/km^2/a for the Nqweba Dam catchment (3651 km^2).

Table 4.8: Cumulative Sediment load entering and deposited in Nqweba Reservoir (1978 - 1998)

Reservoir age (years)	Year	Density calibrated (kg/m^3)	Cum Sed volume entering Nqweba Reservoir (Mm^3)	Cum Sediment load entering the reservoir and deposited (Mt)
53	1978	1152.8	31.3974	36.194
73	1998	1186.8	32.4541	38.5165

The SHETRAN model was applied for the 1978-1998 verification period, and the results for the simulated monthly sediment loads are illustrated in Figure 4.6. The difference between the cumulative calculated and -simulated sediment load entering the Nqweba Reservoir is given in Table 4.9.

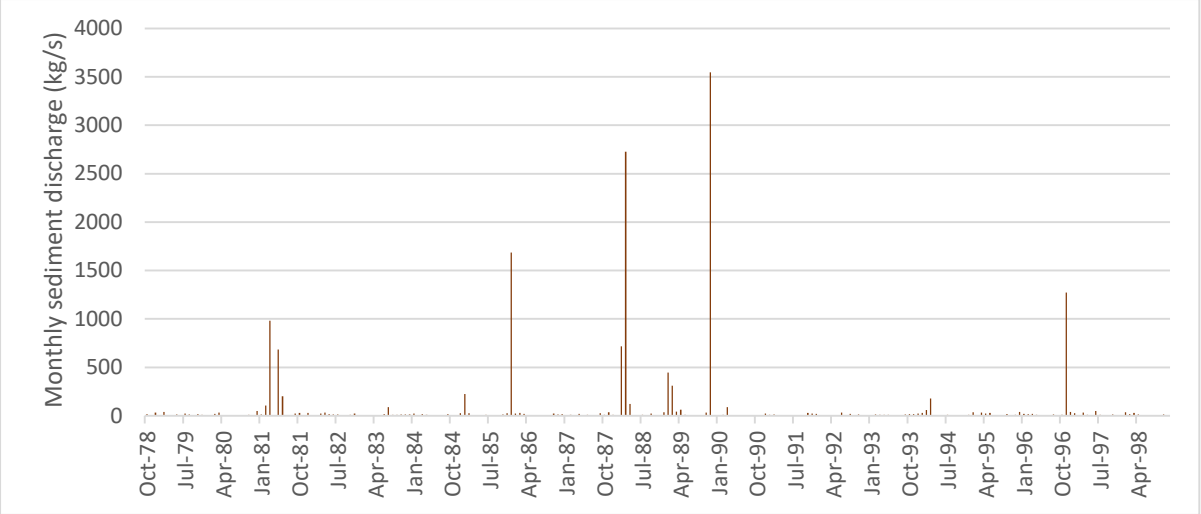

Figure 4.6: Simulated monthly sediment load entering the Nqweba Reservoir during 1978-1998 verification period

Table 4.9: Difference between calculated and simulated sediment load entering the reservoir during the 1978-1998 verification period

Period	Calculated sediment load entering the reservoir and deposited (Mt)	Simulated sediment load entering reservoir (Mt)	% error
1978-1998	2.32	1.70	26.7

4.1.2.1 Sediment yield calibration and parameter verification discussion

Table 4.7 illustrates that the total sediment load entering the reservoir during the 2010-2020 period was calibrated accurately, with an error of only 3.4 % between the calculated and simulated sediment load. When the verification results in Table 4.9 are considered, an error of 26.7 % is observed between the calculated and simulated sediment load entering the reservoir during the 1978-1998 period. Therefore, the simulation for the verification period underestimates the actual sediment load entering the reservoir. However, when looking at Figure 4.6, it is observed that the majority of sediment load for the verification period occur before 1990. From Table 4.4, it is evident that the simulated water flow for the 1980-1990 period is underestimated compared to the water flow calibration period of 2010-2020. Therefore, the underestimation of the sediment load is as expected.

4.1.2.2 Sediment yield calibration and parameter verification summary

It can be concluded that the SHETRAN model can be used to accurately calibrate the cumulative simulated sediment load against the observed sediment load (calculated from accumulated sediment volume obtained from reservoir survey data). The model parameters were verified, and a relatively

high error was observed. However, it can be concluded that the error is due to uncertainties in input data (rainfall distribution) and varying catchment dynamics (vegetation change), and not an inaccurate model. Unfortunately, sediment yield data for smaller time steps are not available, making it challenging to verify simulated sediment yield results for specific rainfall/storm events.

4.2 Identification of high sediment yield areas in Nqweba Dam catchment

The SHETRAN model can calculate the sediment yield at any river link in the catchment. In order to identify areas that generate the most sediment, the catchment was divided into 34 sub-catchments by identifying pour points in the rivers. The sub-catchments with pour points are illustrated in Figure 4.7. The sediment yield for the total contributing upstream area was determined (simulated) at each pour point and summarized in Table 4.10. The sub-catchment S2 generates the highest sediment yield, followed by sub-catchment S24. From the DEM in Section 3.2.1 (Figure 3.5), it is observed that these areas are characterised by relatively steep hillslopes. In Section 2.3.4.3, the significance and impact of topography (especially slope steepness) on erosion and sediment yield were discussed.

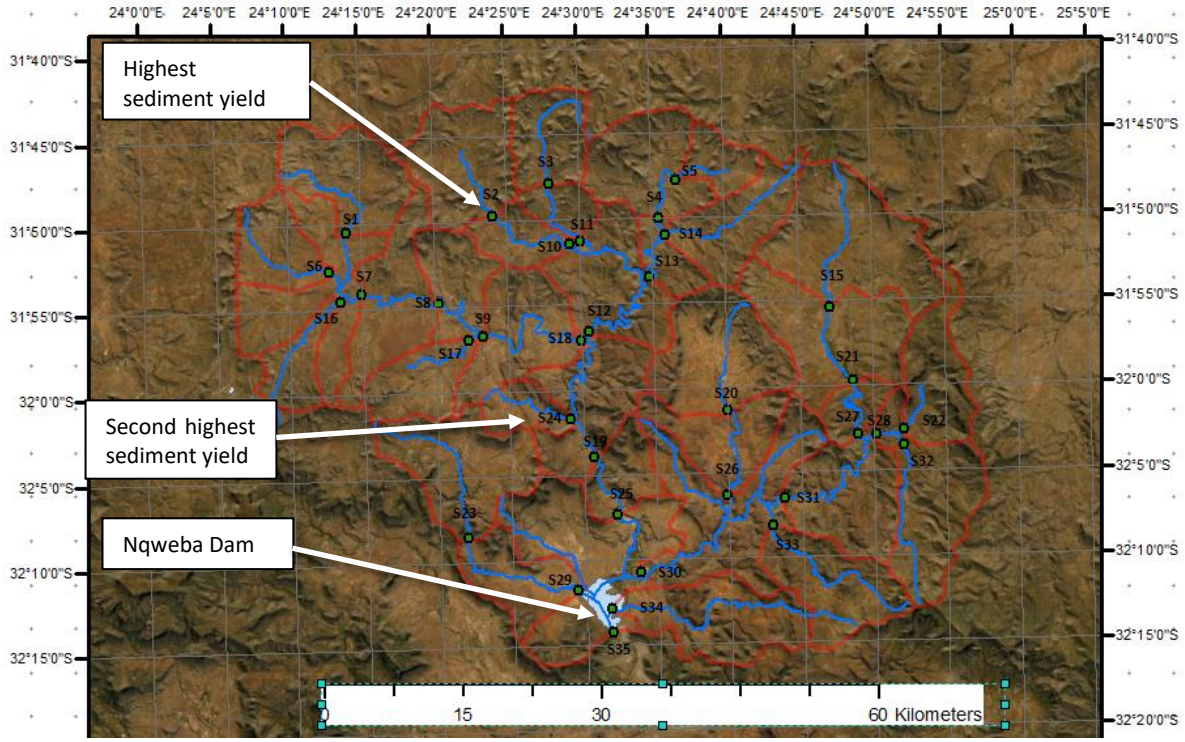

Figure 4.7: Nqweba Dam sub-catchments (red lines) with pour points

Table 4.10: Sediment yield at each pour point

Pour Point in Figure 4.7	Contributing Area (km^2)	Sediment yield ($t/km^2/a$)
S1	120	113
S2	131	611
S3	80	206
S4	161	69
S5	43	122
S6	74	15
S7	389	113
S8	513	111
S9	664	95
S10	181	170
S11	116	174
S12	693	112
S13	300	120
S14	102	132
S15	170	92
S16	54	319
S17	74	165
S18	786	46
S19	1647	116
S20	157	124
S21	333	79
S22	58	68
S23	152	161
S24	42	537
S25	1707	118
S26	1264	21
S27	248	140
S28	206	26
S29	225	305
S30	1264	82
S31	707	96
S32	131	204
S33	119	36
S34	133	32
S35*	3651	56

*At Nqweba Dam

4.3 SHETRAN Model parameter sensitivity and model uncertainty

During the water flow and sediment yield calibration, it was found that some model parameters are more sensitive than others. Table 4.11 illustrates the different model parameters that were adjusted to calibrate the water flow. The sensitivity is classified as a low, moderate, or high influence on the magnitude of the water flow, and consequently, the flood peaks of a preceding simulation. Table 4.11 also gives each parameter's range, as suggested for different vegetation and soil characteristics in the SHETRAN manual. It is suggested that the parameters with high sensitivity are used to calibrate the flood peaks and those with a low and moderate sensitivity for the base flow.

Table 4.11: Sensitivity and range of SHETRAN Model parameters and influence on water flow

Parameter	Sensitivity	Range	Influence on water flow if increased (+/-)
Canopy storage capacity	Low	0.5 – 3 (mm)	-
Leaf Area index	Low	1 - 5	-
Actual Evap/Potential Evap	High	0.4 – 0.7	-
Stickler overland flow coef.	Moderate	1 - 30	+
Saturated water content	Low	0.35 – 0.54	-
Residual water content	Low	0.07 – 0.326	+
Saturated conductivity	High	0.014 – 5 (m/day)	+
Van Genuchten α	Moderate	0.00458 - 0.02296 (cm^{-1})	-
Van Genuchten n	Moderate	1.443 - 2.071	-
Soil depth	High	0.1 – 10 (m)	-

Table 4.12 summarizes the sensitivity and range of the different model parameters that were adjusted to calibrate the sediment yield, as well as the influence on the simulated sediment yield. It is important to realise that the sediment yield is highly dependent on the water flow. Therefore, it is always suggested that the water flow is calibrated before any of these parameters are changed.

Table 4.12: Sensitivity and range of SHETRAN Model parameters and influence on sediment yield

Parameter	Sensitivity	Range	Influence on sediment yield if increased (+/-)
Raindrop and –drip soil erodibility coefficient	Low	0.1 – 82 (J^{-1})	+
Overland flow soil erodibility coefficient	Moderate	0.00005 – 0.0001 (kg/s)	+
Channel bank soil erodibility coefficient	High	0.00001 - 0.00003 (kg/s)	+

4.3.1 Model Uncertainty and Limitations

SHETRAN is a physically-based, spatially distributed hydrological and sediment yield model, and uses grids to represent the catchment area. The impossibility and impracticability to measure and obtain the actual physical parameters within the entire catchment, resulted in the use of effective parameter values, representative at the grid-scale. According to Bathurst (2011), the use of effective parameter values for grids may not allow an accurate reproduction of the observed response in all circumstances. For example, during simulations, the model rated soil hydraulic conductivity may increase beyond measured values when large grid squares are used for catchments with hilly terrain. As a result of parameter estimation, it is generally acknowledged that the parameterization of physically-based, spatially distributed models involves uncertainty. This uncertainty creates the potential for multiple parameterizations with possibly quite different but (apparently) equally acceptable combinations of parameter values (Bathurst, 2011).

In Section 3.2.4 and 3.2.5, the rainfall and streamflow data for the Nqweba Catchment were discussed, and the following limitations cause uncertainties when the simulated results are compared to the measured or calculated streamflow and sediment yield:

- The absence of complete rainfall data for the entire catchment results in significant rainfall events to be either under- or overestimated for parts of the catchment;
- The streamflow data used for calibration was calculated from a dam mass balance and is not actual streamflow measurements, which adds variables (water withdrawal, spillage, evaporation, and sedimentation), and increases uncertainty in the accuracy of streamflow data;
- The simulated sediment yield was calibrated against calculated sediment yield (from reservoir survey data) because actual stream measurements were not available;

- Limited availability of borehole log data causes uncertainties in subsoil parameterization data (soil type and depth), resulting in possible errors during simulations;
- Seasonal variability in vegetation and changes in vegetation caused by different land-use practices for different decades makes parameter verification and model validation difficult; and
- The model was calibrated for a single catchment in South Africa and is not validated for general application.

The implications of the uncertainties for model output is recognised, and errors in the output results are probably possible. Although the SHETRAN model was calibrated and the calibration parameters verified, caution should be exercised when the climate change simulation results are evaluated. The simulation results must be seen as crude approximations and not exact values, and it should be noted that computer simulations form only a small part of environmental planning and hydraulic design criteria.

5 Climate Change – SHETRAN model application

In Section 5, climate data obtained from the Climate Information Platform (CIP) (CSAG, 2020), which was developed by the Climate System Analysis Group and discussed in section 2.6.4.1, is used to determine climate change signals for different future periods. The climate change signals are applied to the current Nqweba Dam catchment's climate data (rainfall and evaporation) to represent possible future conditions. The modified climate data is applied to the SHETRAN model to investigate the possible future impacts of climate change on water flow and sediment yield.

The methodology used to determine and apply the climate change signals was adopted from Meddi *et al.* (2010) and is known as the Delta Change Approach. Three data sets are required, which includes observed climate data, as well as current and future climate data projected by climate models for the period under consideration.

5.1 Climate data and determination of climate change signals

The CIP offers projected climate data (1960-2100) for eleven climate models (Section 2.6.4.1) and two future emission scenarios (RCP 4.5 and RCP 8.5) for numerous locations in South Africa, which are marked in Figure 5.1. Four possible data points surround the Nqweba Dam catchment. Included are stations located at Beaufort West, Willowmore, Somerset East, and Middelburg. In order to determine which station's data is the most suitable for the Nqweba Dam catchment, the current climate of Graaff-Reinet was compared to each surrounding location. Looking at the average monthly high and low temperatures, average hourly temperatures, monthly cloud cover, daily chance of precipitation, and average monthly rainfall, it was determined that the climate at Somerset East is the closest related to that at Graaff-Reinet. The comparison between Graaff-Reinet's climate and Somerset East's climate is given in **Appendix F**.

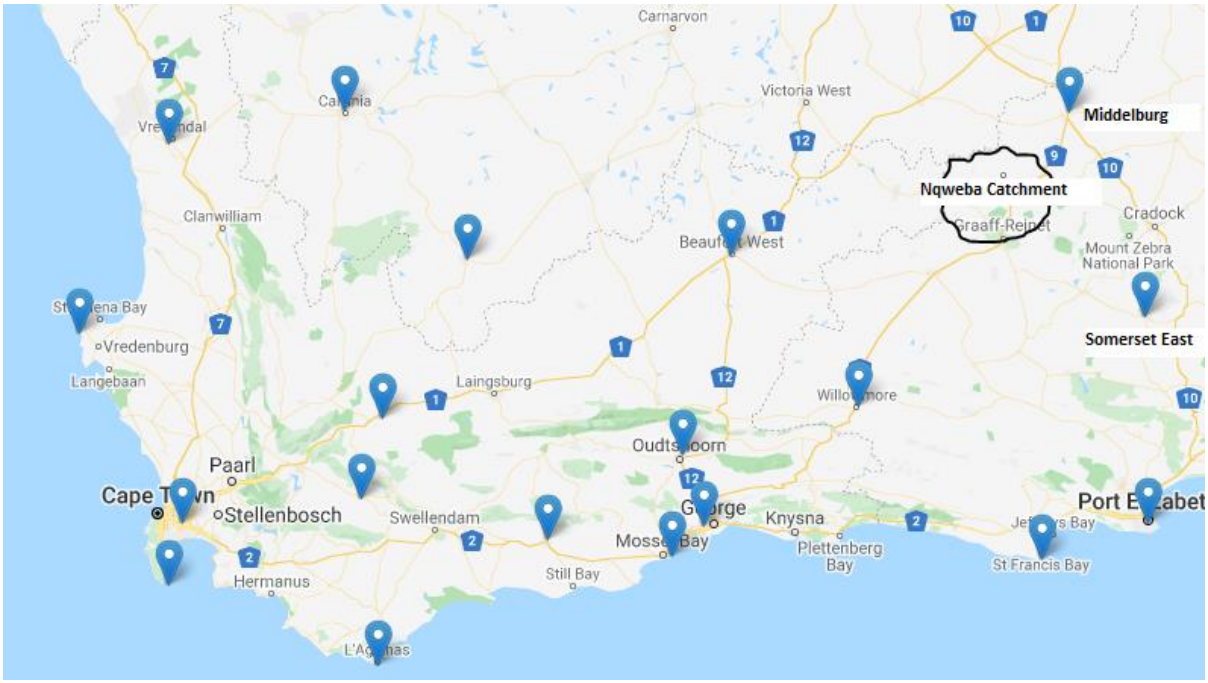

Figure 5.1: Location of Nqweba catchment and location points of available climate data (CSAG, 2020)

5.1.1 Determination of climate change signal for different future periods

Four future periods were chosen for the analysis to investigate the impact of climate change on water flow and sediment yield. Included are 2030-2040, 2050-2060, 2070-2080 and 2090-2100. The methodology used to determine the rainfall and evaporation signals from the CIP data is as follows: First, the monthly rainfall data for the SHETRAN calibration (baseline) period (2010-2020) projected by each climate model was listed. For example, Table 5.1 illustrates the monthly rainfall projected by each climate model for the first six months of 2010. The data in Table 5.1 is for the RCP 4.5 emission scenario. Next, the monthly rainfall for the same emission scenario projected by each climate model for the future period under consideration is listed. For example,

Table 5.2 illustrates the monthly rainfall projected by each climate model for the first six months of 2030. Next, the average monthly rainfall projected by the eleven climate models for the baseline period and the future period under consideration was determined. Finally, by dividing the projected average future rainfall by the projected average rainfall for the baseline period, the climate change signal for each month is calculated, as illustrated in Table 5.3. Meddi *et al.* (2010) propose that the average values for all eleven models are used to minimise the biased signals predicted by individual climate models for some months.

Table 5.1: Monthly Rainfall projected by each climate model for the first six months of 2010 baseline period (mm)

Date (YYYY-MM)	MIROC-ESM	CNRM-CM5	CanESM2	FGOALS-s2	BNU-ESM	MIROC5	GFDL-ESM2G	MIROC-ESM-CHEM	GFDL-ESM2M	MRI-CGCM3	bcc-csm1-1
2010-01	61	83	33	16	17	45	47	38	29	45	33
2010-02	37	43	65	232	79	36	110	54	83	36	62
2010-03	40	22	40	67	23	35	51	71	54	83	32
2010-04	54	47	62	189	64	77	103	113	90	46	148
2010-05	24	11	54	6	20	13	46	12	28	2	19
2010-06	19	100	1	8	10	11	11	37	3	86	1

Table 5.2: Monthly rainfall projected by each climate model for the first six months of 2030 (mm)

Date (YYYY-MM)	MIROC-ESM	CNRM-CM5	CanESM2	FGOALS-s2	BNU-ESM	MIROC5	GFDL-ESM2G	MIROC-ESM-CHEM	GFDL-ESM2M	MRI-CGCM3	bcc-csm1-1
2030-01	8	69	38	12	13	47	24	25	22	23	53
2030-02	40	41	19	36	17	41	38	39	19	35	39
2030-03	26	35	40	24	9	37	56	15	18	14	20
2030-04	31	69	14	15	8	27	23	110	27	95	29
2030-05	46	40	49	20	50	89	51	40	34	37	24
2030-06	43	22	28	32	33	68	42	44	13	22	12

Table 5.3: Determination of climate change rainfall signal for the first six months of 2030 (RCP 4.5)

Date (YYYY-MM)	Avg projected Rainfall (mm)		Date (YYYY-MM)	Avg projected Rainfall (mm)		Climate change signal
2010-01	41		2030-01	28		0.68
2010-02	78		2030-02	32		0.42
2010-03	49		2030-03	27		0.56
2010-04	84		2030-04	42		0.49
2010-05	22		2030-05	45		2.09
2010-06	26		2030-06	34		1.33

The methodology described above was used to determine the monthly rainfall signals for all the future periods under consideration, as well as for both emission scenarios (RCP 4.5 and RCP 8.5). By using projected temperature data from the CIP, the same methodology was used to determine the evaporation signals for the corresponding future periods by applying an approach suggested by Hughes (2007):

SHETRAN requires potential evaporation data to execute a simulation. The maximum and minimum (monthly average) projected temperature data for the baseline period and future period under consideration were used to determine the temperature component of the Hargreaves (Hargreaves & Allen, 2003) Equation (Eq. (5.1)). For Eq. (5.1), relative humidity and wind speed, which are also parameters included in the Hargreaves Equation, are ignored. This is done because it was assumed that the relative humidity and wind speed remains constant between the present and future scenarios under consideration.

$$\mathbf{HC} = \frac{(\mathbf{T_{max}} + \mathbf{T_{min}})}{\mathbf{2}} \cdot \sqrt{(\mathbf{T_{max}} + \mathbf{T_{min}})} \qquad (5.1)$$

Where:

- HC = The temperature component of the Hargreaves equation
- $\mathrm{T_{max}}$ = Average monthly maximum temperature
- $\mathrm{T_{min}}$ = Average monthly minimum temperature.

The same approach that was used to determine the climate change signals for the rainfall was applied to determine the climate change signals for the evaporation. However, instead of using the monthly rainfall, the calculated monthly HC was used. The data for determining the climate change evaporation signals for the first six months of the 2030-2040 period and emission scenario RCP 4.5 is given in **Appendix G**.

A summary of the average monthly rainfall and evaporation signals in relation to the 2010-2020 period predicted by each climate model for the RCP 4.5 emission scenario and the 2030-2040 period are illustrated in Figure 5.2 and Figure 5.3. The climate change signals for all the other periods under consideration, and both RCP 4.5 and RCP 8.5 emission scenarios are given in **Appendix H**. Table 5.4 summarizes the average climate change signals for the whole period under consideration. It is important to note that, for illustration purposes, only the average climate change signals for the whole period under consideration is given. However, for the SHETRAN simulations, each month's signal (as illustrated in Table 5.3) was applied to the climate data.

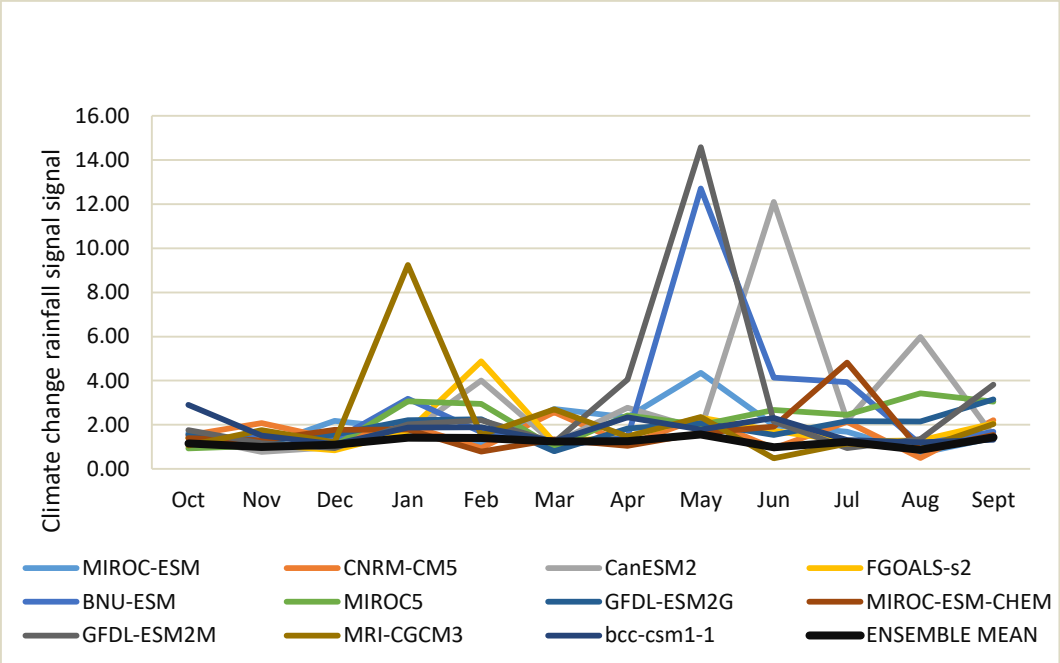

Figure 5.2: Average monthly climate change rainfall signals predicted by climate models for 2030-2040 in relation to 2010-2020 (RCP 4.5)

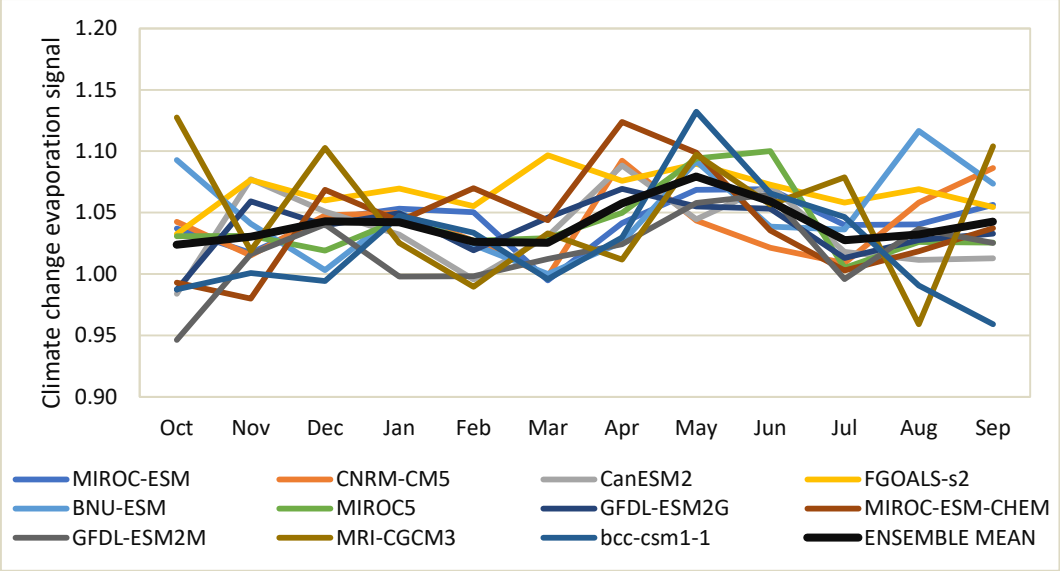

Figure 5.3: Average monthly climate change evaporation signals predicted by climate models for 2030-2040 in relation to 2010-2020 (RCP 4.5)

Table 5.4: Average climate change signals for different future periods in relation to the 2010-2020 climate

Period	Average Rainfall signal		Average Evaporation signal	
	RCP 4.5	RCP 8.5	RCP 4.5	RCP 8.5
2010-2020	1.00	1.00	1.00	1.00
2030-2040	1.22	1.17	1.04	1.05
2050-2060	1.11	1.12	1.05	1.09
2070-2080	1.13	1.19	1.08	1.15
2090-2100	1.24	1.29	1.09	1.21

From the results in Table 5.4, it is evident that an increase in average rainfall and evaporation for all future periods in relation to the 2010-2020 period is predicted. A steady increase in evaporation is predicted for both emission scenarios. Figure 5.3 illustrates that monthly evaporation signals will vary between 0.95 and 1.13. According to the climate models, a linear increase in average rainfall is not predicted. The highest increase in average rainfall is predicted for 2090-2100 and 2030-2040. Figure 5.2 illustrates that some models predict extremely high values (between 8 and 14.6) for some monthly rainfall signals. In order to prevent unrealistic rainfall data when the signals are applied to the current rainfall data, it was suggested that the average signals (for all eleven models) be used.

5.2 SHETRAN water flow and sediment yield climate change simulations (constant vegetation)

The climate change signals were applied to the rainfall and evaporation data that were used to calibrate the SHETRAN model for the 2010 to 2020 period. Although the climate models predicted an increase in average rainfall, which may result in the improvement of the vegetation cover, for this section, the SHETRAN model was used as calibrated and described in Section 4.1. All physical catchment parameters remained constant, and only the climate data were adapted. Figure 5.4 to Figure 5.7 illustrate the results for the calibrated sediment yield simulations of the baseline period (2010-2020) against the predicted sediment yield for different future periods. Similar graphs illustrating the impact on the water flow component are given in **Appendix I**. Table 5.5 summarizes the predicted future impacts of climate change on water flow and sediment yield for the Nqweba Dam catchment without considering land-use and vegetation change.

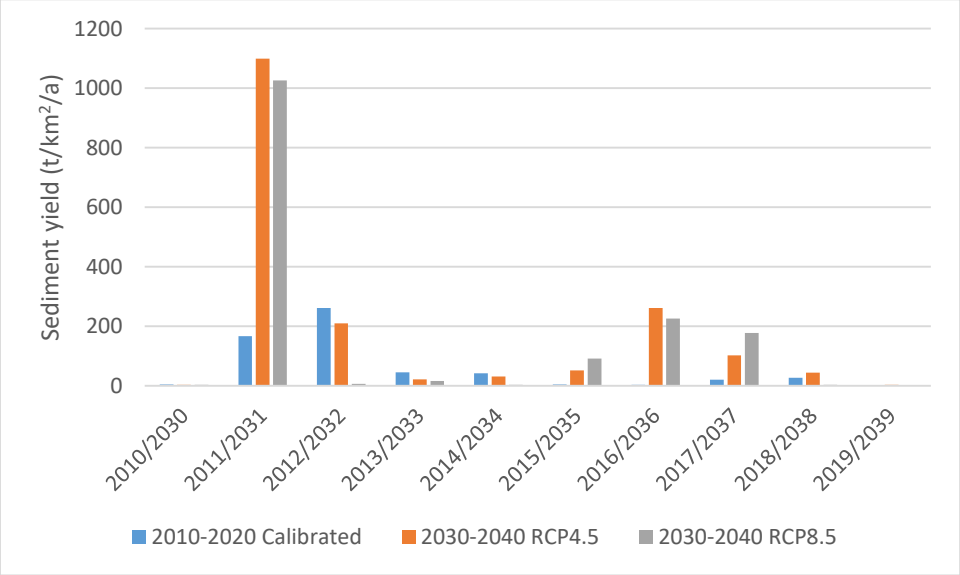

Figure 5.4: Calibrated sediment yield against possible future (2030-2040) sediment yield predicted for emission scenarios RCP 4.5 and RCP 8.5 and constant vegetation

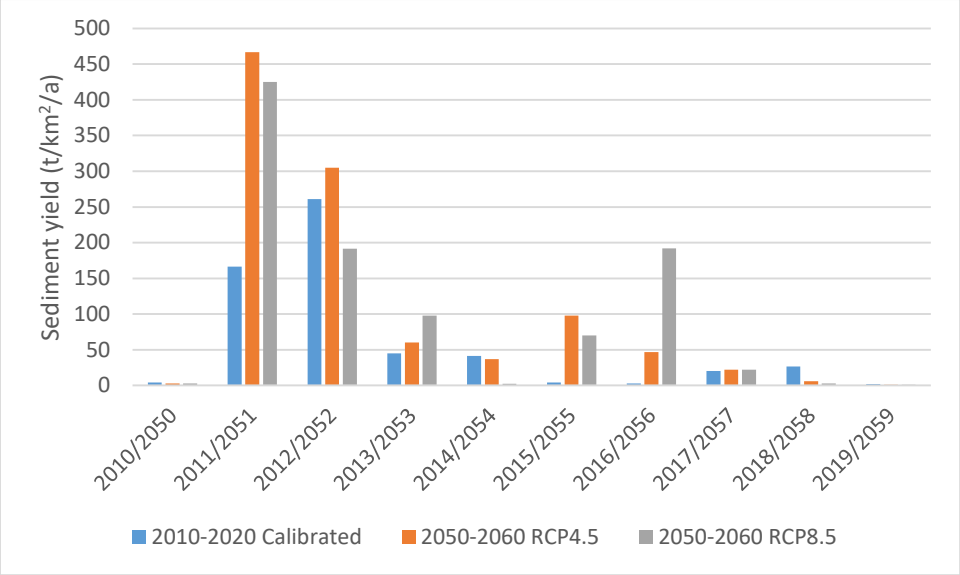

Figure 5.5: Calibrated sediment yield against possible future (2050-2060) sediment yield predicted for emission scenarios RCP 4.5 and RCP 8.5 and constant vegetation

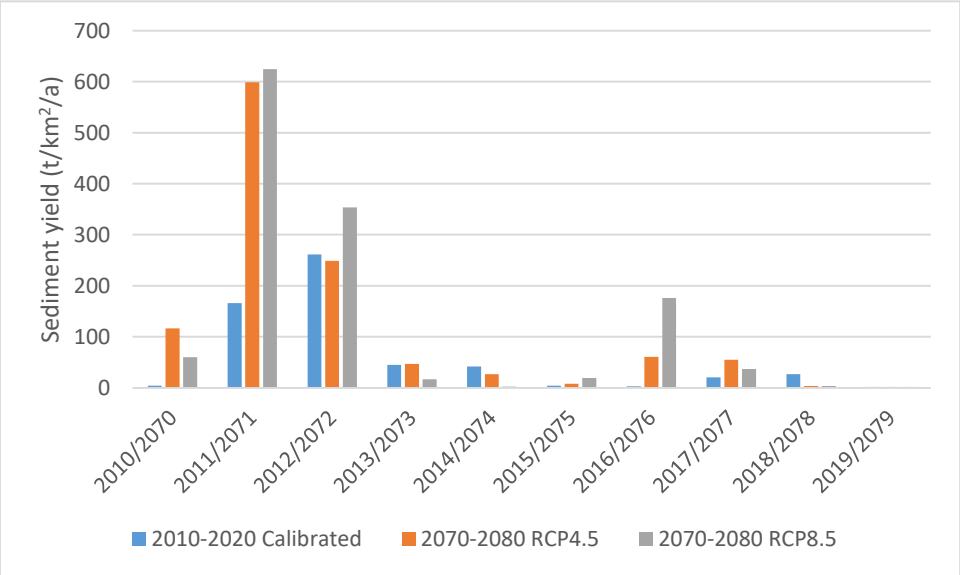

Figure 5.6: Calibrated sediment yield against possible future (2070-2080) sediment yield predicted for emission scenarios RCP 4.5 and RCP 8.5 and constant vegetation

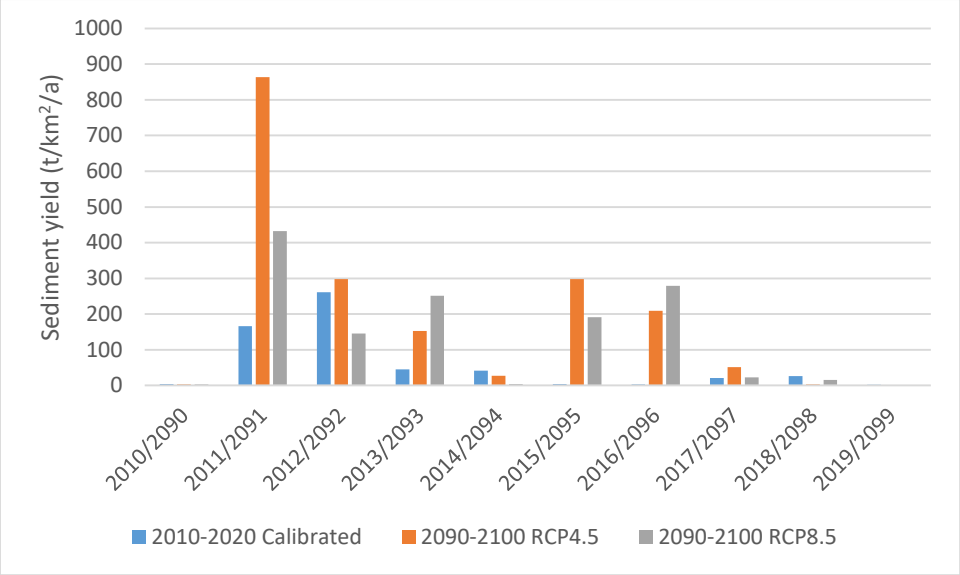

Figure 5.7: Calibrated sediment yield against possible future (2090-2100) sediment yield predicted for emission scenarios RCP 4.5 and RCP 8.5 and constant vegetation

Table 5.5: Predicted future impacts of climate change in relation to 2010-2020 on water flow and sediment yield for Nqweba Dam catchment

Period	Cumulative Water Flow (m^3/s)		Sediment yield ($t/km^2/a$)	
	RCP 4.5	RCP 8.5	RCP 4.5	RCP 8.5
2010-2020	3023	3023	60	60
2030-2040	19178	14110	191	162
2050-2060	9994	6849	109	105
2070-2080	8061	10997	122	135
2090-2100	15761	12731	199	140

From Table 5.5, it is evident that the cumulative water flow for each future period will be much higher than the 2010-2020 baseline period (due to the increased rainfall), with the highest increase during the 2030-2040 and 2090-2100 periods. Consequently, an increase in sediment yield is also observed with future values varying between 105 $t/km^2/a$ during the 2050s and 199 $t/km^2/a$ by the end of the century.

5.3 SHETRAN water flow and sediment yield climate change simulations (vegetation change)

According to the average climate change signals, calculated in Section 5.1, the Nqweba Dam catchment's average rainfall will increase in the future. An increase in average rainfall might increase

plant growth and improved vegetation cover. In Section 2.3.4.4, the influences of vegetation on (the mitigation of) soil erosion and sediment yield were discussed. Therefore, in this section, the impact of climate change and possible land cover change will be evaluated.

5.3.1 Quantifying the relationship between vegetation and rainfall for the Nqweba Catchment

In Section 2.2.5 the relationship between rainfall and vegetation greenness (the NDVI) for a study in the West African Sahel was discussed. Like the Nqweba Dam catchment, the West African Sahel is classified as a semi-arid region, with similar vegetation ranging from herbaceous types (short grass) and woody shrubs to thorny trees. The climate is characterised by long, dry winters and wet summers, which also resembles the Nqweba Dam catchment. The area (Wst African Sahel) has been affected by a severe drought during the late 1960s through the 1980s, causing land degradation and desertification. However, by analysing satellite data, it has been found that large areas of the region showed an increase in greenness since the 1980s.

In order to obtain possible vegetation change signals for the Nqweba Dam catchment, it was assumed that a linear relationship exists between the cumulative rainfall and the NDVI. Boundary values of 0.2 for current land cover conditions and 0.6 for future (end of the century) land cover were chosen. It is important to note that these values do not necessarily express the vegetation's actual condition for the different periods but are used to illustrate the possible change (improvement) that may occur. Figure 5.8 illustrates the linear regression between the cumulative rainfall and NDVI for the Nqweba Dam catchment. The equation on the graph was used to determine the NDVI for each period, and the vegetation change signal was calculated for both RCP 4.5 and RCP 8.5 emission scenarios and summarized in Table 5.6.

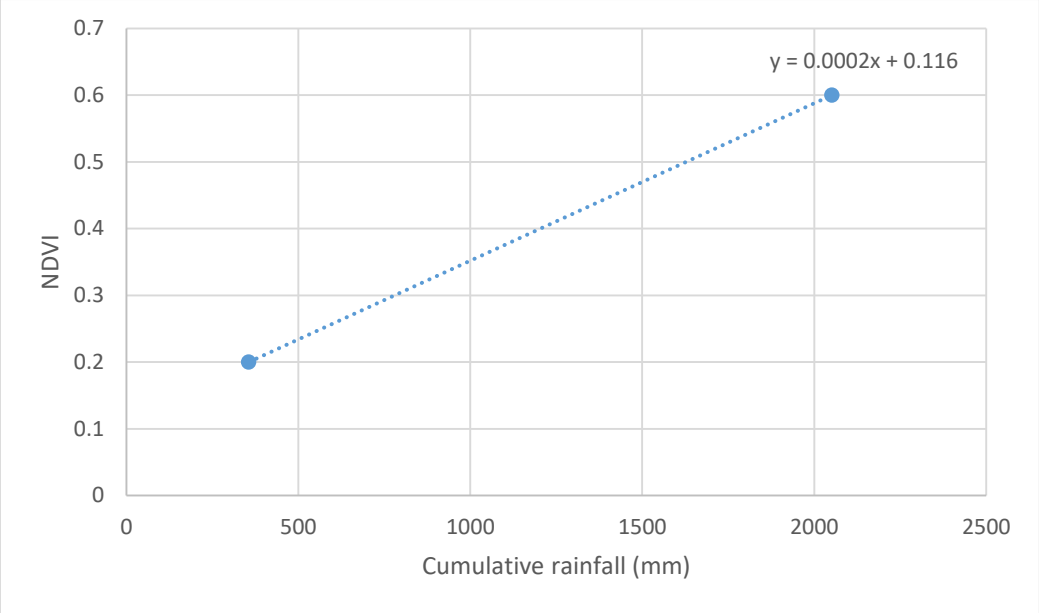

Figure 5.8: Linear regression between rainfall and NDVI for Nqweba catchment

Table 5.6: Determination of NDVI and vegetation change signals for future periods

Year	Cum Rainfall (mm)		NDVI		Vegetation signal	
	RCP 4.5	RCP 8.5	RCP 4.5	RCP 8.5	RCP 4.5	RCP 8.5
2020	356	356	0.20	0.20	1.00	1.00
2040	790	772	0.27	0.27	1.37	1.35
2060	1185	1170	0.35	0.35	1.77	1.75
2080	1587	1593	0.43	0.44	2.17	2.17
2100	2028	2052	0.54	0.60	2.70	3.00

5.3.2 Climate change with vegetation change - SHETRAN simulations

The vegetation signals were applied to the following vegetation properties that were described in Section 4.1.1:

- Stickler overland flow coefficient;
- Canopy storage capacity; and
- Leaf Area Index.

The other vegetation properties were kept constant, and the SHETRAN simulations for climate change with land cover change were executed. Figure 5.9 to Figure 5.12 illustrate the calibrated sediment yield against the possible future sediment yield for emission scenarios RCP 4.5 and RCP 8.5 and an improved vegetation cover. Table 5.7 illustrates a summary of the simulated impacts of climate change and vegetation change on the water flow and sediment yield for the Nqweba Dam catchment.

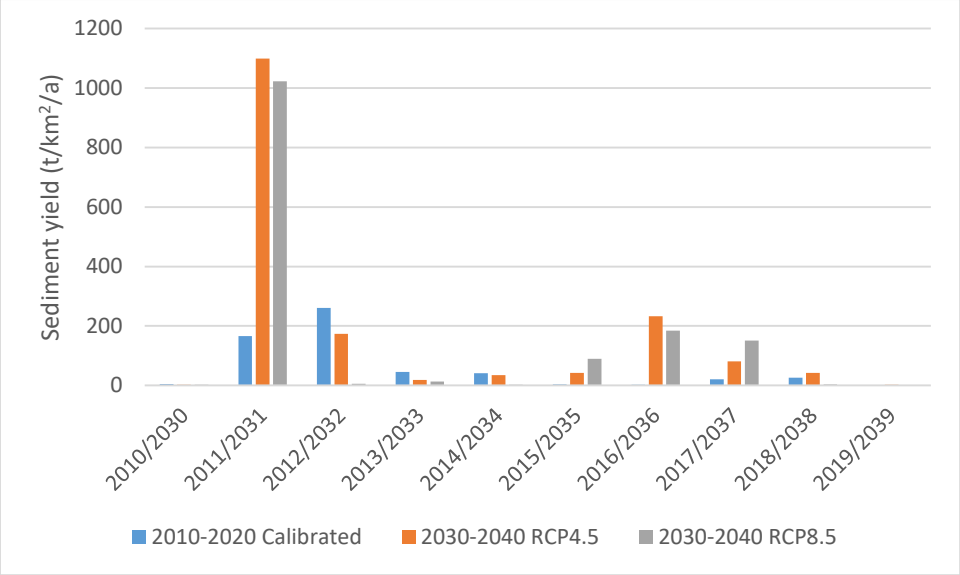

Figure 5.9: Calibrated sediment yield against possible future (2030-2040) sediment yield predicted for emission scenarios RCP 4.5 and RCP 8.5 and improved vegetation

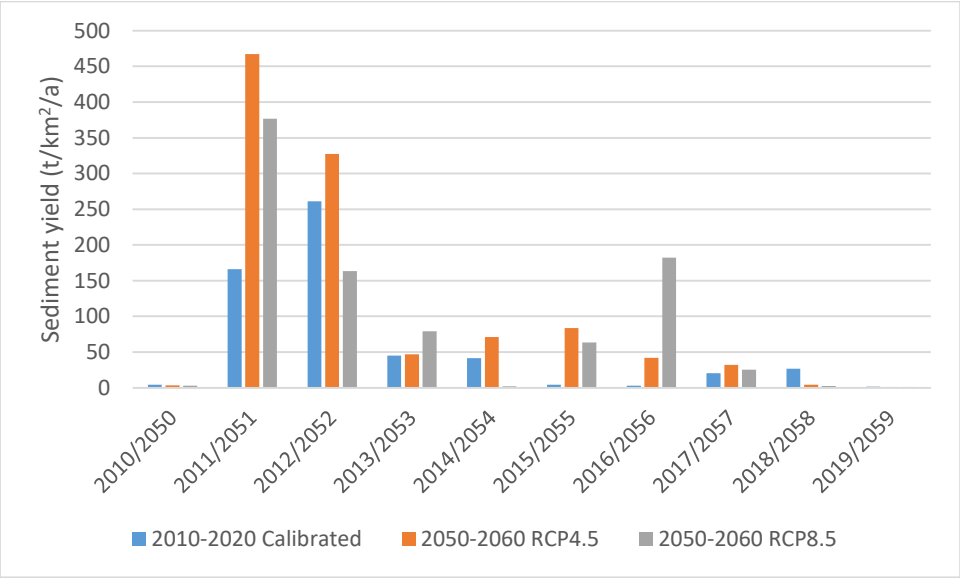

Figure 5.10: Calibrated sediment yield against possible future (2050-2060) sediment yield predicted for emission scenarios RCP 4.5 and RCP 8.5 and improved vegetation

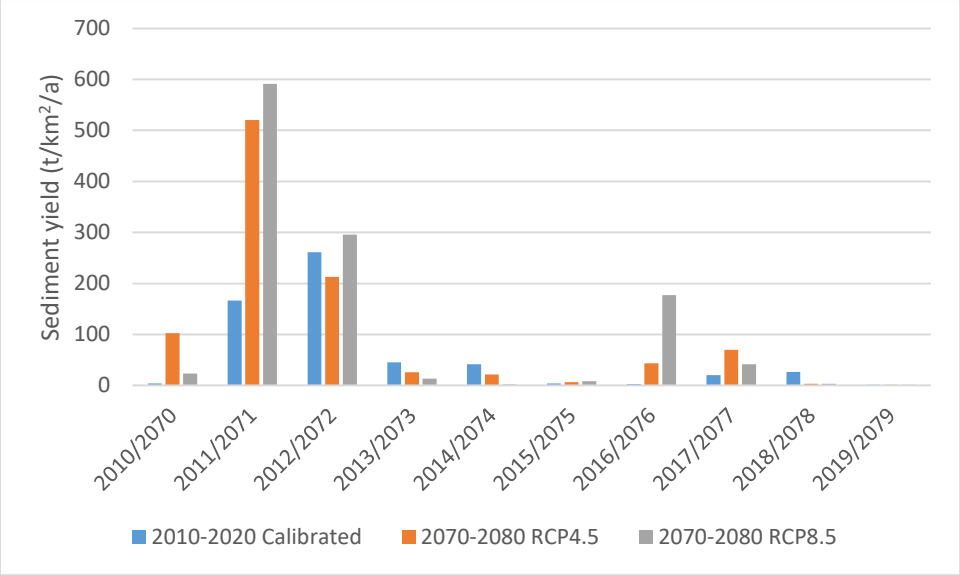

Figure 5.11: Calibrated sediment yield against possible future (2070-2080) sediment yield predicted for emission scenarios RCP 4.5 and RCP 8.5 and improved vegetation

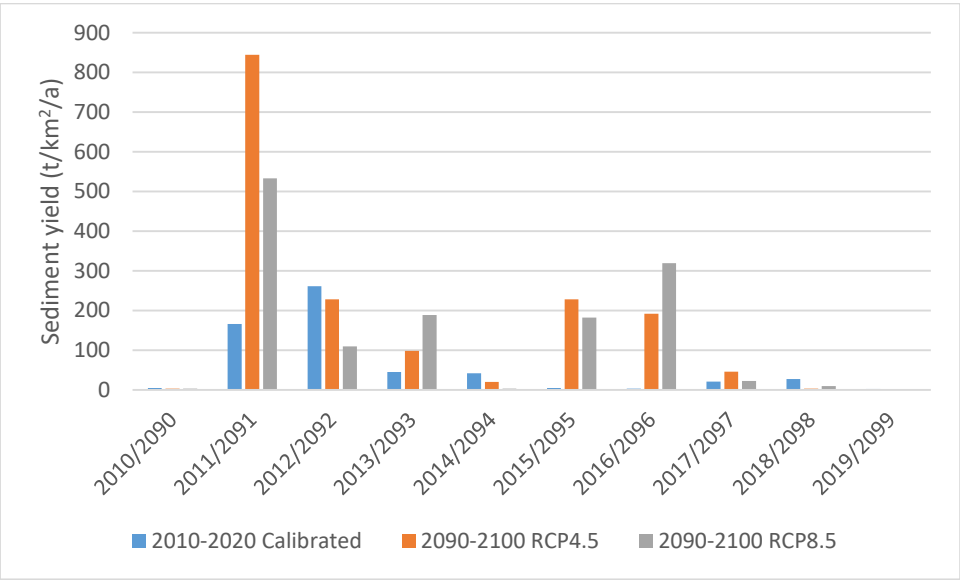

Figure 5.12: Calibrated sediment yield against possible future (2090-2100) sediment yield predicted for emission scenarios RCP 4.5 and RCP 8.5 and improved vegetation

Table 5.7: Predicted future impacts of climate change and improved vegetation cover in relation to 2010-2020 on water flow and sediment yield for Nqweba Dam catchment

Year	Cum Water Flow (m^3/s)		Average Sediment yield (t/km2/a)	
	RCP 4.5	RCP 8.5	RCP 4.5	RCP 8.5
2010-2020	3023	3023	60	60
2030-2040	18441	13608	182	155
2050-2060	9154	6016	101	94
2070-2080	6921	9636	106	121
2090-2100	14066	11015	174	133

Comparing the results in Table 5.7 and Table 5.5, it shows that the simulated water flow and sediment yield for the catchment will decrease if the vegetation cover improves. However, an increase in sediment yield of up to approximately 200 % is still predicted for the RCP 4.5 emission scenario and the 2030-2040 period.

5.4 Discussion of results

In summary, four possible future scenarios were simulated with the SHETRAN model:

1. Climate change with RCP 4.5 emission scenario and vegetation cover remaining as calibrated for the 2010-2020 period.
2. Climate change with RCP 4.5 emission scenario and vegetation cover changing with time and increased average precipitation.
3. Climate change with RCP 8.5 emission scenario and vegetation cover remaining as calibrated for the 2010-2020 period.
4. Climate change with RCP 8.5 emission scenario and vegetation cover changing with time and increased average precipitation.

Therefore, four possible outcomes were determined for each simulated period, as illustrated in Table 5.5 and Table 5.7. Table 5.8 summarizes the minimum and maximum (of the four possible outcomes) cumulative water flow and minimum and maximum average sediment yield for each period as simulated with the SHETRAN model. Table 5.9 illustrates the percentage increase in sediment for the different future periods under consideration in relation to the 2010-2020 baseline period.

Table 5.8: Minimum and maximum cumulative water flow and average sediment yield simulation results due to climate – and vegetation change for future periods

Period	Cumulative Water Flow (m^3/s)		Average Sediment yield ($t/km^2/a$)	
	Min	Max	Min	Max
2010-2020	3023	3023	60	60
2030-2040	13608	19178	155	191
2050-2060	6016	9994	94	109
2070-2080	9636	10997	106	135
2090-2100	11015	15761	133	199

Table 5.9: Increase in sediment yield for different future periods in relation to the 2010-2020 baseline period

Period	Increase in sediment yield (%)	
	Min	Max
2030-2040	158	218
2050-2060	57	82
2070-2080	77	125
2090-2100	122	232

From the results in Table 5.9 it can be seen that climate change may cause an increase in sediment yield (in relation to the 2010-2020 baseline period) of up to 232 % by the end of the century. However, it is possible that an increase of only 122 % by the end of the century is possible. The difference is due to the possibility of improved vegetation and a less harmful emission scenario (RCP 4.5). Figure 5.13 illustrates the historical sediment yields for the Nqweba Dam catchment, as calculated in Section 3.3, as well as the possible future sediment yields.

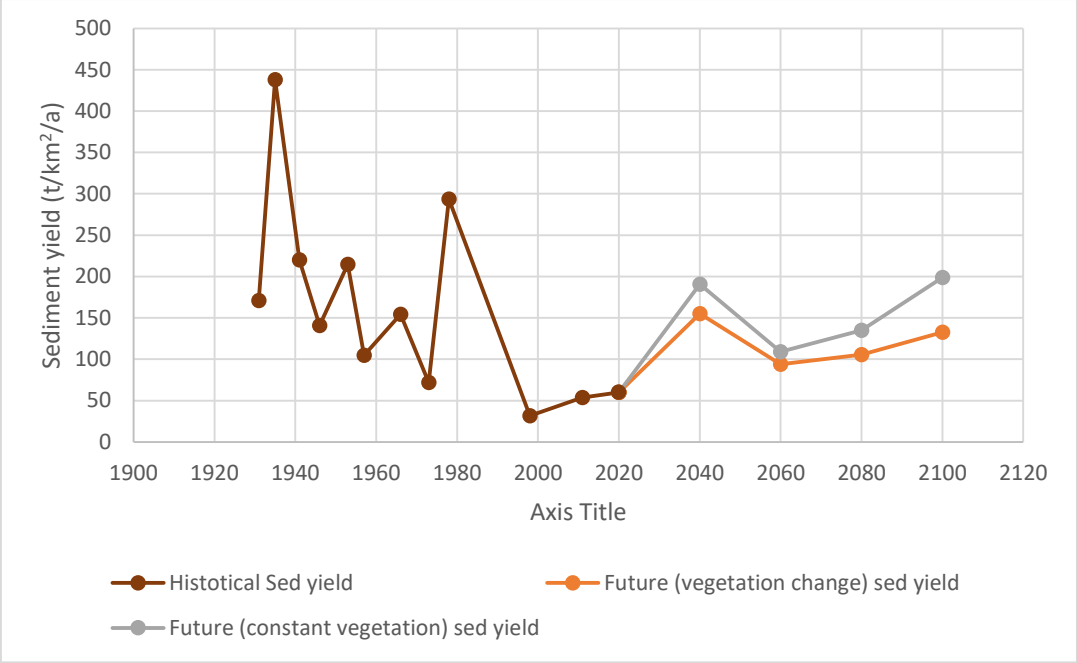

Figure 5.13: Historical - and simulated future sediment yield for Nqweba Dam

Figure 5.13 shows that the sediment yield for the Nqweba Dam catchment declined from the 1920s to the late 1990s, with the exception of the 1973 to 1978 period (the largest flood was recorded in 1974 – 3116 m^3/s). A slight increase in sediment yield is recorded from the late 1990s until the present (2020). According to the climate models and the application of the SHETRAN model, the predicted sediment yield for the Nqweba Dam catchment will increase through the following decades (until the end of the century). However, the predicted future sediment yield at the end of the century (up to 199 $t/km^2/a$ – Ref Table 5.8) is still lower than some historical measurements from the previous century. The reason for the decline in historical sediment yield will be evaluated and discussed in Section 5.4.1.

5.4.1 Analysing the decrease in historical sediment yield

To determine the historical catchment dynamics, the SHETRAN model was applied for all historical periods from 1930. The rainfall and evaporation data were described in Section 3.2.4, and the calibrated model, described in Section 4, was used for the simulations. Figure 5.14 illustrates the observed yearly flow (cumulative daily discharge) into the Nqweba Reservoir against the simulated flow. Table 5.10 gives a summary of the difference between the observed flow and simulated flow, as well as the average observed rainfall that was used in the simulations.

Table 5.10: Average rainfall for different periods and difference between observed and simulated flow into Nqweba Reservoir(1930-2020)

Period	Average rainfall (mm)	Approximate MAP(mm)	Cumulative Observed Discharge (m^3/s)	Cumulative Simulated Discharge (m^3/s)	%error
1930-1940	3251	325	5259	1660	-68
1940-1950	2871	287	3166	1281	-60
1950-1960	3253	325	2688	1564	-42
1960-1970	3291	329	3591	3873	8
1970-1980	3764	376	10867	9303	-14
1980-1990	3396	340	2899	2962	2
1990-2000	2952	295	769	1098	43
2000-2010	3616	362	1747	2263	30
2010-2020	3565	356	2595	3023	16

From Table 5.10 and Figure 5.14, it is clear that the SHETRAN model that was calibrated for the 2010-2020 period significantly underestimates the streamflow for the period between 1930 and 1960. The average MAP for this period (1930-1960) was 312 mm, with an average yearly flow of 370 m^3/s. Between 1990 and 2020, an average MAP of 338 mm and an average observed yearly flow of only 170 m^3/s were recorded. Therefore, although the average rainfall has increased from the early 1900s until the present, the average runoff (and sediment) ending up in the Nqweba Reservoir has reduced significantly. The reason for the decline in sediment yield can be determined by examining the history of the land-use practices in the Nqweba Dam catchment.

According to Du Toit (2013), the Kimberly – and Witwatersrand gold rush of 1877 to 1886 caused numerous prospectors to stream through the Karoo at the time, resulting in a great deal of damage to the landscape and vegetation by the early 1930s. The Korean War of 1950 to 1953 and freezing American soldiers resulted in a large wool demand. The large wool demand caused overstocking of sheep in the Nqweba Dam catchment to reach a peak during the mid-1950s. Poor farm management resulted in overgrazing and land degradation: Farmers did not like grass (that protect the soil) but preferred small shrubs because they argued that it is more durable during drought; A typical farmer during the early 1900s also had only three encampments (one for ewes, one for rams, and one for hamels), giving the land limited rest (Du Toit, 2013).

In the late 1950s and 1960s, the South African government implemented a compulsory stock reduction scheme, where farmers were paid not to graze livestock (Du Toit, 2013). According to Foster & Rowntree (2012), conservation efforts were implemented in the 1950s to mitigate soil erosion and improve water retention on hillslopes. In order to improve soil retention, Agave Americana

(Garingboom) was planted on eroded areas, which had a positive impact on soil retention. Improved land management practices by farmers and the shift from livestock to game farming for some parts of the Nqweba Dam catchment have improved the overall vegetation cover and catchment response to rainfall since the 1960s (Du Toit, 2013).

Another factor that needs to be considered is the construction of numerous farm dams within the catchment. According to a study conducted by Boardman *et al.* (2009), evidence suggests that small farm dams in badly eroded areas have a significant impact on sediment retention. In an area along the Compassberg (in the Nqweba Dam catchment) of approximately 80 km^2, 95 small farm dams were mapped, of which some were already full of sediment. Boardman *et al.* (2009) estimated that 2 million m^3 of sediment are stored in an area of 100 km^2, which results in 27000 t/km^2 if a sediment density of 1.35 t/m^3 is assumed.

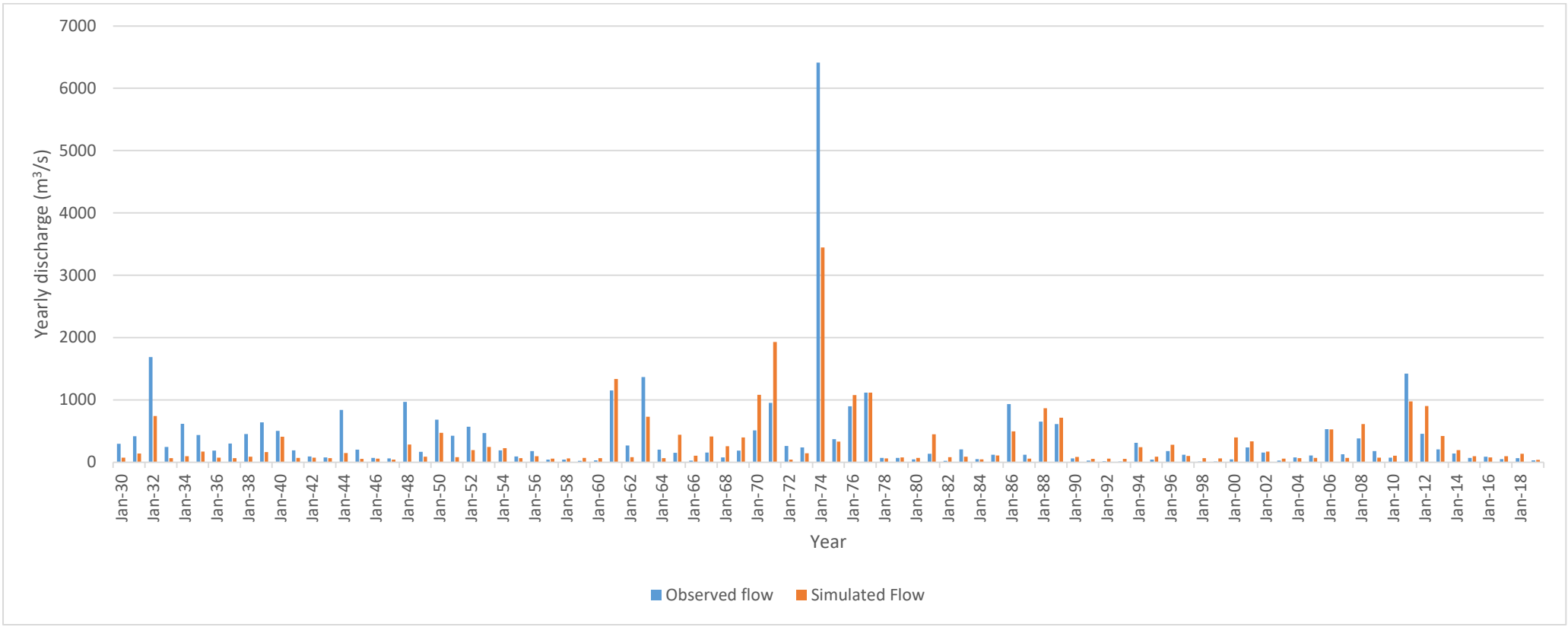

Figure 5.14: Observed yearly streamflow (cumulative daily discharge) against the simulated flow for Nqweba Dam catchment from 1930 to 2020

5.4.2 Impact of climate change on flood peaks by the end of the century

Figure 5.15 illustrates the daily flow into the Nqweba Reservoir for 2010-2020, as calibrated in Section 4.1. Figure 5.16 and Figure 5.17 illustrates the daily flow by the end of the century, as simulated for climate change (RCP 8.5) in Section 5.2 and 5.3. In order to estimate the possible impact of climate change on flood peaks, four flood peaks for the 2010-2020 period were compared to the corresponding flood peaks simulated for the end of the century. Table 5.11 and Table 5.12 summarize the increase in the magnitude of the flood peaks, as predicted by the climate models and simulated with the SHETRAN model.

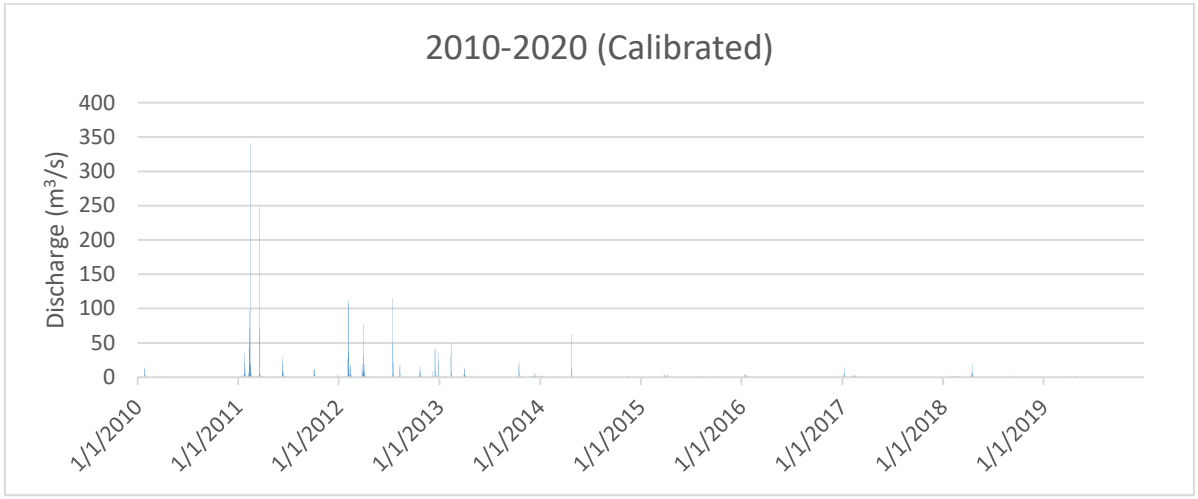

Figure 5.15: Calibrated daily flow into the Nqweba Reservoir for 2010 to 2020

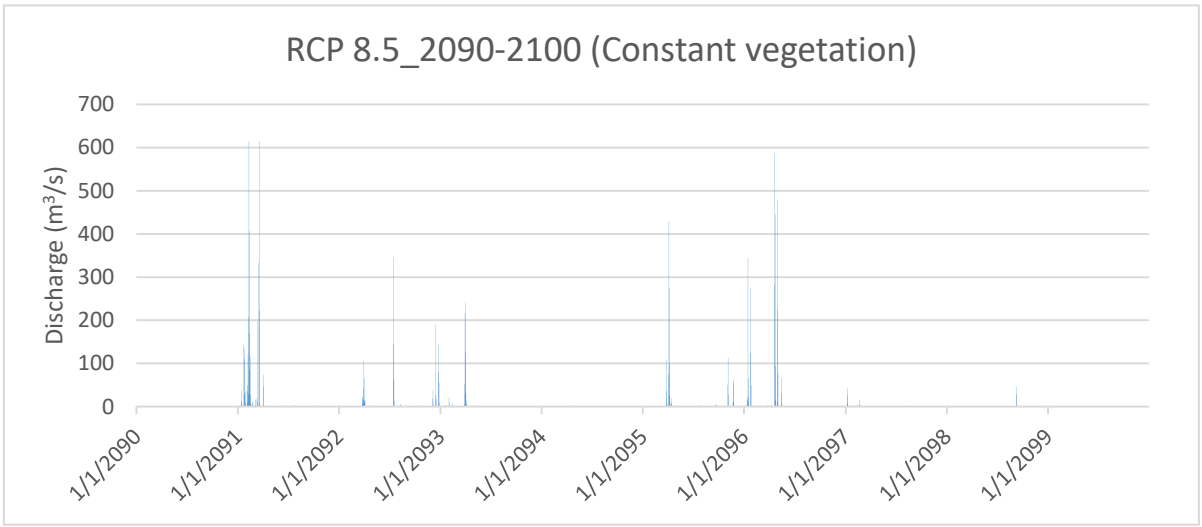

Figure 5.16: Predicted (simulated with constant vegetation) daily flow into the Nqweba Reservoir for 2090 to 2100

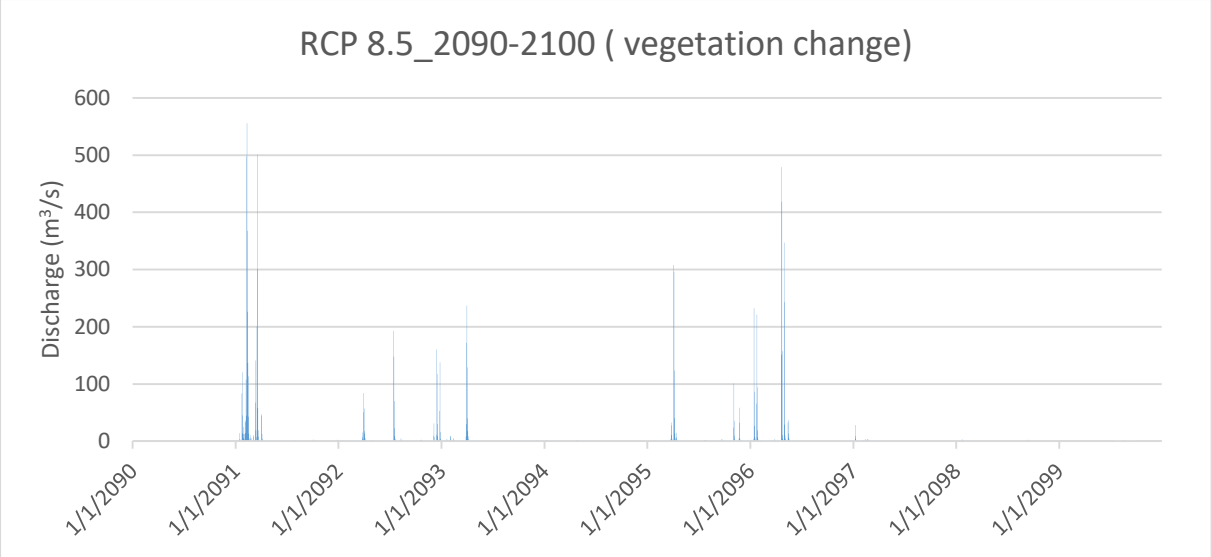

Figure 5.17: Predicted (simulated with changing vegetation) daily flow into Nqweba Reservoir for 2090 to 2100

Table 5.11: Simulated increase of flood peaks by the end of the century if the vegetation remains constant

Date	Current flood peak (m^3/s)	End of century flood- constant vegetation (m^3/s)	% increase
2/13/2011	340	613	80
3/18/2011	248	614	147
3/29/2012	77	107	39
7/14/2010	115	345	200

Table 5.12: Simulated increase of flood peaks by the end of the century if the vegetation change (improve)

Date	Current flood (m^3/s)	End of century simulation flood- Vegetation improve (m3/s)	% increase
2/13/2011	340	555	63
3/18/2011	248	500	101
3/29/2012	77	84	9
7/14/2010	115	192	67

From Table 5.11, it can be seen that an increase of up to 200 % for some flood peaks is predicted if the land cover does not improve by the end of the century. Table 5.12 illustrates that if the land cover improves, the climate models still predict an increase of up to 100 % for some flood peaks. It is important to note that the increase in magnitude is in relation to the flood peaks recorded between

2010 and 2020. Three historical flood peaks described in Section 3.2.5 are still higher than the predicted future flood peaks.

5.4.3 Identification of high sediment yield areas for possible future conditions

In Section 4.2, the Nqweba Dam catchment was divided into sub-catchments to identify the high sediment yield areas for the current catchment characteristics. It was assumed that the same areas would generate the highest sediment yield in the future. However, to verify this, the SHETRAN model was applied for the RCP 8.5 emission scenario (with and without vegetation change). The simulated sediment yield results for the sub-catchments for 2010-2020 and 2090-2100 are summarized in Table 5.13. From Table 5.13 it is observed that the same areas (sub-catchments S2 and S24) for present and possible future conditions will generate the highest sediment yield.

Table 5.13: Present and possible future simulated sediment yield (sub-catchment results)

Pour Point in Figure 4.7	2010-2020 Sediment yield (t/km^2/a)	2090-2100 sediment yield- constant vegetation(t/km^2/a)	2090-2100 sediment yield- vegetation change (t/km^2/a)
S1	113	335	206
S2	611	841	692
S3	206	358	197
S4	69	124	74
S5	122	236	140
S6	15	48	27
S7	113	364	207
S8	111	342	212
S9	95	270	198
S10	170	529	312
S11	174	303	177
S12	112	112	241
S13	120	277	172
S14	132	217	150
S15	92	192	112
S16	319	507	439
S17	165	253	138
S18	46	144	135
S19	116	204	265
S20	124	270	157
S21	79	171	108
S22	68	168	99

Pour Point in Figure 4.7	2010-2020 Sediment yield (t/km^2/a)	2090-2100 sediment yield- constant vegetation(t/km^2/a)	2090-2100 sediment yield- vegetation change (t/km^2/a)
S23	161	309	184
S24	537	764	604
S25	118	209	265
S26	21	49	28
S27	140	352	229
S28	26	66	40
S29	305	496	324
S30	82	161	140
S31	96	220	158
S32	204	492	231
S33	36	93	49
S34	32	68	63
S35*	57	199	133

6 Conclusion and recommendations

The main objective of this study was to determine the possible future impacts of climate change on sediment yield for a semi-arid catchment. The goal was achieved by calibrating the physically-based hydrological model, SHETRAN for the current catchment characteristics and climate data of the Nqweba Dam catchment near Graaff-Reinet in the Eastern Cape. Projected climate data for present and future periods were obtained from eleven downscaled GCMs and two emission scenarios to determine possible future rainfall and evaporation signals. The climate change signals were applied to the climate data that were used for the baseline (calibrated) period to represent possible future climate conditions. The possibility of vegetation change was also evaluated by modifying the SHETRAN model's vegetation properties in a structured manner. High sediment yield areas for present and possible future conditions were determined by identifying pour points in the rivers and dividing the catchment into sub-catchments. Section 6 concludes the findings of the study, identifies certain limitations, and gives recommendations for model application and further research.

6.1 Identification of study area and model calibration

The Nqweba Dam and catchment area were identified to conduct the research, because long term climate- and sediment data from gauging stations and reservoir surveys were available. The region is also faced with a real problem, because the Nqweba Reservoir has already lost approximately 46 % of its original storage capacity since the dam was constructed in 1925. The required data for SHETRAN simulations were obtained from numerous online sources, and the climate data was requested from Weather SA. A physical survey was conducted to obtain soil samples for twelve points in the catchment. The following limitations were identified:

- To obtain optimal results with the SHETRAN model, hourly rainfall data for the whole catchment is preferred. However, only daily rainfall data was available for limited points in the catchment. Therefore, it is highly probable that errors in the simulated results will be present;
- Although a physical survey was conducted, some soil and vegetation characteristics for large areas in the catchment are uncertain and were estimated. The availability of land cover distribution data is limited to only specific historical periods. Sub-soil conditions (soil depth and grading) are also uncertain due to limited borehole logs, making calibration and parameter verification difficult;

- For the water flow calibration, actual observed streamflow data was not available. The inflow into the Nqweba Reservoir was calculated from gauge plate readings and a dam balance. The additional variables in a dam balance calculation increase the uncertainty of the accuracy of the flood peaks; and
- For the sediment yield calibration, observed daily sediment load data was not available. The simulated sediment load had to be calibrated against accumulated sediment in the reservoir, which was calculated from DWS reservoir survey data.

Although these limitations exist, the SHETRAN model was successfully calibrated for the 2010-2020 period, with a 16 % error between the observed and simulated water flow. The accumulated sediment load was also successfully calibrated against the accumulated sediment in the reservoir. The model parameters were verified, and simulations were executed for all the decades between 1980 and 2010. It was determined that the accuracy between the simulated and observed results for the sediment yields vary between 2 % and 43 %. However, it was concluded that the larger errors were due to variability in catchment dynamics and limited rainfall data, and not an inaccurate model.

For the Nqweba Dam catchment, high sediment yield areas were identified by dividing the catchment into sub-catchments, and an average sediment yield of 57 t/km^2/a for the 2010-2020 period was observed. A SHETRAN model parameter sensitivity analysis was also conducted to identify the model parameters with the most significant influence on water flow and sediment yield simulation results. For future research and model calibration, it is recommended that high sensitive model parameters be used to calibrate flood peaks and less sensitive parameters to adjust the base flow.

6.2 Determination and application of climate change signals

Projected climate data from eleven climate models and two emission scenarios were obtained for the 2010-2020 baseline period and several future periods. For some future periods, individual models predict extreme climate signals in relation to the baseline period. Therefore, it is recommended that the average projected climate data for all models be used to calculate the climate change signals for each scenario and future period. By the middle of the century (2050-2060), average climate change rainfall signals of 1.11 and 1.12 were predicted for the RCP 4.5 and RCP 8.5 emission scenarios, respectively. By the end of the century (2090-2100), average rainfall signals of 1.24 and 1.29 were predicted for the RCP 4.5 and RCP 8.5 emission scenarios respectively. An increase of up to 200 % for some flood peaks were observed. For the same future periods and emission scenarios, average evaporation signals of 1.05 and 1.09, and 1.09 and 1.21 were predicted.

The rainfall and evaporation signals were applied to the observed climate data for the baseline (2010-2020) period, and the calibrated SHETRAN model (with modified climate data), was implemented. Due to the predicted increase in average rainfall, the possibility of vegetation change was introduced, and four scenarios for each future period were evaluated. Included were two emission scenarios with two different land cover scenarios, resulting in an uncertainty envelope with minimum and maximum predicted sediment yields for each period. For the middle of the century (2050-2060), sediment yields between 94 and 109 t/km^2/a are predicted for the Nqweba Dam catchment. By the end of the century (2090-2100), sediment yields between 133 and 199 t/km^2/a are predicted. Although an increase (due to climate change) of up to 232 % in the average sediment yield from the baseline period is predicted, it is still lower than the historical sediment yield of 293 t/km^2/a recorded in the Nqweba Dam catchment during the 1973-1978 period. The future sediment yield predictions for the Nqweba Dam catchment are also relatively low compared to current observations in other South African regions.

6.3 Final remarks and recommendation for further research

Estimating the future impacts of climate change on sediment yield with a physically-based model, using climate change signals obtained from climate models, and applying them on questionable observed climate data, will impose errors in the results. It was concluded that numerous uncertainties are present and that the simulated (sediment yield) climate change results must be interpreted as crude approximations and not exact values. When the historical catchment dynamics and sediment data were analysed, it was determined that the Nqweba Dam catchment had experienced numerous changes regarding land cover and catchment response. The effect of overgrazing, poor farm management, and the construction of numerous farm dams exceeds the impact of climate change on sediment yield for the specific catchment. It is suggested that improved farm management practices must be maintained. In high sediment yield areas, farmers must be educated on the impact of overgrazing and poor farm management on erosion and the downstream effect.

Nevertheless, according to the average predictions of eleven climate models, it was concluded that climate change would cause an increase in the average sediment yield for the Nqweba Dam catchment. An increase (in relation to the 2010-2020 period) between 122 % and 232 % in average sediment yield (by the end of the century) is possible, and an increase of up to 200 % for flood peaks are possible. It is suggested that the increase in sediment yield due to climate change must be taken into account when environmental planning and hydraulic design criteria are considered. Although the increased future sediment yield (due to climate change) for the Nqweba Catchment is still lower than historical observations, it may not be the case for other regions in South Africa. Recommendations for further research include the following:

- The validity of the SHETRAN model must be evaluated by investigating the future impacts of climate change on sediment yield for other areas (especially winter rainfall regions) in South Africa;
- Investigation of the impacts of farm dams on sediment yield, sediment trap efficiency, and possible dam breaching with downstream effects; and
- A more detailed study of the impact of climate change on vegetation and evapotranspiration.

References

Anthoni, J.F. 2000. *Soil erosion and conservation - Part 1*. [Online], Available: http://www.seafriends.org.nz/enviro/soil/erosion1.htm#concern [2019, November 26].

Arnold, J.G., Srinivasan, R., Muttiah, R.S. & Williams, J.R. 1998. LARGE AREA HYDROLOGIC MODELING AND ASSESSMENT PART I : MODEL DEVELOPMENT ' basin scale model called SWAT (Soil and Water speed and storage , advanced software debugging policy to meet the needs , and the management to the tank model (Sugawara et al ., 1. 34(1):73–89.

Basson, G.R. & Rooseboom, A. 1997. *Dealing with reservoir sedimentation: WRC Report No. TT 91/97*. Pretoria.

Bathurst, J.C. 2011. Predicting Impacts of Land Use and Climate Change on Erosion and Sediment Yield in River Basins Using SHETRAN. *Handbook of Erosion Modelling*. 263–288.

Bathurst, J. & Purnama, A. 1991. Design and application of a sediment and contaminant transport modelling system. *IAHS Publication*. (203):305–313.

Bathurst, J.C., Sheffield, J., Vicente, C., White, S.M. & Romano, N. 2002. Modelling large basin hydrology and sediment yield with sparse data : The Agri Basin , and Sediment Yield with Sparse Data : *The Geographical Journal*. 170(October):440.

Beasley, D.B., Huggins, L.F. & Monke, E.J. 2013. ANSWERS: A Model for Watershed Planning. *Transactions of the ASAE*. 23(4):0938–0944.

Bennett, S.J. & Wells, R.R. 2019. Gully erosion processes, disciplinary fragmentation, and technological innovation. *Earth Surface Processes and Landforms*. 44(1):46–53.

Bergant, K., Bogataj, L.K. & Trdan, S. 2006. Uncertainties in modelling of climate change impact in future: An example of onion thrips (Thrips Tabaci Lindeman) in Slovenia. *Ecological Modelling*. 194(3):244–255.

Bicknell, B.R., Imhoff, J.C. & Kittle, J.L. 1996. HSPF-User's Manual. *Time*. (September).

Birkinshaw, S.J. 2013. SHETRAN Version 4 Data Requirements , Data Processing and Parameter Values Executive Summary. *Data Processing*.

Birkinshaw, S.J. 2016. User Guide and Data Input Manual.

Boardman, J., Foster, I., Rowntree, K., Mighall, T. & Parsons, T. 2009. Small farm dams: A ticking time bomb? *Water Wheel*. 8(4):30–35.

Boardman, J., Foster, I.D.L., Rowntree, K.M., Favis-Mortlock, D.T., Mol, L., Suich, H. & Gaynor, D. 2017. Long-term studies of land degradation in the Sneeuberg uplands, eastern Karoo, South Africa: A synthesis. *Geomorphology*. 285:106–120.

Borah, D.K. & Bera, M. 2003. Watershed - Scale Hydrologic and Nonpoint - Source Pollution Models :Review of Mathematical Bases. 46(6):1553–1566.

Braune, E. 1984. *Density of Sediment in South African Reservoirs. Technical Report 119*.

Castillo, C. & Gómez, J.A. 2016. A century of gully erosion research: Urgency, complexity and study approaches. *Earth-Science Reviews*. 160:300–319.

CCCMA. 2017. *Environment and Climate Change Canada - CanESM2*. [Online], Available: https://www.ec.gc.ca/ccmac-cccma/default.asp?lang=En&n=1A3B7DF1-1&wbdisable=true [2020, August 31].

Clark, L.A. & Wynn, T.M. 2013. Methods for Determining Streambank Critical Shear Stress and Soil Erodibility: Implications for Erosion Rate Predictions. *Transactions of the ASABE*. 50(1):95–106.

CSAG. 2020. *Climate Information Platform*. [Online], Available: https://cip.csag.uct.ac.za/webclient2/datasets/africa-merged-cmip5/ [2020, June 17].

Dunne, J.P. 2013. *GFDL Earth System Models*. [Online], Available: https://www.gfdl.noaa.gov/earth-system-model/ [2020, August 31].

DWS. 2011. *Dam List*. [Online], Available: https://www.gov.za/about-sa/water-affairs?gclid=CjwKCAjw_NX7BRA1EiwA2dpg0m3-uT1phTaOWqFh50XAtsMlBL6m_bBWjtUNODy0_8hgWCaDB-oENBoC6JoQAvD_BwE [2019, August 26].

Ellis, F. & Lambrechts, J.J.N. 1986. *THE KAROO BIOME: a preliminary synthesis, Part 1*. Pretoria.

Engelund, F. & Hansen, E. 1967. *A Monograph on sediment transport in alluvial streams*. Copenhagen.

Evans, R. 2013. Assessment and monitoring of accelerated water erosion of cultivated land - when will reality be acknowledged? *Soil Use and Management*. 29(1):105–118.

Ewen, J. & Parkin, G. 1996. Validation of catchment models for predicting land-use and climate change impacts. 1. Method. *Journal of Hydrology*. 175(1–4):583–594.

Ewen, J., Parkin, G. & O'Connell, P.E. 2011. SHETRAN: Distributed River Basin Flow and Transport Modeling Systen. (JULY):250–258.

FAO. 2019. *Soil erosion: The Greatest challange to sustainablesoil management*. Rome.

Fey, M. V. 2010. A short guide to the soils of South Africa , their distribution and correlation with World Reference Base soil groups. *19th World Congress of Soil Science, Soil Solutions for a Changing World*. 32–35.

Foster, I.D. & Rowntree, K.M. 2012. Sediment yield changes in the semi-arid Karoo: A Paleoenvironmental reconstruction of sediments accumulating in Cranmere Reservoir, Eastern Cape, South Africa. *Zeitschift fur Geomorphology*. 53(3):131–146.

Freeze, R.A. & Cherry, J.A. 1979. *Groundwater*. illustrate ed. Michigan: Prentice-Hall.

Furphy, D. 2013. *What on Earth is an RCP?* [Online], Available: https://medium.com/@davidfurphy/what-on-earth-is-an-rcp-bbb206ddee26 [2020, July 09].

Grenfell, S.E., Grenfell, M.C., Rowntree, K.M. & Ellery, W.N. 2014. Fluvial connectivity and climate: A comparison of channel pattern and process in two climatically contrasting fluvial sedimentary systems in South Africa. *Geomorphology*. 205:142–154.

Gyssels, G., Poesen, J., Bochet, E. & Li, Y. 2005. Impact of plant roots on the resistance of soils to erosion by water: A review. *Progress in Physical Geography*. 29(2):189–217.

Hargreaves, G.H. & Allen, R.G. 2003. History and evaluation of hargreaves evapotranspiration equation. *Journal of Irrigation and Drainage Engineering*. 129(1):53–63.

Henderson, F.M. 1966. *Open Channel Flow*. New York: The MacMillan Company.

Herrmann, S.M., Anyamba, A. & Tucker, C.J. 2005. Exploring relationships between rainfall and vegetation dynamics in the sahel using coarse resolution satellite data. *Proceedings, 31st International Symposium on Remote Sensing of Environment, ISRSE 2005: Global Monitoring for Sustainability and Security*.

Hughes, D. 2007. CHAPTER 4 . MODELLING OF CLIMATE CHANGE IMPACTS ON HYDROLOGY WITH THE PITMAN MODEL by. (2005):44–48.

IPCC-TGICA. 2007. General Guidelines on the Use of Scenario Data for climate impact and adaptation assessment. *Finnish Environment Institute*. 312(June):66.

IPCC. 2007. [Climate change 2007] : The physical science basis : summary for policymakers and technical summary and frequently asked questions ; part of the Working Group I contribution to the Fourth Assessment Report of the Intergovernmental Panel on Climate Change. *Proceedings of the Alpine Snow Workshop, Munich, October 5-6, Germany | HeBIS-Verbundkatalog*. 8:142. [Online], Available: http://bluemarble.nasa.gov.

Jacob, D. & Hurk, V. den. 2009. Climate Change Scenarios at the Global and Local Scales. In F. Ludwig,

P. Kabat, H. VanSchaik, & M. Van der Valk (eds.). London: Earthscan *Climate Change Adaptation in the Water Sector*. 23–33.

Ji, D., Wang, L., Feng, J., Wu, Q., Cheng, H., Zhang, Q., Yang, J., Dong, W., et al. 2014. Description and basic evaluation of BNU-ESM version 1. *Geoscientific Model Development Discussions*. 7(2):1601–1647.

Kamphuis, J.W. & Hall, K.R. 2008. Cohesive Material Erosion by Unidirectional Current. *Journal of Hydraulic Engineering*. 109(1):49–61.

Kiehl, J.T. & Trenberth, K.E. 1997. Earth's Annual Global Mean Energy Budget. *Bulletin of the American Meteorological Society*. 78(2):197–208.

Kinnell, P.I.A. 2016. A review of the design and operation of runoff and soil loss plots. *Catena*. 145:257–265.

Kinsel, W.G. 1980. *CREAMS: A field scale model for Chemicals, Runoff, and Erosion, in Agricultural Management Systems, Conservation Report no. 26*.

Laker, M.C. 2004. Advances in soil erosion, soil conservation, land suitability evaluation and land use planning research in South Africa. *South African Journal of Plant and Soil*. 21(5):345–368.

Levy, R. 2019. *NASA Earth Observatory*. [Online], Available: https://earthobservatory.nasa.gov/global-maps/TRMM_3B43M/MOD_NDVI_M#:~:text=One of the most important,to a burst of green. [2020, August 06].

Lukey, B.T., Bathurst, J.C., Hiley, R.A. & Ewen, J. 1995.

Lynch, S.D. 2004. *Development of a raster database of annual, monthly and daily rainfall for Southern Africa: Report to the water research commission*. Pretoria.

Marshall, J.S. & Palmer, W.M. 1950.

Meddi, M., Boucefiane, A. & Belabbes, A.S. 2010. Impact of climate change on runoff in the Chéllif basin (Algeria). *IAHS-AISH Publication*. 340(October):95–102.

Miller, C.R. 1953. *Determination of the Unit Weight of Sediment for use in Sediment Volume Computations*. Denver, Colorado.

Minnaar, A. 1987. Graaf-Reinet's water problems. *Institute for Historical Research*. 75–77.

Morgan, P.C.R., Quiton, J.N., Smith, R.E., Govers, G., Poesen, J.W.A., Auerswald, K. & Chisci, G. 1998. The European Soil Erosion Model (Eurosem): A Dynamic Approach For Predicting Sediment Transport From Fields And Small Catchments. *Earth Surface Processes and Landforms*. 544:527–

544.

Msadala, V., Gibson, L., Le Roux, J., Rooseboom, A. & Basson, G.R. 2010. *Sediment Yield Prediction for South Africa : 2010 Edition, WRC Report No. 1765/1/10*.

Palmer, A.R. 1989. The vegetation of the Karoo Nature Reserve, Cape Province. I. A phytosociological reconnaissance. *South African Journal of Botany*. 55(2):215–230.

Palmer, E. 2012. *The Plains of the Camdeboo: The Classic book of the Karoo*. 1st ed. Cape Town: Penguin Books.

Pandey, A., Himanshu, S.K., Mishra, S.K. & Singh, V.P. 2016. Physically based soil erosion and sediment yield models revisited. *Catena*. 147:595–620.

Parkin, G. 1995. SHETRAN Water Flow Component, Equations and Algorithms.

Parkin, G., O'Donnell, G., Ewen, J., Bathurst, J.C., O'Connell, P.E. & Lavabre, J. 1996. Validation of catchment models for predicting land-use and climate change impacts. 2. Case study for a Mediterranean catchment. *Journal of Hydrology*. 175(1–4):595–613.

PENMAN, H.L. 1948. Natural evaporation from open water, hare soil and grass. *Proceedings of the Royal Society of London. Series A, Mathematical and physical sciences*. 193(1032):120–45. [Online], Available: http://www.ncbi.nlm.nih.gov/pubmed/18865817.

Poesen, J. 2018. Soil erosion in the Anthropocene: Research needs. *Earth Surface Processes and Landforms*. 43(1):64–84.

Pretorius, D.J. 1995. *The development of a Soil Degradation ManagementSupport System*. Pretoria.

Pretorius, D.J. 1998. *The development of Land degradation Monitoring with the aid of Remote Sensing and GIS Technology*. Pretoria: ISCW Report No. GW/A/98/27.

Rawls, W.J., Brakensiek, C.L. & Saxton, K.E. 1982. Estimation of soil water properties. *Transactions - American Society of Agricultural Engineers*. 25(5).

Rooseboom, A., Verster, E., Zietsman, H.L. & Lotriet, H.H. 1992. *The Development of the New Sediment Yield Map of Southern Africa*.

Le Roux, J. 2014. *Soil erosion in South Africa - its nature and distribution*. [Online], Available: https://www.grainsa.co.za/soil-erosion-in-south-africa---its-nature-and-distribution [2019, November 22].

Le Roux, J.J., Morgenthal, T.L., Malherbe, J., Pretorius, D.J. & Sumner, P.D. 2008. Water erosion prediction at a national scale for South Africa. *Water SA*. 34(3):305–314.

Rutter, A.J., Kershaw, K.A., Robins, P.C. & Morton, A.J. 1972. A predictive model of rainfall interception in forests, 1. Derivation of the model from observations in a plantation of Corsican Pine. *Agricultural Meteorology*. 9(1971/1972):367–384.

Sadeghi, S.H.R., Gholami, L., Darvishan, A.K. & Saeidi, P. 2014. A review of the application of the MUSLE model worldwide. *Hydrological Sciences Journal*. 59(2):365–375.

SALTER, P.J. & WILLIAMS, J.B. 1965. the Influence of Texture on the Moisture Characteristics of Soils: I. a Critical Comparison of Techniques for Determining the Available-Water Capacity and Moisture Characteristic Curve of a Soil. *Journal of Soil Science*. 16(1):1–15.

SANBI. 2012. *BGIS Map Viewer*. [Online], Available: bgisviewer.sanbi.org/Html5Viewer/Index.html?configBase=http://bgisviewer.sanbi.org/Geocortex/Essentials/REST/sites/Vegmap/viewers/National_Vegetation_Map_2009/virtualdirectory/Resources/ [2020, April 13].

Savabi, M.R., Rawls, W.J. & Knight, R.W. 2007. Water Erosion Prediction Project (WEPP) Rangeland Hydrology Component Evaluation on a Texas Range Site. *Journal of Range Management*. 48(6):535.

Saxton, K.E., Rawls, W.J., Romberger, J.S. & Papendick, R.I. 1986. Estimating generalized soil-water characteristics from texture. *Soil Science Society of America Journal*. 50(4):1031–1036.

Schulze, R.. 2011. The Hydrological Model Used in Climate Change Impact Studies on the South African Water Sector. In R.E. Schulze (ed.). Pretoria: WRC Report TT 518/12 *A 2011 Perspective on Climate Change and the South African Water Sector.* 39–57.

Schulze, R.E., Knoesen, D.M., Kunz, R.. & Lumsden, T.G. 2014. General Circulation Models and Downscaling for South African Climate Change Impacts Studies: A 2011 Perspective. In R.E. Schulze (ed.). Pretoria: WRC Report TT 518/12 *A 2011 Perspective on Climate Change and the South African Water Sector.* 21–30.

Di Silvo, G. & Basson, G. 2008. Erosion and sediment dynamics from catchment to coast. *IHP-VI Technical Document in Hydrology N°82 UNESCO Working Series SC-2008/WS/34*. (82):48. [Online], Available: http://www.unesco.org/water/ihp.

Slaughter, A.R. 2011. Modelling the relationship between flow and water quality in South African rivers . (May).

Du Toit, J. 2013. *Karoo Space - At the heart of South Africa*. [Online], Available: http://karoospace.co.za/progressive-farmers-of-graaff-reinet/ [2020, October 07].

Tongwen, W.U., Lianchun, S., Weiping, L.I., Zaizhi, W., Hua, Z., Xiaoge, X.I.N., Yanwu, Z., Li, Z., et al. 2014. An Overview of BCC Climate System Model Development and. *Journal of Meteorlogical Research*. 28(1):34–56.

Torri, D. & Borselli, L. 2012. Water Erosion. In second ed. Boca Raton: CRC Press *Handbook of soil sciences resources management and environmental impacts*. 22–1 to 22–9.

UNM. 2008. Soil Texture Index. (February):1–6. [Online], Available: http://www.unm.edu/~jplaut/Texindex.htm.

De Villiers, J.W.L. & Basson, G.R. 2007. Modelling of long-term sedimentation at Welbedacht Reservoir, South Africa. *Journal of the South African Institution of Civil Engineering*. 49(4):10–18.

Voldoire, A., Sanchez-Gomez, E., Salas y Mélia, D., Decharme, B., Cassou, C., Sénési, S., Valcke, S., Beau, I., et al. 2013. The CNRM-CM5.1 global climate model: Description and basic evaluation. *Climate Dynamics*. 40(9–10):2091–2121.

Watanabe, M., Suzuki, T., O'Ishi, R., Komuro, Y., Watanabe, S., Emori, S., Takemura, T., Chikira, M., et al. 2010. Improved climate simulation by MIROC5: Mean states, variability, and climate sensitivity. *Journal of Climate*. 23(23):6312–6335.

Watanabe, S., Hajima, T., Sudo, K., Nagashima, T., Takemura, T., Okajima, H., Nozawa, T., Kawase, H., et al. 2011. MIROC-ESM 2010: Model description and basic results of CMIP5-20c3m experiments. *Geoscientific Model Development*. 4(4):845–872.

Wessels, K.J., Van den Berg, H.M., Van der Merve, J.P.A., Smith, H.J., Van Zyl, A.J. & Twyman, L. 2001. *Mapping and monitoring the conservation status of the natural resources of Mpumalanga province by means of remote sensing and GIS technology.* Pretoria.

Wicks, J.M. & Bathurst, J.C. 1996. SHESED: A physically based, distributed erosion and sediment yield component for the SHE hydrological modelling system. *Journal of Hydrology*. 175(1–4):213–238.

Wischmeier, W.H. 1959. A Rainfall Erosion Index for a Universal Soil-Loss Equation1. *Soil Science Society of America Journal*. 23(3):246.

Yalin, M.S. 1963. An Expression for Bed-Load Transportation. *Journal of Hydraulic Division of the American Society of Civil Engineers*. 89(3):221–250.

Yang, C.T. 2003. *Sediment Transport Theory and Practice*. Florida: Krieger Pub Co.

Yukimoto, S., Adachi, Y., Hosaka, M., Sakami, T., Yoshimura, H., Hirabara, M., Tanaka, T.Y., Shindo, E., et al. 2012. A new global climate model of the Meteorological Research Institute: MRI-CGCM3: -Model description and basic performance-. *Journal of the Meteorological Society of Japan*.

90(A):23–64.

Zhou, T., Wang, B., Yu, Y., Liu, Y., Zheng, W., Li, L., Wu, B., Lin, P., et al. 2018. The FGOALS climate system model as a modeling tool for supporting climate sciences: An overview. *Earth and Planetary Physics*. 2(4):276–291.

Ziervogel, G., New, M., Archer van Garderen, E., Midgley, G., Taylor, A., Hamann, R., Stuart-Hill, S., Myers, J., et al. 2014. Climate change impacts and adaptation in South Africa. *Wiley Interdisciplinary Reviews: Climate Change*. 5(5):605–620.

Appendix A: Soil Characteristics

Table A-1: Sediment size ranges

Sediment	Diameter (mm)
Very large boulders	4096 – 2048
Large cobbles	2048 – 1024
Medium boulders	1024 – 0512
Small boulders	512 – 256
Large cobbles	256 – 128
Small cobbles	128 – 64
Very coarse gravel	64 – 32
Coarse gravel	32 – 16
Medium gravel	16 – 8
Fine gravel	8 – 4
Very fine gravel	4 – 2
Very coarse sand	2 – 1
Coarse sand	1 – 0.5
Medium sand	0.5 – 0.25
Fine sand	0.25 – 0.125
Very fine sand	0.125 – 0.062
Coarse silt	0.062 – 0.031
Medium silt	0.031 – 0.016
Fine silt	0.016 – 0.008
Very fine silt	0.008 – 0.004
Coarse clay	0.004 - 0.002
Medium clay	0.002 - 0.001
Fine clay	0.0010 - 0.0005
Very fine clay	0.0005 - 0.00024

Table A-2: Saturated Conductivity for different soil types(Rawls *et al.*, 1982)

Soil type	Fraction Sand	Fraction Clay	Saturated water content	Residual water content	Saturated conductivity (m/day)
Clay	0.2	0.6	0.54	0.326	0.014
Silty Clay	0.1	0.4	0.53	0.21	0.02
Silty Clay Loam	0.1	0.27	0.51	0.14	0.04
Silt Loam	0.1	0.1	0.45	0.09	0.16
Clay Loam	0.35	0.27	0.49	0.15	0.055
Sandy Silt Loam	0.35	0.1	0.43	0.09	0.32
Sandy Clay	0.52	0.4	0.50	0.23	0.03
Sandy Clay Loam	0.65	0.24	0.46	0.17	0.1
Sandy Loam	0.65	0.1	0.41	0.1	0.62
Loamy Sand	0.85	0.06	0.37	0.075	1.47
Sand	0.92	0.05	0.35	0.07	5.04
Peat	N/A	N/A	0.91	0.32	0.46

Table A-3: Van Genuchten parameters for different soil types(Rawls *et al.*, 1982)

Soil type	Fraction Sand	Fraction Clay	Van Genuchten α (/cm^3)	Van Genuchten n^3
Clay	0.2	0.6	0.00458	1.443
Silty Clay	0.1	0.4	0.00654	1.531
Silty Clay Loam	0.1	0.27	0.00724	1.608
Silt Loam	0.1	0.1	0.00515	1.681
Clay Loam	0.35	0.27	0.00923	1.657
Sandy Silt Loam	0.35	0.1	0.00838	1.587
Sandy Clay	0.52	0.4	0.01069	1.879
Sandy Clay Loam	0.65	0.24	0.01236	2.071
Sandy Loam	0.65	0.1	0.01441	1.736
Loamy Sand	0.85	0.06	0.01986	1.793
Sand	0.92	0.05	0.02296	1.847
Peat	N/A	N/A	0.012	1.536

Appendix B: Vegetation Parameters

Table B-1: Canopy and leaf Parameters (Birkinshaw, 2013)

Vegetation Type	Canopy drainage		Canopy storage	Vegetation cover indices	
	CK (mm/s)	Cb (mm/s)	CSTACAP (mm)	PLAI	CLAI
Arable	0.0000014	5.1	1.5	1	6
Bare ground	0	0	0	0	1
Grass	0.0000014	5.1	1.5	1	6
Deciduous Forest	0.0000014	5.1	5.0	1	6
Evergreen Forest	0.0000014	5.1	5.0	1	6
Shrubs	0.0000014	5.1	1.5	1	3
Urban	0.0000014	5.1	0.3	0.3	1

Table B-2: Root density function for standard vegetation types (Birkinshaw, 2013)

Vegetation type	Total dept of roots (m)	Depth of layer below ground surface														
		0.1	0.2	0.3	0.4	0.5	0.6	0.7	0.8	0.9	1	1.2	1.4	1.6	1.8	2
Arable	**0.8**	0.31	0.23	0.17	0.1	0.07	0.06	0.04	0							
Bare ground	**0.1**	1														
Grass	**1**	0.25	0.18	0.15	0.12	0.1	0.08	0.06	0	0.02	0.01					
Deciduous Forest	**1.6**	0.18	0.14	0.13	0.11	0.09	0.08	0.07	0.1	0.04	0.03	0.04	0.03	0.02		
Evergreen Forest	**2**	0.13	0.12	0.11	0.1	0.09	0.08	0.07	0.1	0.05	0.03	0.06	0.04	0.03	0.02	0.01
Shrubs	**1**	0.25	0.18	0.15	0.12	0.1	0.08	0.06	0	0.02	0.01					
Urban	**0.5**	0.4	0.3	0.2	0.07	0.03										

Appendix C: Vegetation cover in Nqweba Dam catchment

Figure C-1: Camdeboo Escarpment thicket

Figure C-2: Upper Karoo Hardeveld

Figure C-3: Karoo grassland

Appendix D: Soil sample properties

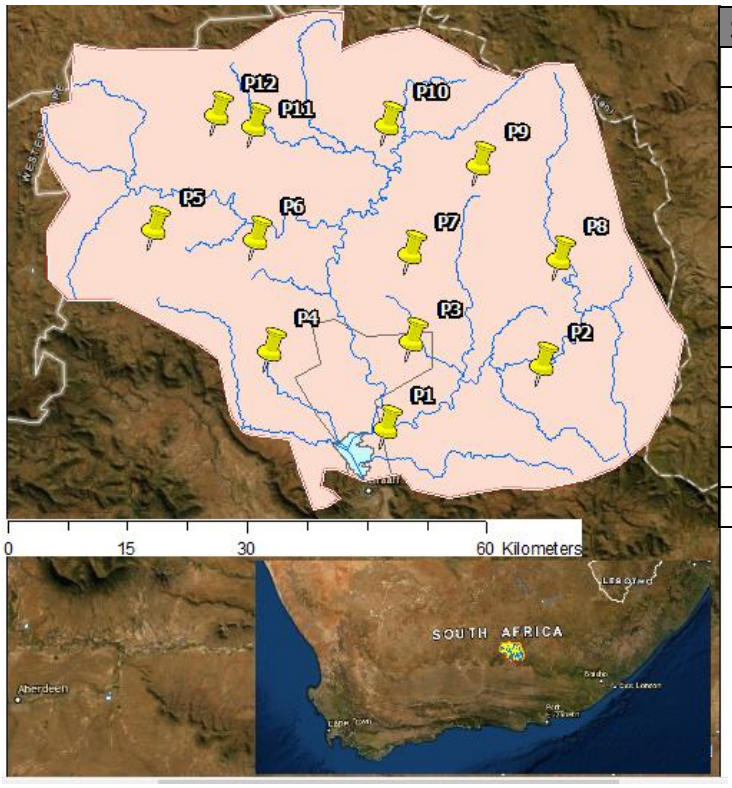

Sample	Latitude	Longitude
P1	-32.179	24.564
P2	-32.11209	24.77442
P3	-32.08215	24.60184
P4	-32.08874	24.41233
P5	-31.94901	24.26416
P6	-31.96268	24.3969
P7	-31.98337	24.60148
P8	-31.99282	24.799
P9	-31.88455	24.69659
P10	-31.83609	24.57641
P11	-31.83447	24.39897
P12	-31.82145	24.35111

Figure D-1: Location of soil samples obtained in Nqweba Dam catchment

Table D-1: Grading for catchment soil samples P1, P4, P5, and P7*

Diameter (mm)	P1 Cumulative Percentage Passing (%)	P4 Cumulative Percentage Passing (%)	P5 Cumulative Percentage Passing (%)	P7 Cumulative Percentage Passing (%)
75	100.00	100.00	100.00	100.00
50	100.00	100.00	100.00	100.00
37.5	100.00	100.00	100.00	78.59
19	100.00	100.00	100.00	70.85
9.5	99.59	100.00	100.00	63.22
4.75	99.38	99.76	100.00	57.18
2.36	99.17	99.76	99.66	48.06
1.18	99.17	98.05	99.66	44.31
0.6	97.65	89.48	90.46	40.56
0.3	94.60	84.34	67.46	37.55
0.15	82.39	79.20	39.86	34.55
0.075	47.30	70.63	19.93	30.80
0.0342	15.26	37.69	6.13	17.27
0.0218	13.73	30.84	6.13	15.77

Diameter (mm)	P1 Cumulative Percentage Passing (%)	P4 Cumulative Percentage Passing (%)	P5 Cumulative Percentage Passing (%)	P7 Cumulative Percentage Passing (%)
0.0127	12.21	25.70	6.13	14.27
0.0090	10.68	22.27	4.60	13.52
0.0064	9.15	18.85	4.60	12.76
0.0032	6.10	11.99	4.60	11.26
0.0013	4.58	8.57	3.07	9.01

*The grading for the other sample points can be related to one of the given four (Ref. Table 3.2)

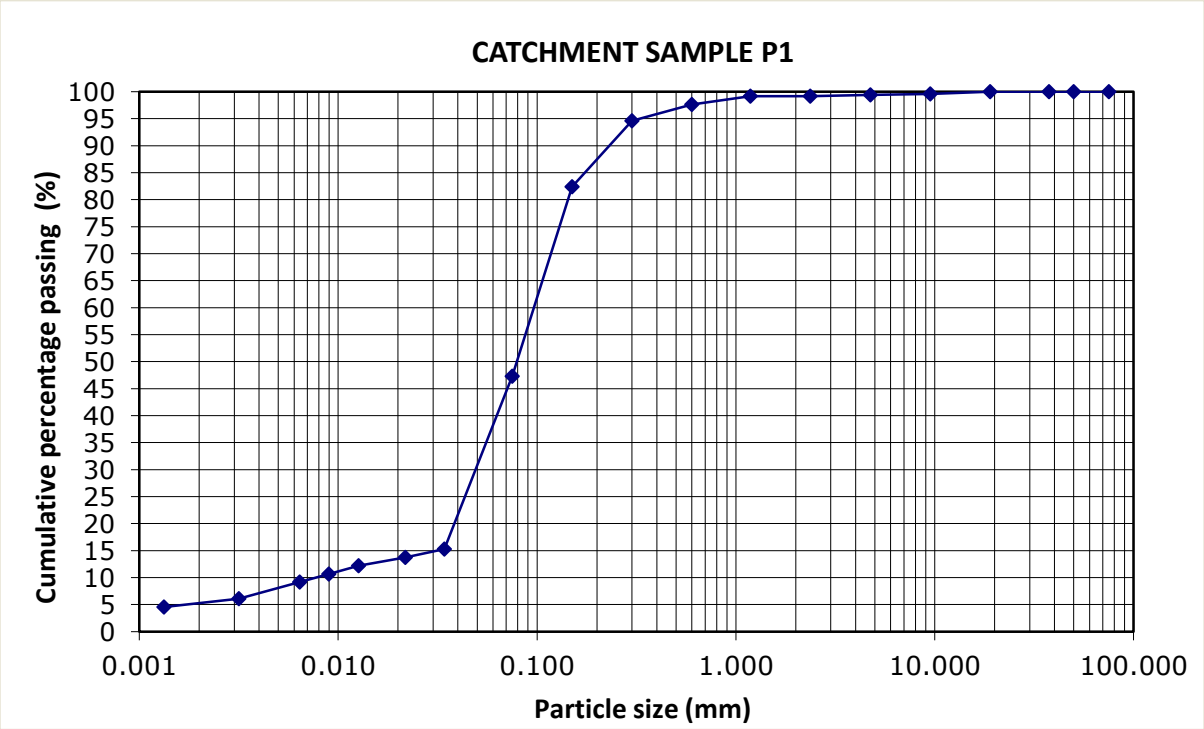

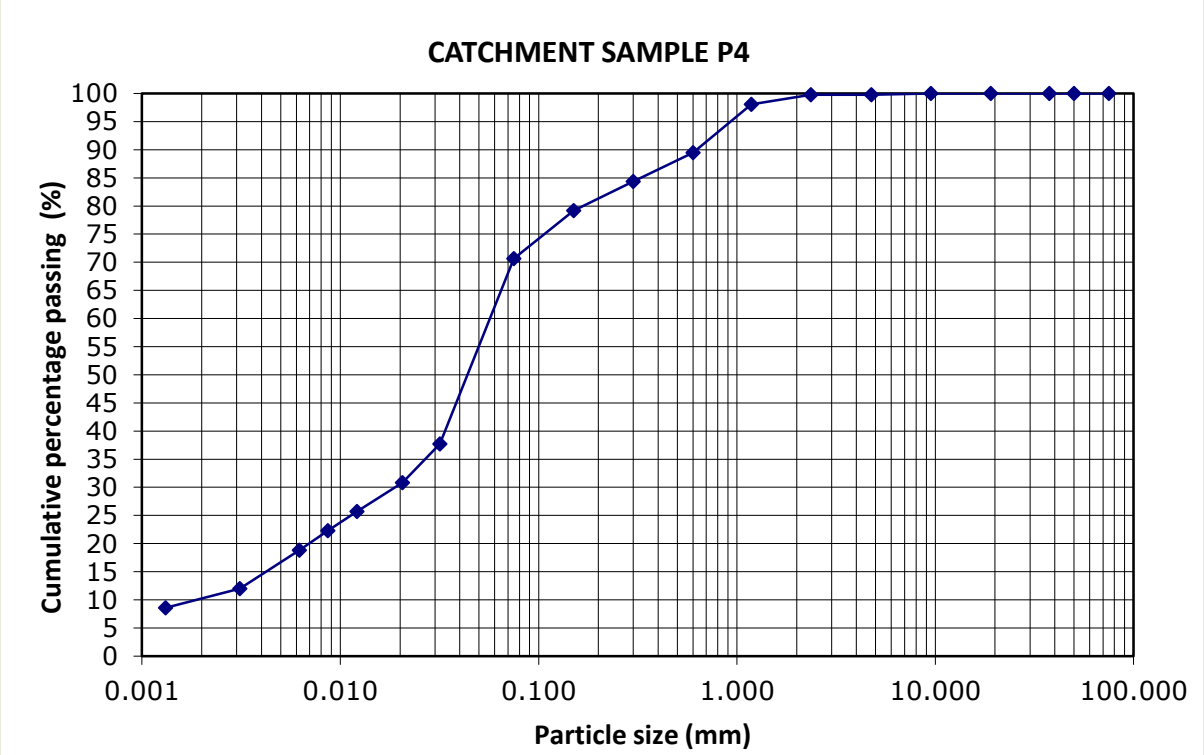

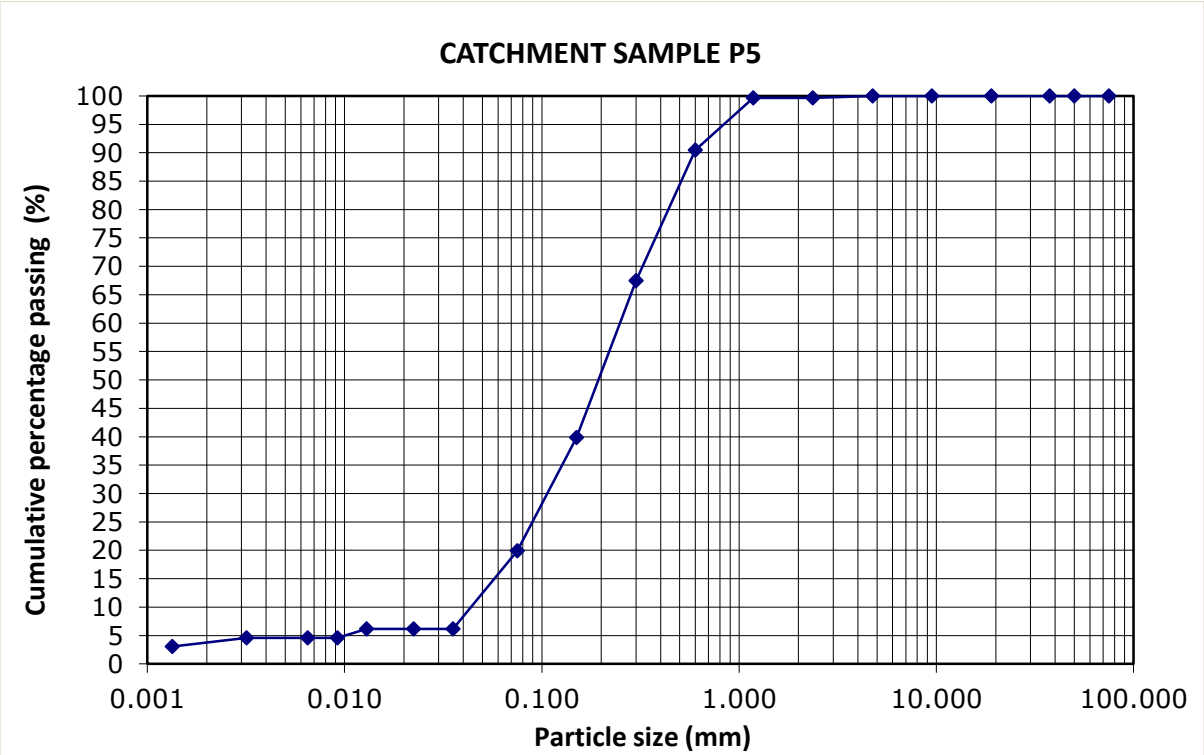

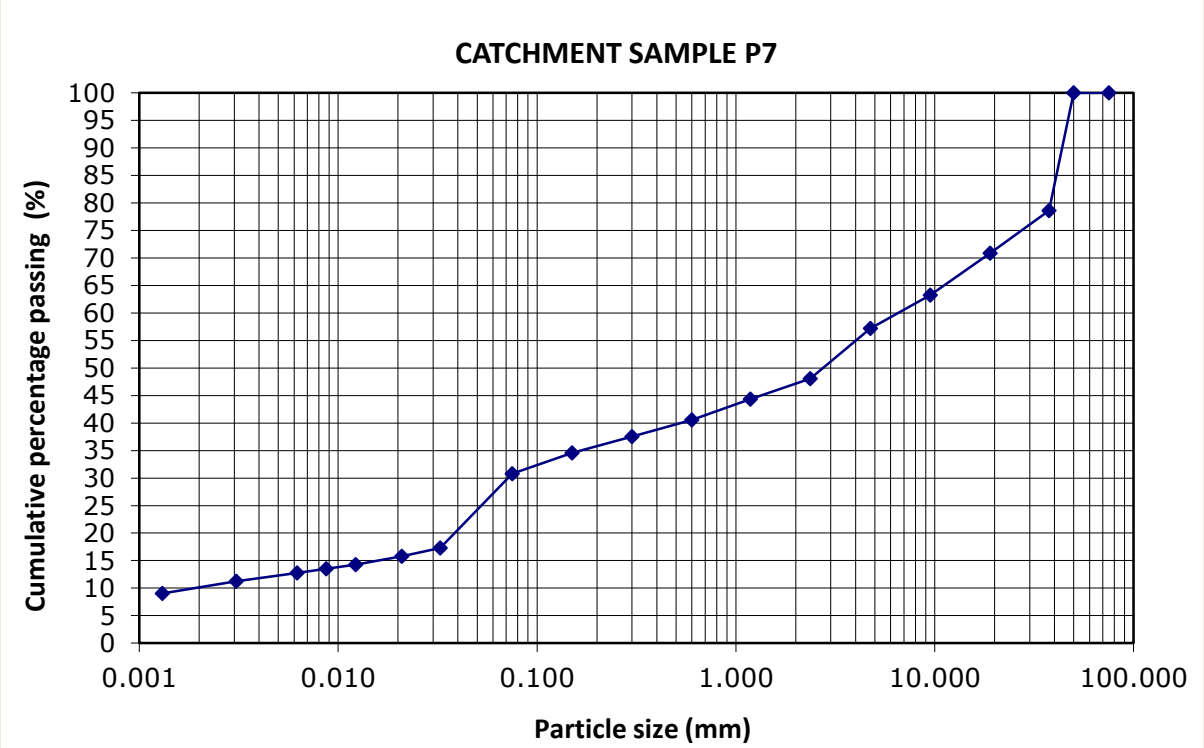

Appendix E: Observed daily flow against the simulated daily flow for 1980-2020

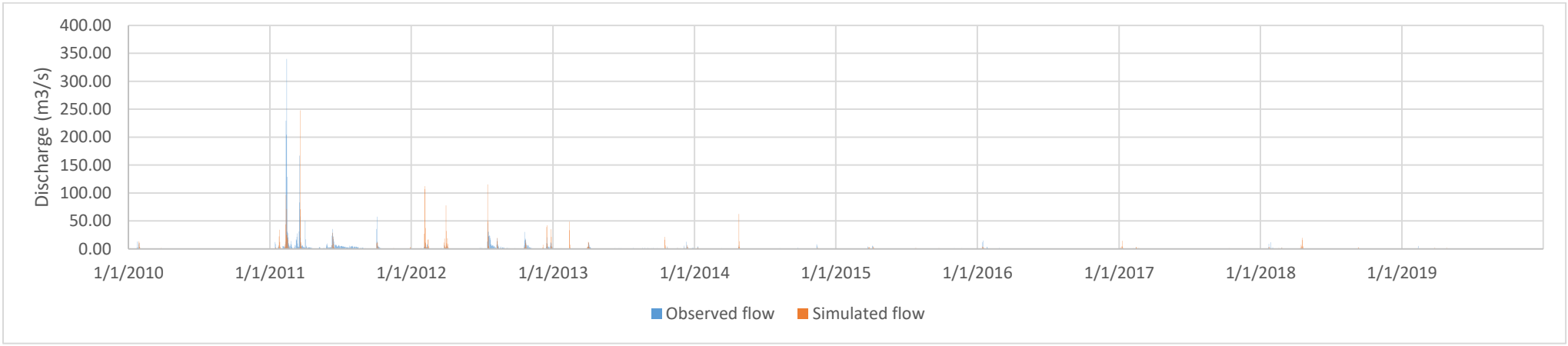

Figure E-1: Simulated daily flow against observed daily flow into the Nqweba Reservoir for the 2010-2020 period

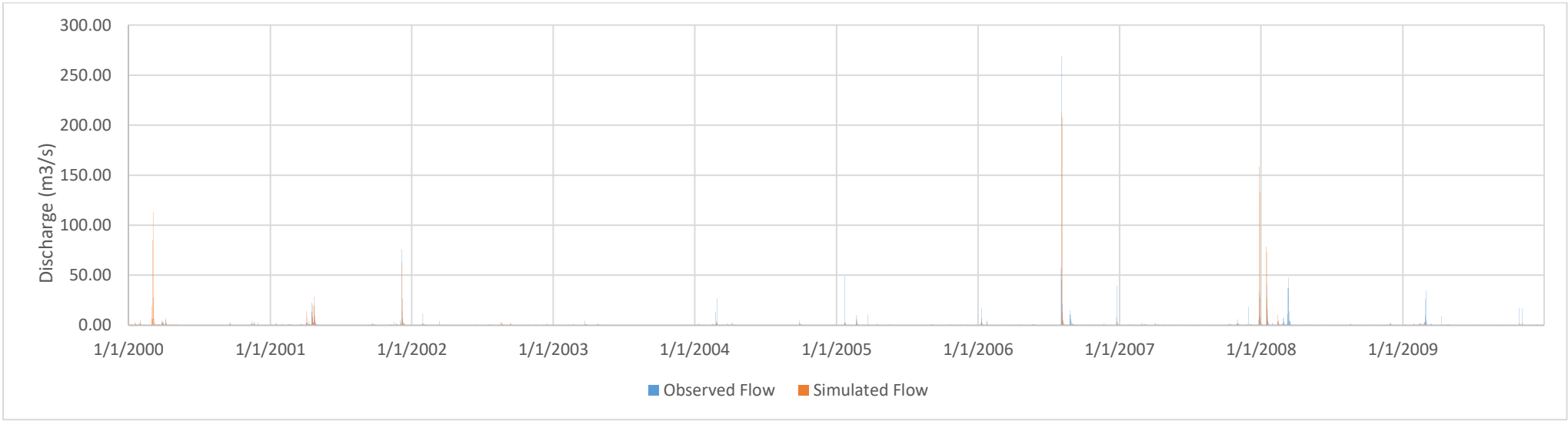

Figure E-2: Simulated daily flow against observed daily flow into the Nqweba Reservoir for the 2000-2010 period

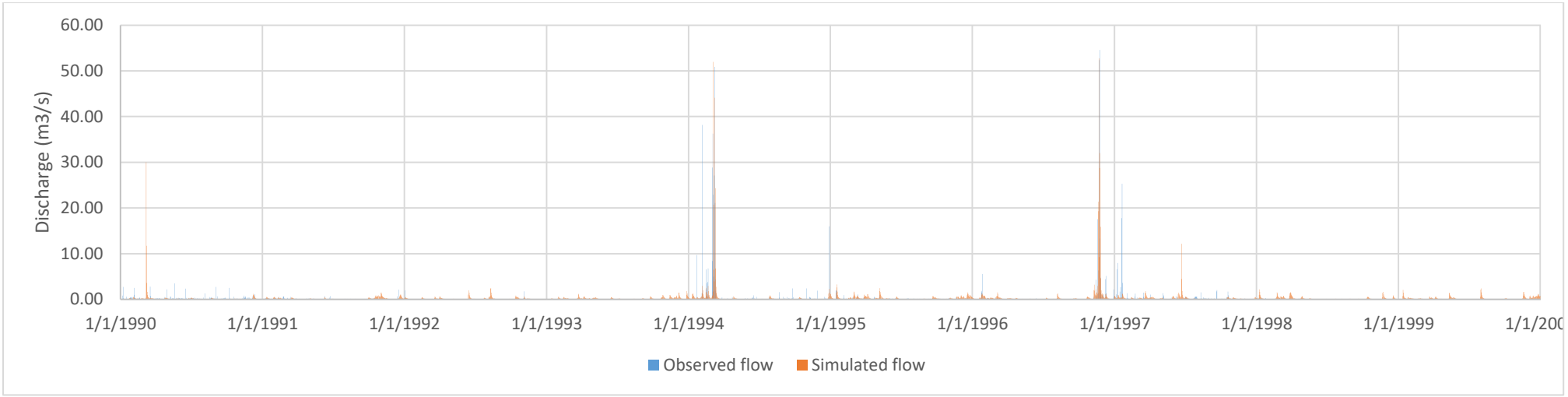

Figure E-3: Simulated daily flow against observed daily flow into the Nqweba Reservoir for the 1990-2000 period

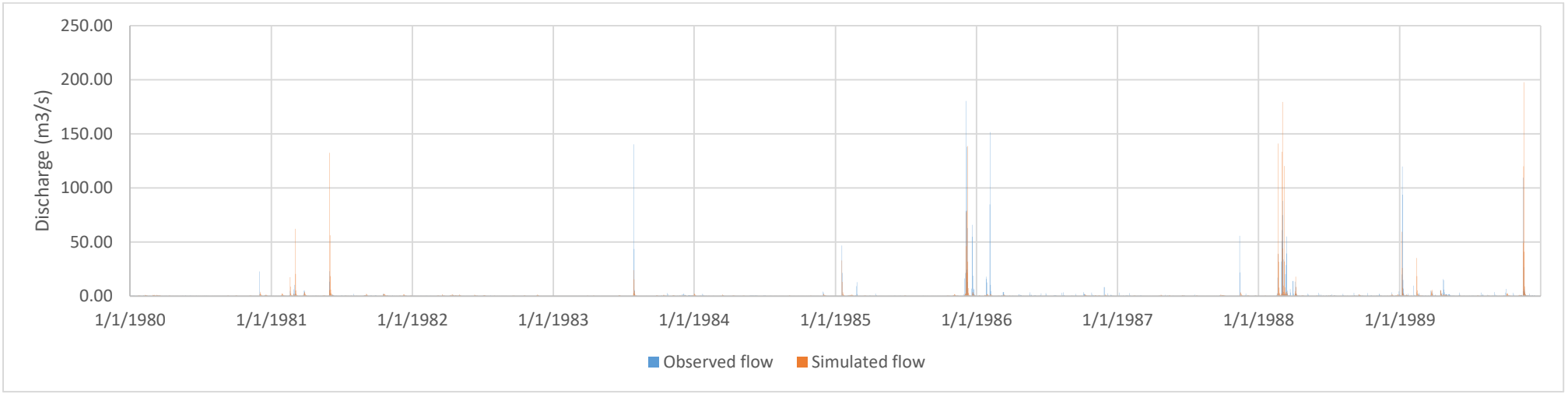

Figure E-4: Simulated daily flow against observed daily flow into the Nqweba Reservoir for the 1980-1990 period

Appendix F: Climate comparison between Graaff-Reinet and Somerset East

Graaff Reinet

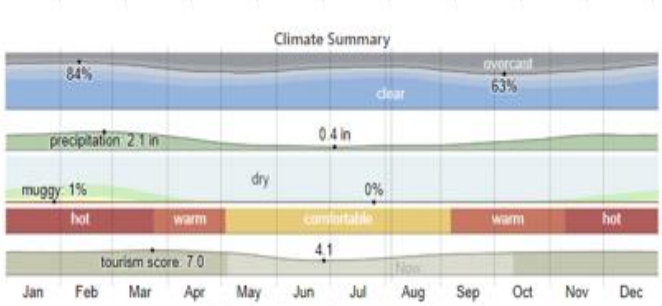

Click on each chart for more information.

Somerset East

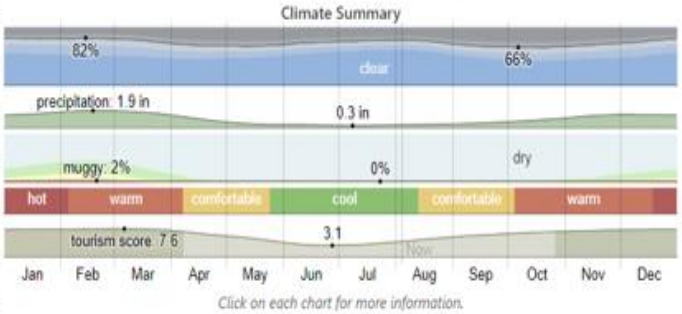

Click on each chart for more information.

Graaff-Reinet

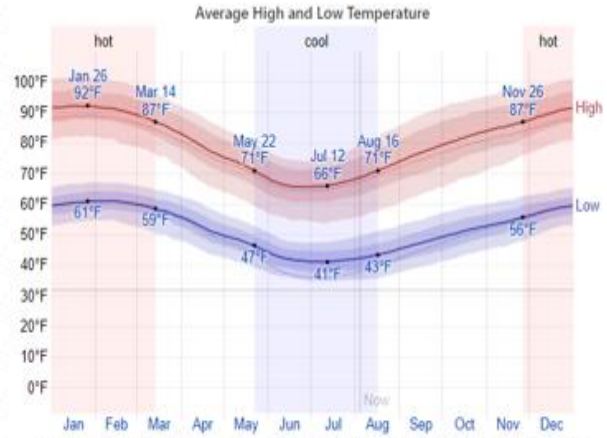

The daily average high (red line) and low (blue line) temperature, with 25th to 75th and 10th to 90th percentile bands. The thin dotted lines are the corresponding average perceived temperatures.

Somerset East

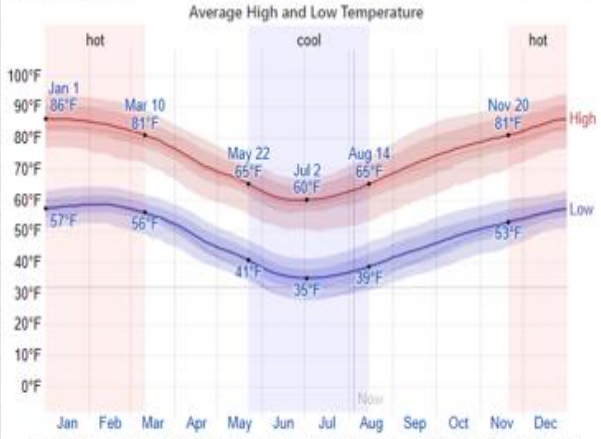

The daily average high (red line) and low (blue line) temperature, with 25th to 75th and 10th to 90th percentile bands. The thin dotted lines are the corresponding average perceived temperatures.

Graaff-Reinet

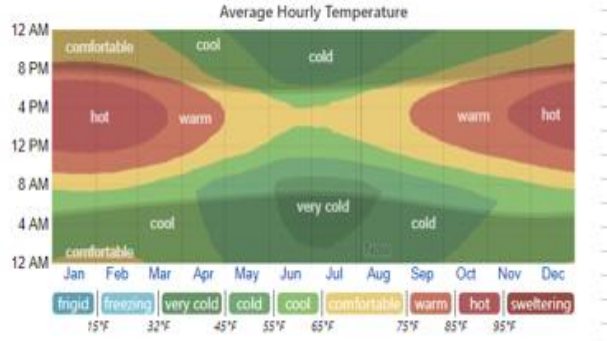

The average hourly temperature, color coded into bands. The shaded overlays indicate night and civil twilight.

Somerset East

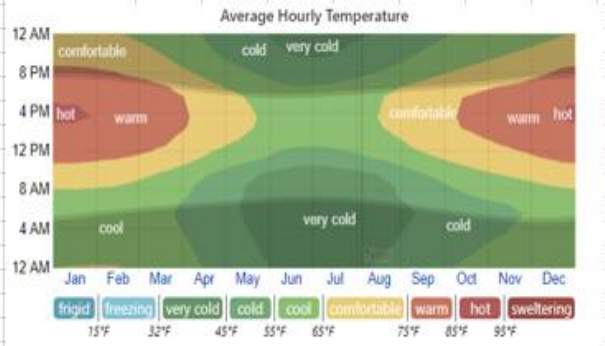

The average hourly temperature, color coded into bands. The shaded overlays indicate night and civil twilight.

Graaff-Reinet

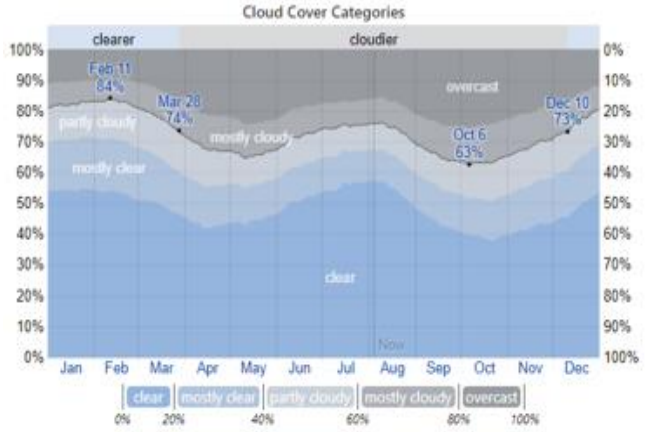

The percentage of time spent in each cloud cover band, categorized by the percentage of the sky covered by clouds.

Somerset East

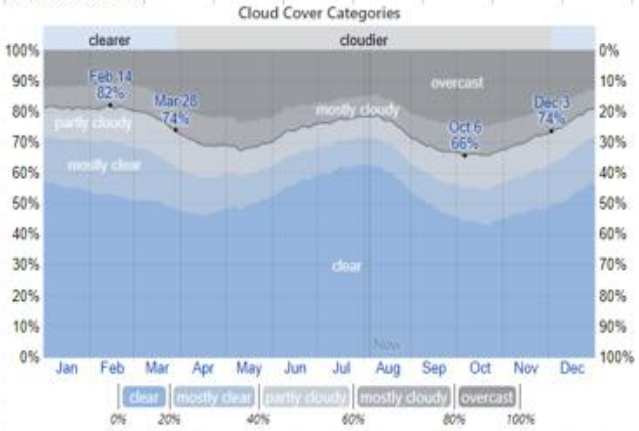

The percentage of time spent in each cloud cover band, categorized by the percentage of the sky covered by clouds.

Graaff-Reinet

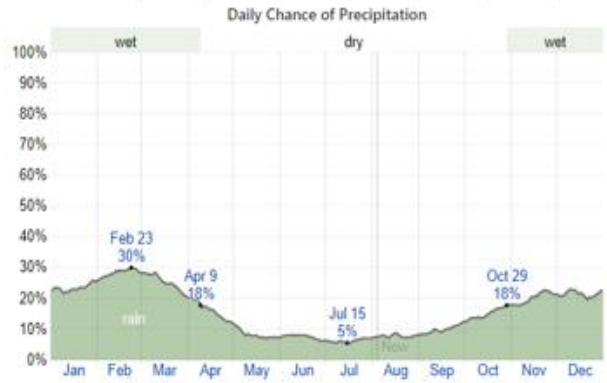

The percentage of days in which various types of precipitation are observed, excluding trace quantities: rain alone, snow alone, and mixed (both rain and snow fell in the same day).

Somerset East

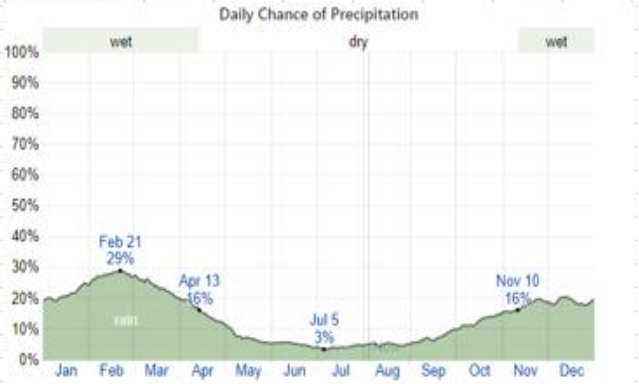

The percentage of days in which various types of precipitation are observed, excluding trace quantities: rain alone, snow alone, and mixed (both rain and snow fell in the same day).

Graaff-Reinet

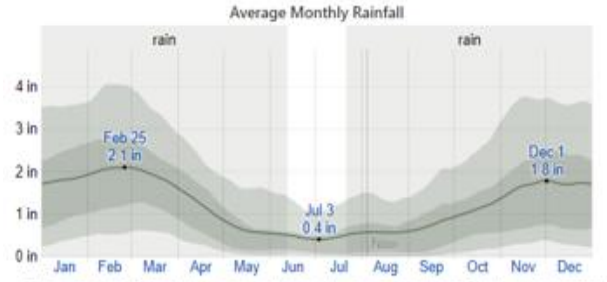

The average rainfall (solid line) accumulated over the course of a sliding 31-day period centered on the day in question, with 25th to 75th and 10th to 90th percentile bands. The thin dotted line is the corresponding average liquid-equivalent snowfall.

Somerset East

The average rainfall (solid line) accumulated over the course of a sliding 31-day period centered on the day in question, with 25th to 75th and 10th to 90th percentile bands. The thin dotted line is the corresponding average liquid-equivalent snowfall.

Appendix G: Determination of climate change evaporation signal for the first six months of 2030-2040 in relation to 2010-2020 (Using RCP 4.5 emission scenario)

Table G-1: Average monthly minimum temperatures (°C) projected by climate models for the first six months of 2010-2020 period and RCP 4.5

Date (YYYY-MM)	MIROC-ESM	CNRM-CM5	CanESM2	FGOALS-s2	BNU-ESM	MIROC 5	GFDL-ESM2G	MIROC-ESM-CHEM	GFDL-ESM2M	MRI-CGCM3	bcc-csm1-1
2010-01	14.43	14.54	14.35	14.43	14.02	12.95	12.74	15.56	12.93	13.69	14.56
2010-02	14.83	14.88	15.80	14.81	15.61	14.08	13.13	16.29	13.51	13.99	16.28
2010-03	14.71	14.89	15.11	14.28	15.35	13.14	12.24	14.6	12.72	13.46	15.02
2010-04	9.18	10.14	12.72	13.43	13.5	12.26	10.86	11.09	12.37	11.9	12.61
2010-05	6.57	7.00	8.44	8.19	7.98	8.41	7.03	6.54	8.34	8.57	8.61
2010-06	8.06	7.62	7.77	7.57	7.00	7.25	5.84	8.36	6.64	8.44	5.91

Table G-2: Average monthly minimum temperatures (°C) projected by climate models for the first six months of 2030-2040 period and RCP 4.5

Date (YYYY-MM)	MIROC-ESM	CNRM-CM5	CanESM2	FGOALS-s2	BNU-ESM	MIROC5	GFDL-ESM2G	MIROC-ESM-CHEM	GFDL-ESM2M	MRI-CGCM3	bcc-csm1-1
2030-01	15.54	12.81	14.73	15.12	14.95	13.66	13.20	15.69	13.34	12.87	14.92
2030-02	15.30	14.26	15.39	15.16	15.89	14.37	12.86	16.16	13.65	13.35	14.90
2030-03	13.60	13.64	14.62	15.4	14.77	12.67	12.49	15.44	12.97	12.18	14.54
2030-04	11.21	11.78	14.23	12.5	12.66	11.2	11.31	12.08	11.76	12.52	12.70
2030-05	8.74	8.52	8.81	10.6	9.60	8.03	7.46	9.76	8.73	9.33	10.74
2030-06	8.57	7.68	7.93	8.62	9.46	7.75	7.26	8.67	8.78	7.10	8.90

Table G-3: Average monthly maximum temperatures (°C) projected by climate models for the first six months of 2010-2020 period and RCP 4.5

Date (YYYY-MM)	MIROC-ESM	CNRM-CM5	CanESM2	FGOALS-s2	BNU-ESM	MIROC5	GFDL-ESM2G	MIROC-ESM-CHEM	GFDL-ESM2M	MRI-CGCM3	bcc-csm1-1
2010-01	30.14	28.03	29.12	28.76	28.12	27.35	26.69	30.18	27.45	29.37	28.69
2010-02	30.13	28.01	30.28	28.46	30.13	28.62	26.17	30.03	27.92	29.29	31.10
2010-03	29.89	28.88	29.67	26.67	29.89	26.68	24.52	29.06	26.20	27.35	29.39
2010-04	23.20	23.32	26.29	26.72	28.16	26.35	24.30	23.28	26.50	26.61	26.86
2010-05	19.52	20.00	23.04	22.78	21.57	22.25	20.02	19.37	23.07	21.56	20.53
2010-06	23.29	21.91	22.41	22.53	20.62	20.41	19.97	22.99	20.18	20.08	21.58

Table G-4: Average monthly maximum temperatures (°C) projected by climate models for the first six months of 2030-2040 period and RCP 4.5

Date (YYYY-MM)	MIROC-ESM	CNRM-CM5	CanESM2	FGOALS-s2	BNU-ESM	MIROC5	GFDL-ESM2G	MIROC-ESM-CHEM	GFDL-ESM2M	MRI-CGCM3	bcc-csm1-1
2030-01	29.55	25.76	28.89	30.62	30.23	27.7	27.74	29.96	27.61	26.87	28.65
2030-02	29.54	27.81	29.74	30.55	30.44	26.35	26.65	31.42	28.08	27.61	28.05
2030-03	27.12	26.03	28.53	29.96	28.87	26.37	25.29	28.13	26.85	25.12	28.83
2030-04	25.00	25.15	28.85	26.77	26.57	24.58	25.59	26.27	25.56	24.93	26.67
2030-05	22.25	21.46	22.94	24.44	22.12	20.13	21.81	23.16	22.08	23.15	24.31
2030-06	23.15	22.15	23.17	22.94	22.56	22.58	22.4	22.97	23.55	21.82	23.13

Table G-5: Calculated temperature component of Hargreaves Equation for projected temperature for first six months of 2010-2020 period and RCP 4.5

Date (YYYY-MM)	MIROC-ESM	CNRM-CM5	CanESM2	FGOALS-s2	BNU-ESM	MIROC 5	GFDL-ESM2G	MIROC-ESM-CHEM	GFDL-ESM2M	MRI-CGCM3	bcc-csm1-1
2010-01	88.33	78.18	83.53	81.75	79.12	76.46	73.63	87.45	76.93	85.25	81.29
2010-02	87.93	77.71	87.67	79.93	87.15	81.41	70.96	85.85	78.64	84.65	91.20
2010-03	86.88	81.86	85.43	72.07	86.25	73.26	64.41	83.01	71.45	76.05	84.17
2010-04	60.62	60.74	71.85	73.18	79.75	72.46	64.45	60.00	73.06	73.85	74.50
2010-05	46.94	48.67	60.14	59.15	54.47	57.03	48.75	46.40	60.28	54.30	50.30
2010-06	61.17	55.81	57.74	58.21	50.97	50.17	48.51	59.96	49.34	48.65	54.41

Table G-6: Calculated temperature component of Hargreaves Equation for projected temperature for the first six months of 2030-2040 period and RCP 4.5

Date (YYYY-MM)	MIROC-ESM	CNRM-CM5	CanESM2	FGOALS-s2	BNU-ESM	MIROC5	GFDL-ESM2G	MIROC-ESM-CHEM	GFDL-ESM2M	MRI-CGCM3	bcc-csm1-1
2030-01	84.39	69.40	82.07	90.04	88.30	77.49	78.05	86.22	77.35	74.35	80.72
2030-02	84.60	77.43	85.48	89.66	88.36	70.47	73.36	92.93	79.26	77.34	77.87
2030-03	74.86	69.82	80.47	86.54	81.93	72.25	67.58	77.60	74.18	67.09	81.97
2030-04	67.23	67.52	82.36	74.17	73.16	65.44	69.72	72.23	69.32	65.96	73.58
2030-05	56.95	53.92	59.67	65.18	56.12	48.98	55.44	60.25	56.29	60.37	64.56
2030-06	60.56	56.74	60.70	59.71	57.95	58.40	57.70	59.82	62.12	55.48	60.41

Table G-7: Climate change evaporation signals for the first six months of 2030-2040 period in relation to the 2010-2020 period and RCP 4.5

Date (YYYY-MM)	MIROC-ESM	CNRM-CM5	CanESM 2	FGOALS-s2	BNU-ESM	MIROC5	GFDL-ESM2G	MIROC-ESM-CHEM	GFDL-ESM2M	MRI-CGCM3	bcc-csm1-1	ENSEMBLE MEAN
2030-01	0.96	0.89	0.98	1.10	1.12	1.01	1.06	0.99	1.01	0.87	0.99	1.00
2030-02	0.96	1.00	0.97	1.12	1.01	0.87	1.03	1.08	1.01	0.91	0.85	0.98
2030-03	0.86	0.85	0.94	1.20	0.95	0.99	1.05	0.93	1.04	0.88	0.97	0.97
2030-04	1.11	1.11	1.15	1.01	0.92	0.90	1.08	1.20	0.95	0.89	0.99	1.03
2030-05	1.21	1.11	0.99	1.10	1.03	0.86	1.14	1.30	0.93	1.11	1.28	1.10
2030-06	0.99	1.02	1.05	1.03	1.14	1.16	1.19	1.00	1.26	1.14	1.11	1.10

Appendix H: Climate change rainfall and evaporation signals for all climate models and RCP 4.5 and RCP 8.5 emission scenarios

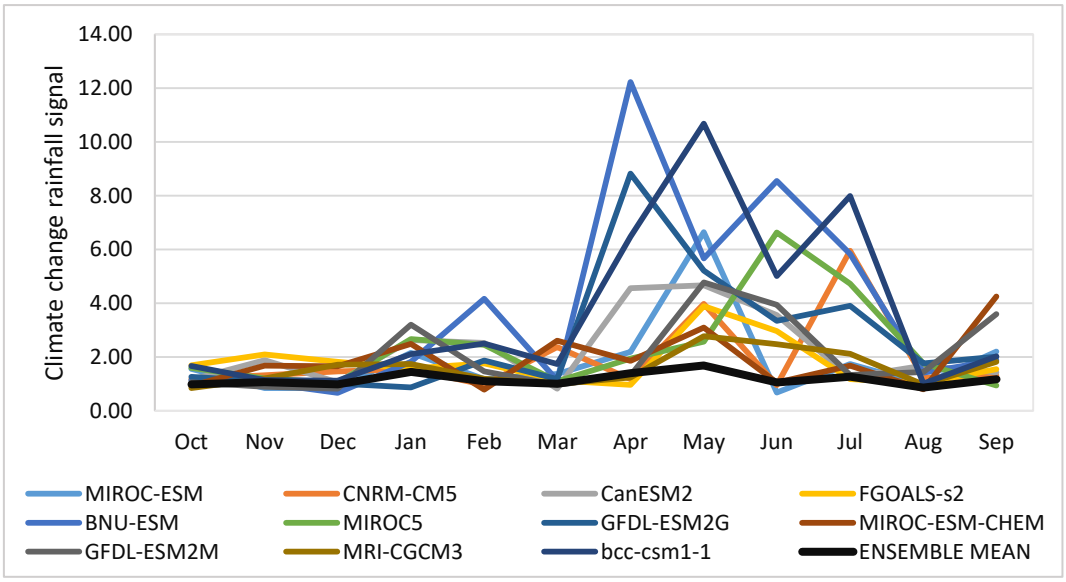

Figure H-1: Average monthly climate change rainfall signals predicted by climate models for 2030-2040 in relation to 2010-2020 (RCP 8.5)

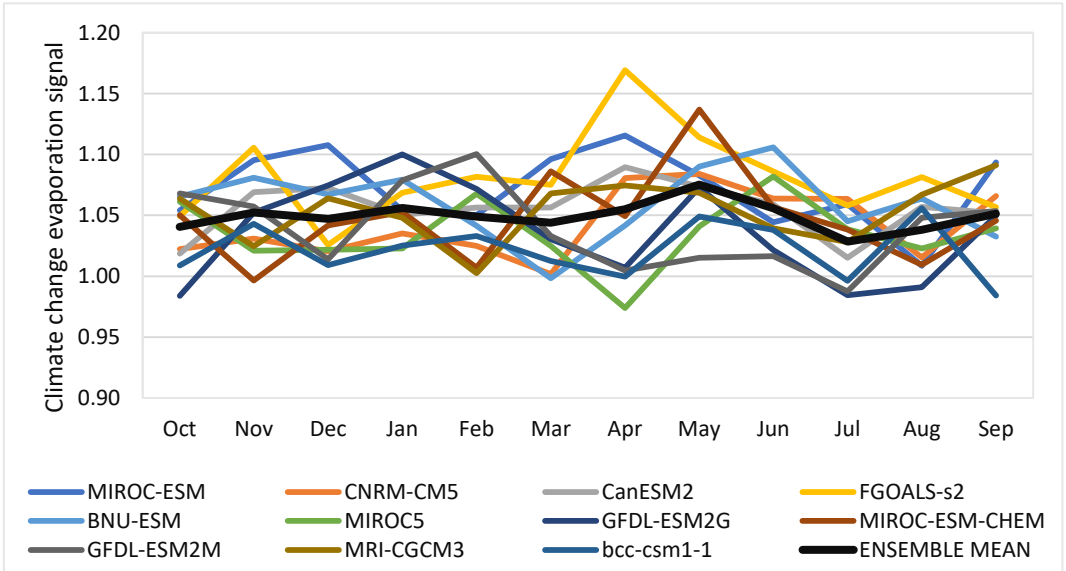

Figure H-2: Average monthly climate change evaporation signals predicted by climate models for 2030-2040 in relation to 2010-2020 (RCP 8.5)

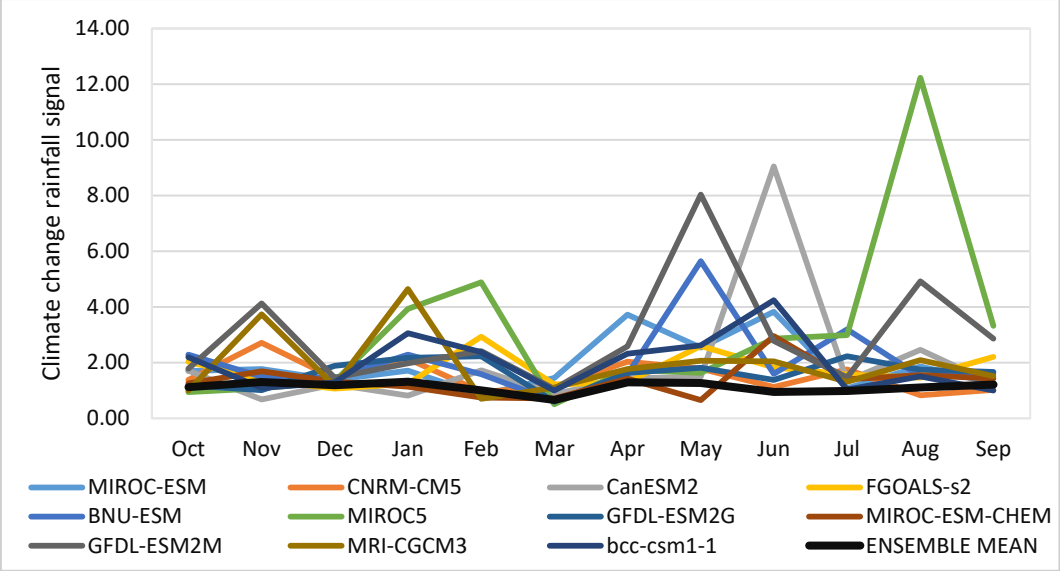

Figure H-3: Average monthly climate change rainfall signals predicted by climate models for 2050-2060 in relation to 2010-2020 (RCP 4.5)

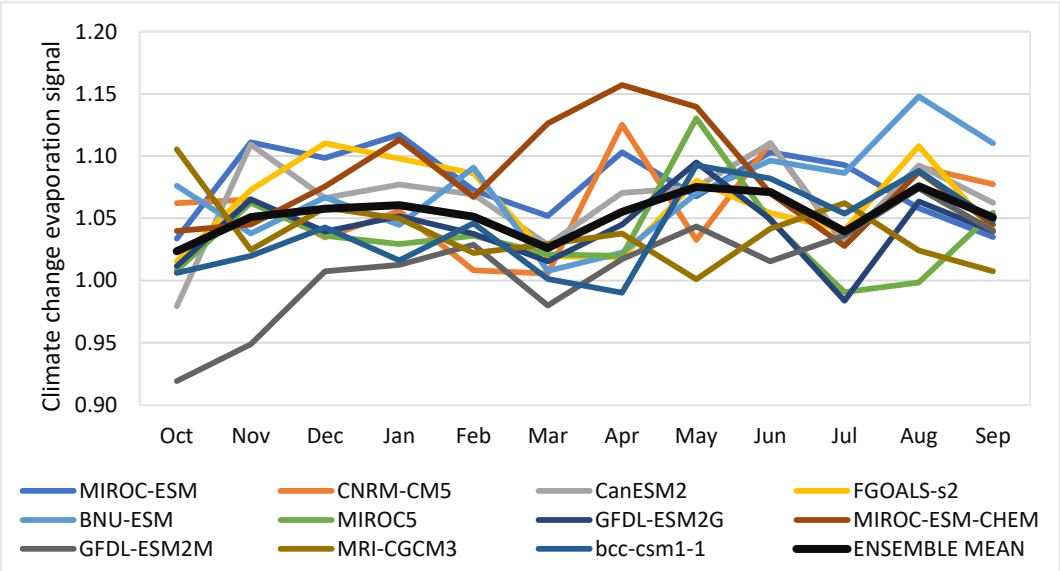

Figure H-4: Average monthly climate change evaporation signals predicted by climate models for 2050-2060 in relation to 2010-2020 (RCP 4.5)

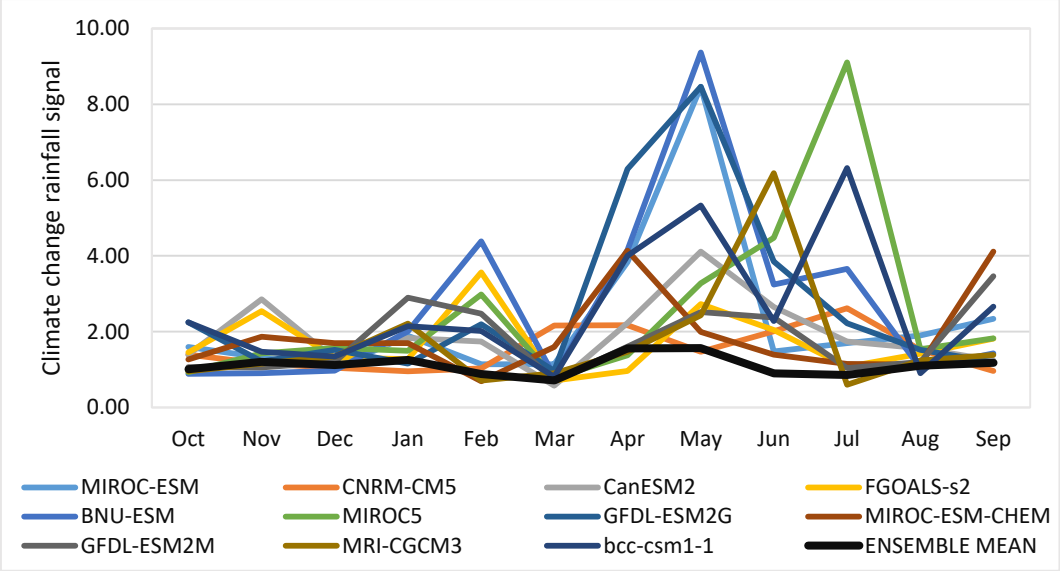

Figure H-5: Average monthly climate change rainfall signals predicted by climate models for 2050-2060 in relation to 2010-2020 (RCP 8.5)

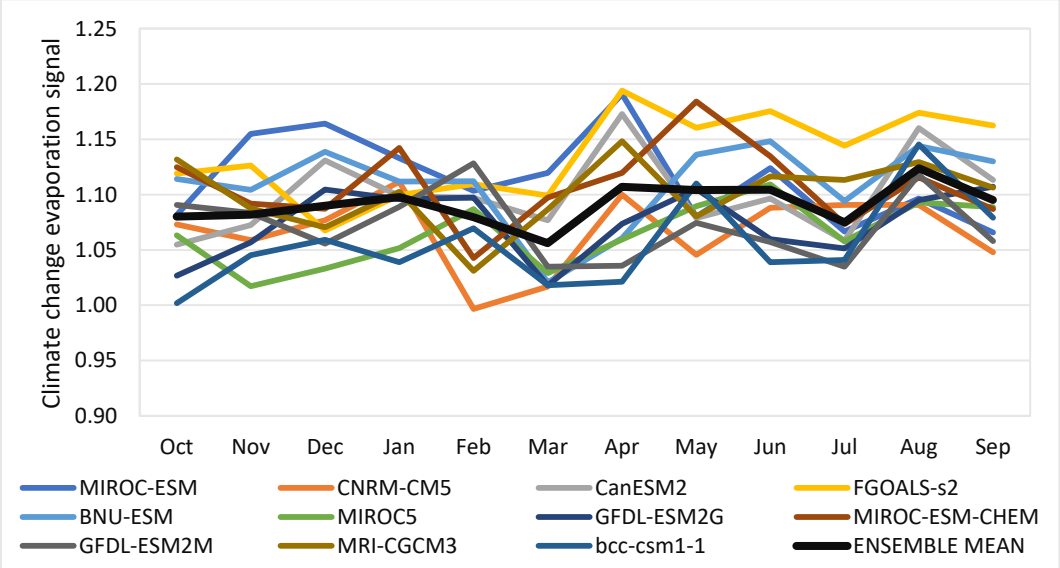

Figure H-6: Average monthly climate change evaporation signals predicted by climate models for 2050-2060 in relation to 2010-2020 (RCP 8.5)

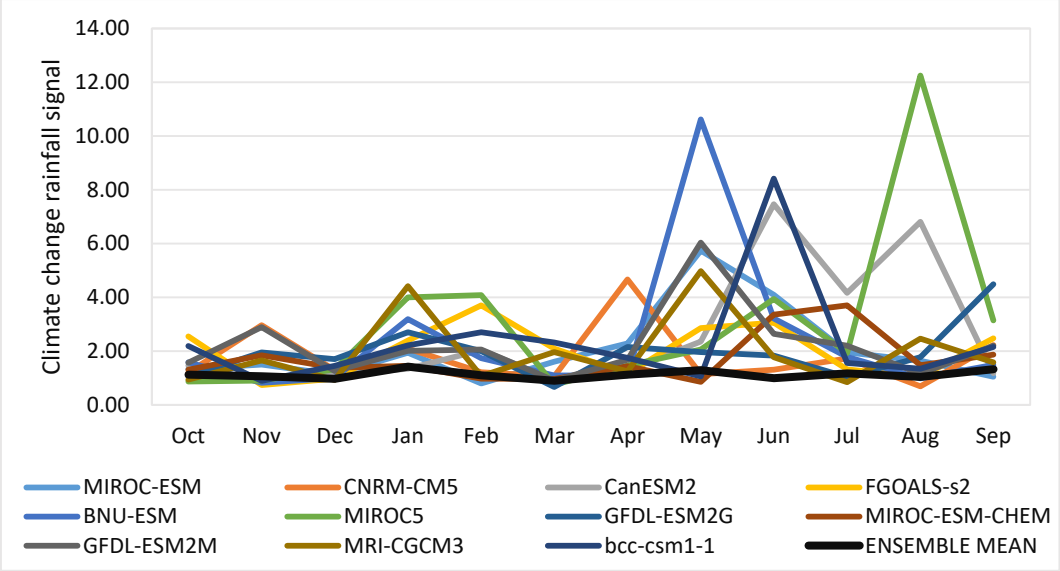

Figure H-7: Average monthly climate change rainfall signals predicted by climate models for 2070-2080 in relation to 2010-2020 (RCP 4.5)

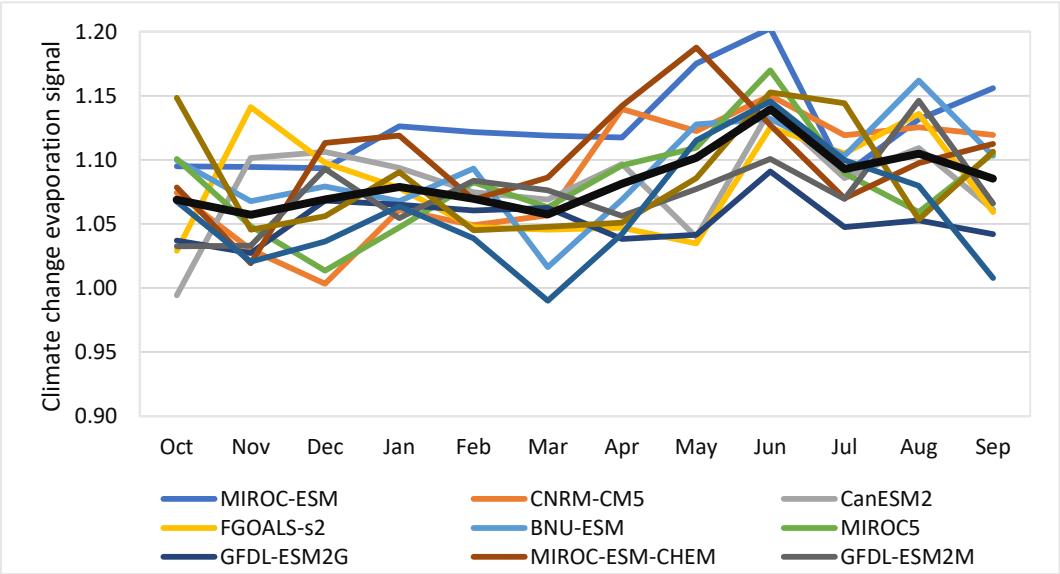

Figure H-8: Average monthly climate change evaporation signals predicted by climate models for 2070-2080 in relation to 2010-2020 (RCP 4.5)

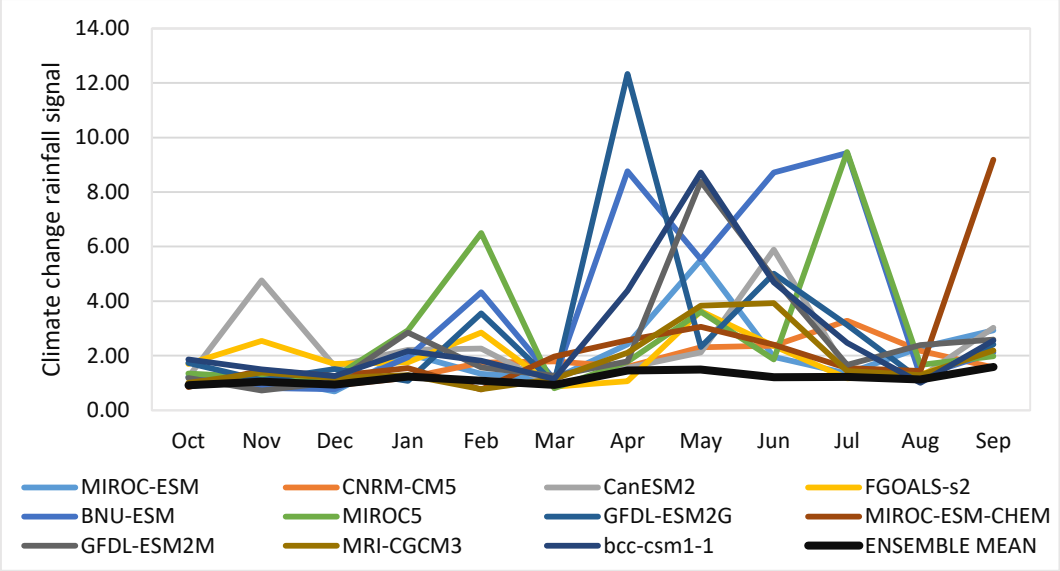

Figure H-9: Average monthly climate change rainfall signals predicted by climate models for 2070-2080 in relation to 2010-2020 (RCP 8.5)

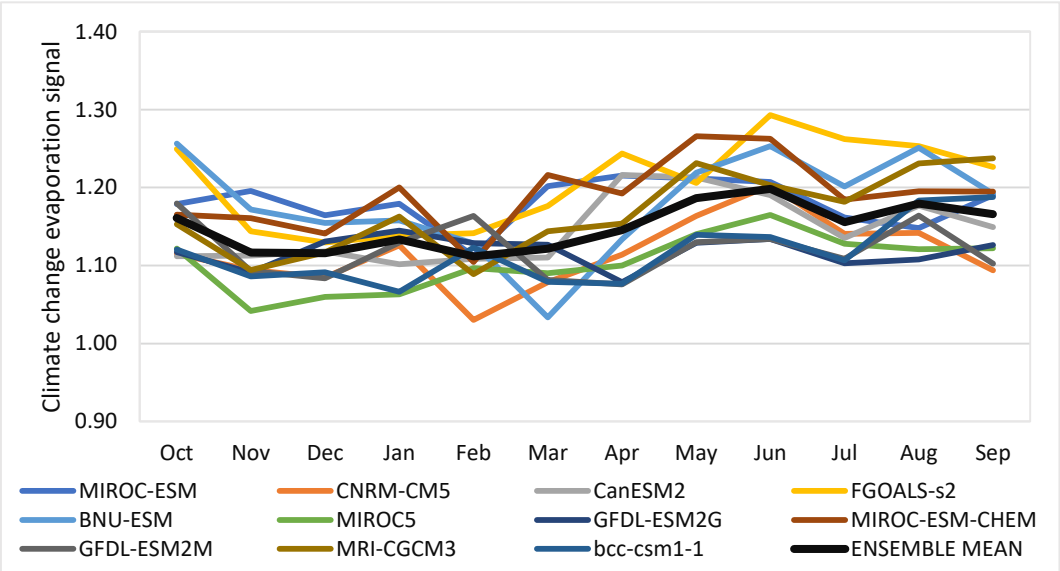

Figure H-10: Average monthly climate change evaporation signals predicted by climate models for 2070-2080 in relation to 2010-2020 (RCP 8.5)

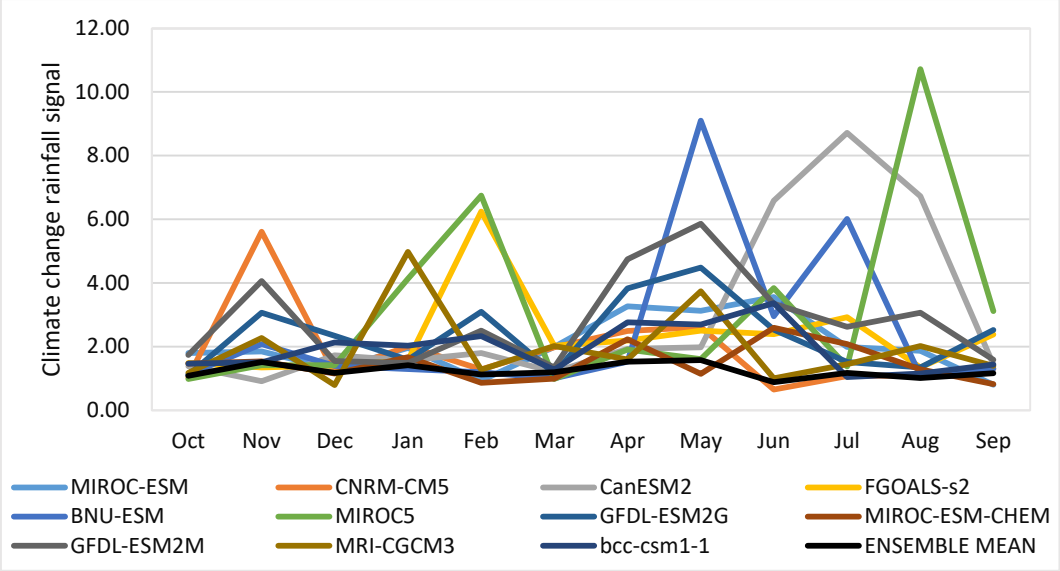

Figure H-11: Average monthly climate change rainfall signals predicted by climate models for 2090-2100 in relation to 2010-2020 (RCP 4.5)

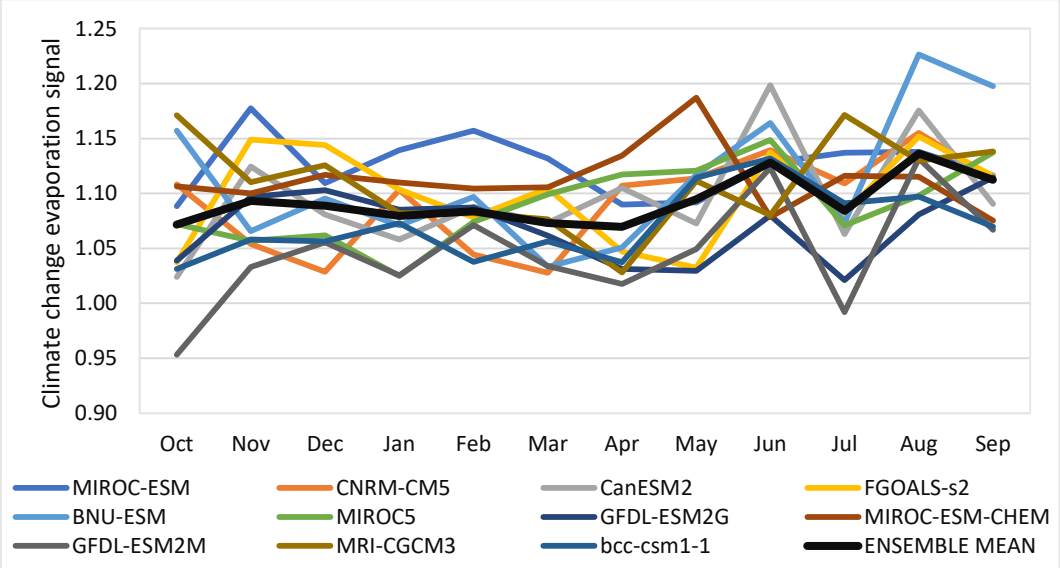

Figure H-12: Average monthly climate change evaporation signals predicted by climate models for 2090-2100 in relation to 2010-2020 (RCP 4.5)

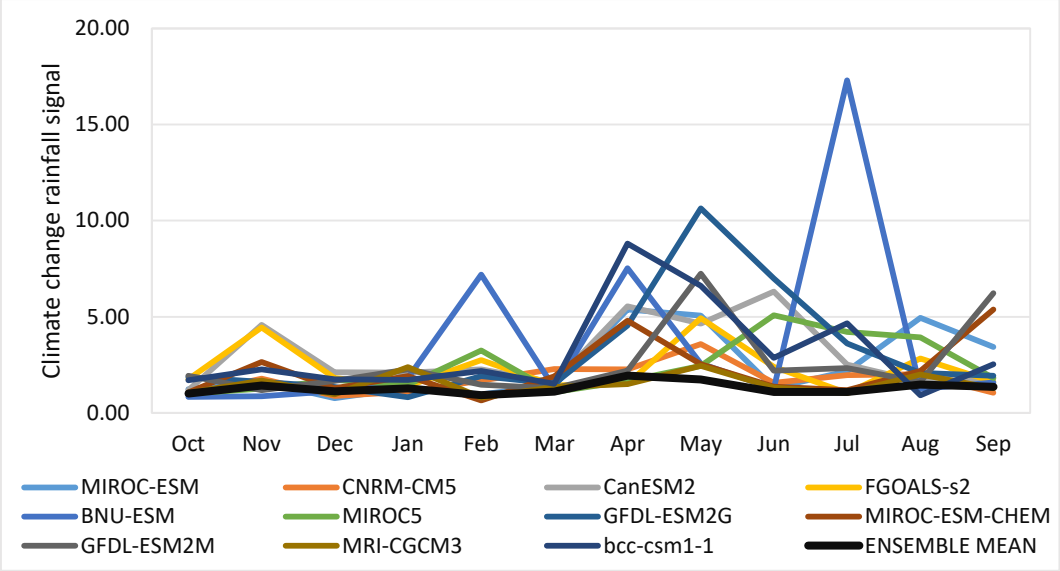

Figure H-13: Average monthly climate change rainfall signals predicted by climate models for 2090-2100 in relation to 2010-2020 (RCP 8.5)

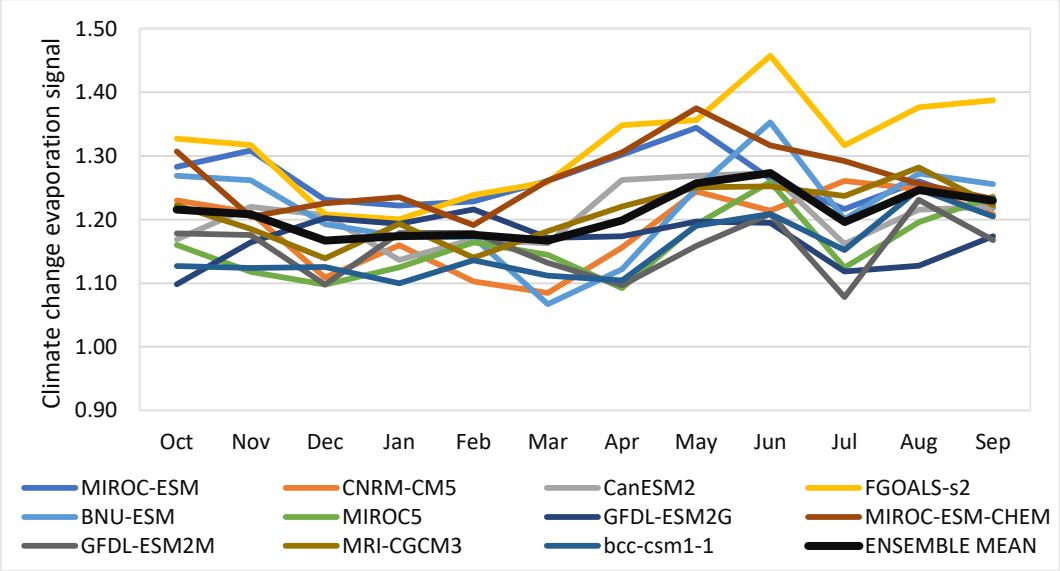

Figure H-14: Average monthly climate change evaporation signals predicted by climate models for 2090-2100 in relation to 2010-2020 (RCP 8.5)

Appendix I: Impact of climate change on yearly water flow using constant vegetation and RCP 4.5 and RCP 8.5

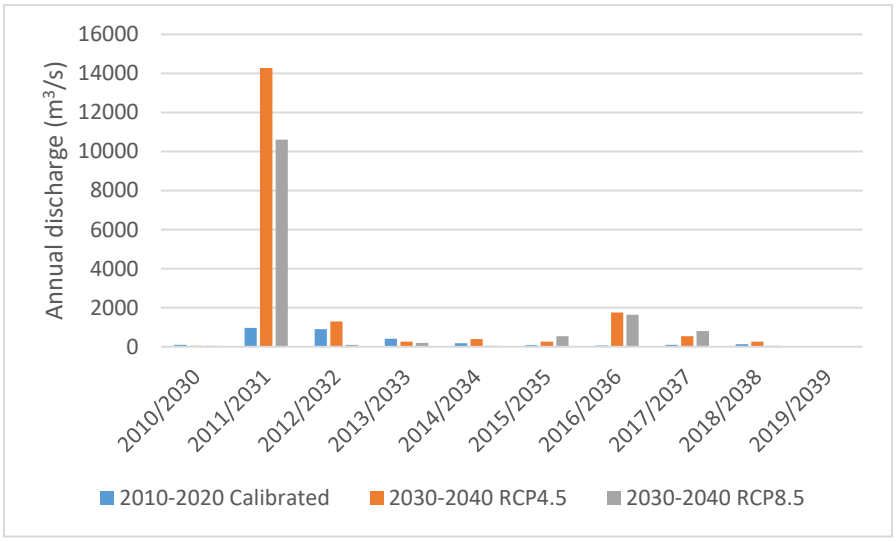

Figure I-1: Calibrated yearly flow (2010-2020) against the simulated flow (2030-2040)

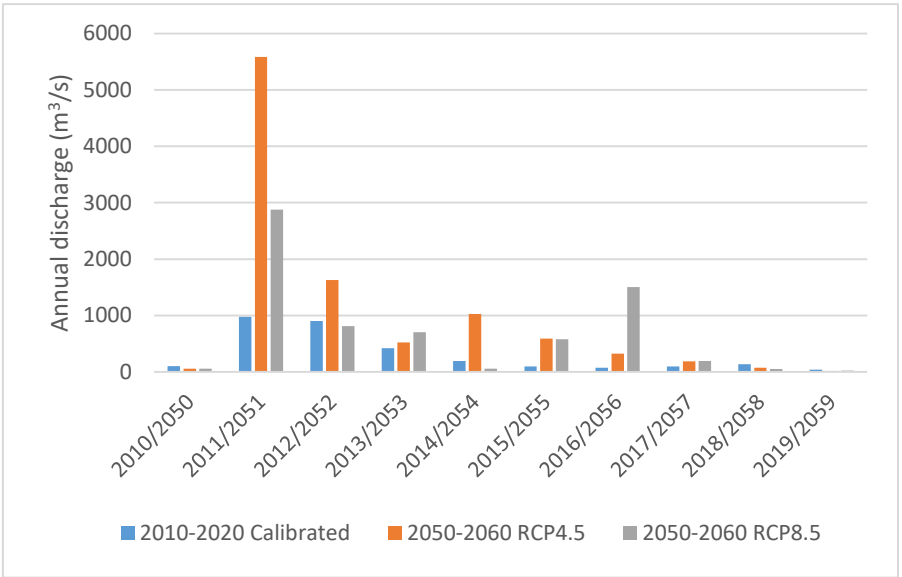

Figure I-2: Calibrated yearly flow (2010-2020) against the simulated flow (2050-2060)

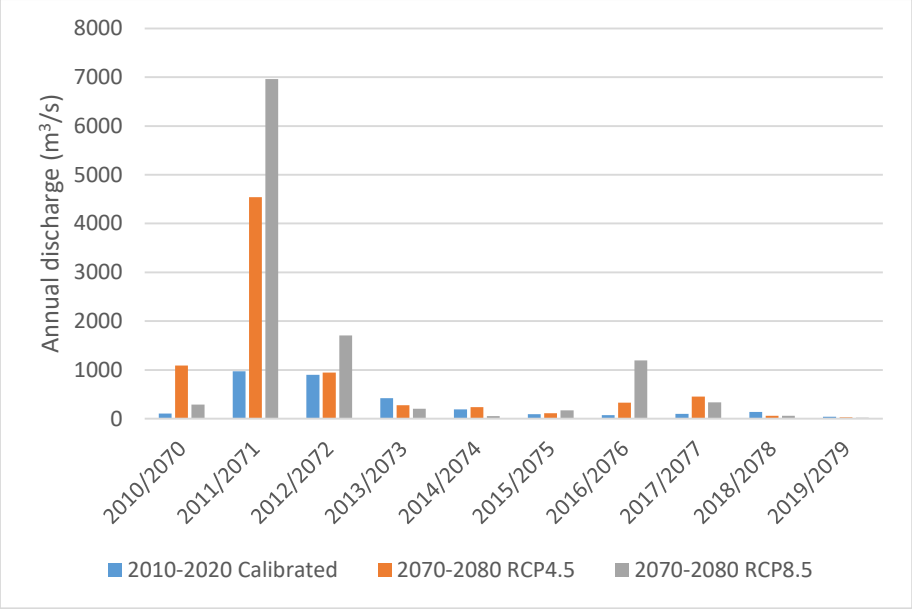

Figure I-3: Calibrated yearly flow (2010-2020) against the simulated flow (2070-2080)

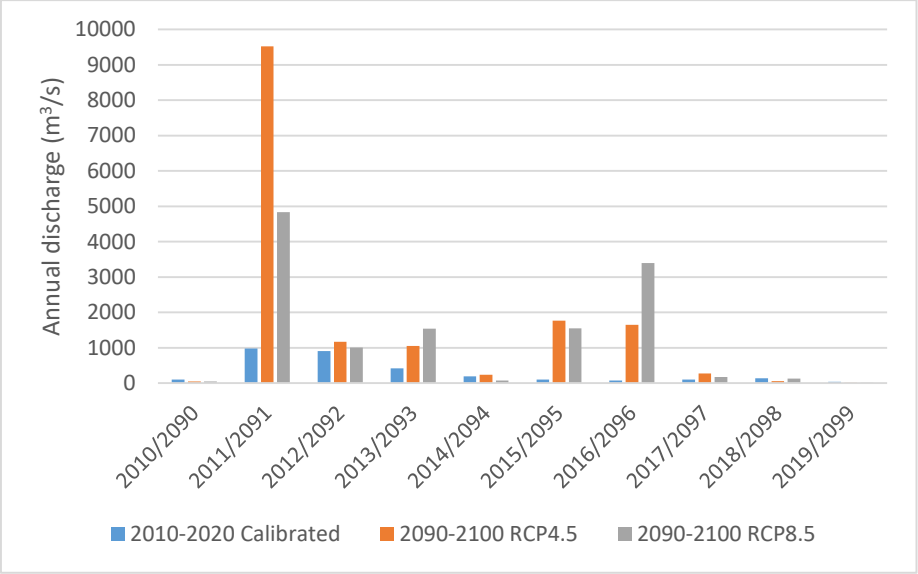

Figure I-4: Calibrated yearly flow (2010-2020) against the simulated flow (2090-2100)